Small field dosimetry

Experimental methods and Monte Carlo simulation in small field radiation therapy dosimetry

Gavin Cranmer-Sargison

Submitted in accordance with the requirements for the degree of
Doctor of Philosophy

The University of Leeds

Leeds Institute of Genetics, Health and Therapeutics,

School of Medicine

April, 2014

The candidate confirms that the work submitted is his/her own, except where work which has formed part of jointly-authored publications has been included. The contribution of the candidate and the other authors to this work has been explicitly indicated below. The candidate confirms that appropriate credit has been given within the thesis where reference has been made to the work of others. The following jointly-authored publications are based on the work of Chapters 2, 3, 4, 5 and 6 respectively.

[1] Cranmer-Sargison G., Weston S., Sidhu N. P. and Thwaites D. I. (2011). Experimental small field 6 MV output ratio analysis for various diode detector and accelerator combinations. *Radiother. Oncol.* 100, 429-35.

[2] Cranmer-Sargison G., Weston S., Evans J. A., Sidhu N. P. and Thwaites D. I. (2011) Implementing a newly proposed Monte Carlo based small field dosimetry formalism for a comprehensive set of diode detectors. *Med. Phys*. 38, 6592-602.

[3] Cranmer-Sargison G., Weston S., Evans J. A., Sidhu N. P. and Thwaites D. I. (2012) Monte Carlo modelling of diode detectors for small field MV photon dosimetry: detector model simplification and the sensitivity of correction factors to source parameterization. *Phys. Med. Biol.* 57, 5141-53

[4] Cranmer-Sargison G., Liu P.Z.Y., Weston S., Suchowerska N., and Thwaites D. I. (2013). Small field dosimetric characterization of a new 160-leaf MLC. *Phys. Med. Biol.* 58, 7343-54

[5] Cranmer-Sargison G., Charles P. H., Trapp J. V., and Thwaites D. I. (2013). A methodological approach to reporting corrected small field relative outputs. *Radiother. Oncol.* 109(3), 350-355

In all cases the work originated from intellectual property generated by the candidate and the majority of measurements were performed by the candidate. All data was analyzed and the articles were written by the candidate as primary author. Under the supervision of the candidate the authors P.Z.Y. Liu and N. Suchowerska assisted in the measurements and analysis of the data presented in Chapter 5. Under the supervision of the candidate the authors P.H. Charles and J.V. Trapp performed some of the measurements presented in Chapter 6. The authors S. Weston, J.A. Evans, N.P. Sidhu, and D.I. Thwaites were all on the candidate's supervisory committee, as such, their input was that of a normal student-supervisor relationship.

Invited speaker presentations

Recent developments in small field dosimetry

AMPICON 2013: 34th Annual Conference of Association of Medical Physicists of India, Kolkata, India

November 13 - 15, 2013

Diode Detectors - uses, common problems and correction factors

Monte Carlo Simulations - uses, common problems and correction factors

ACPSEM Summer School 2012: Stereotactic radiation therapy focusing on small photon field dosimetry

Brisbane, Australia

Nov. 30 - Dec. 2, 2012

Small field dosimetry with diodes: Monte Carlo modelling and measurement

Institute of Medical Physics Seminar Series

School of Physics, University of Sydney

November 29, 2012

Conference abstracts

Reporting corrected small field relative outputs: a methodological approach

G. Cranmer-Sargison, P.H. Charles, J.V. Trapp and D.I. Thwaites

20th International Conference on Medical Physics and Biomedical Engineering (ICMP)

Sept. 19 - 23, 2013

A methodological approach to reporting corrected small field relative outputs

G. Cranmer-Sargison, P.H. Charles, J.V. Trapp and D.I. Thwaites

ESTRO 32, Geneva, Switzerland

April 19 - 23, 2013

Monte Carlo modelling for small field 6 MV diode dosimetry

G. Cranmer-Sargison, S. Weston, N. and D.I. Thwaites

EPSM 2012, Gold Coast, Australia

December 2 - 6, 2012

Small field dosimetric characterization of a new 160-leaf MLC

G. Cranmer-Sargison, P.Z.Y. Liu, S. Weston, N. Suchowerska and D.I. Thwaites

EPSM 2012, Gold Coast, Australia

December 2 - 6, 2012

Diode detector modelling for small fields and correction factor sensitivity to source parameterization

G. Cranmer-Sargison, S. Weston, N.P. Sidhu and D.I. Thwaites

ESTRO 31, Barcelona, Spain

May 9 - 13, 2012

Diode detector modelling for Monte Carlo small field MV photon dosimetry[1]

G. Cranmer-Sargison, S. Weston, N.P. Sidhu and D.I. Thwaites

European Medical Physics and Engineering Conference 2011, Dublin, IRL

September 1 - 3, 2011

Characterizing small field MV photon output factors using various diode detectors and accelerator combinations

G. Cranmer-Sargison, S. Weston, N.P. Sidhu and D.I. Thwaites

European Medical Physics and Engineering Conference 2011, Dublin, IRL

September 1 - 3, 2011

Diode detector modelling for Monte Carlo based small field dosimetry

G. Cranmer-Sargison, S. Weston, N.P. Sidhu and D.I. Thwaites

The International Workshop on Recent Advances in Monte Carlo Techniques for Radiation Therapy

Montreal, Quebec

June 8 - 10, 2011

Application of a recently proposed Monte Carlo based small field dosimetry formalism for a comprehensive set of diode detectors

G. Cranmer-Sargison, S. Weston, N.P. Sidhu and D.I. Thwaites

11th Biennial ESTRO Meeting, London, UK

May 8 - 12, 2011

---

[1] Awarded Best Proffered Paper: Modelling and Simulation in Medicine Session organised by the Institute of Physics (IOP) Medical Physics and Computational Physics Groups.

Experimental small field output factor analysis for various diode detector and accelerator combinations

G. Cranmer-Sargison, S. Weston, N.P. Sidhu and D.I. Thwaites

11th Biennial ESTRO Meeting, London, UK

May 8 - 12, 2011

Acknowledgements

I want to start by thanking my wife Tammy for her unconditional support and encouragement. I share the joy of completion with her and my children Cathrine, Grace and Evan - knowing this would not have been possible if not for their love. I would like to express my deepest appreciation to my supervisors David Thwaites and Steve Weston. Not only did they provide me their scientific expertise but also offered me their friendship. I would like to thank Tony Evans, Narinder Sidhu and Chris Newcomb for their support of the spit-site program. Finally, a heartfelt thank-you to my examiners Andy Beavis and Steven Sourbron for a wonderful afternoon spent together.

Abstract

The goal of the thesis was to investigate, and better define, what the requirements are for accurate small field relative dosimetry. Diode detector selection and experimental techniques were evaluated. EGSnrc Monte Carlo simulations were used to predict diode detector dosimetric parameters and assist in interpreting measured data. An emerging scintillator based detector technology was also tested and methods developed to standardize the reporting of small field dosimetric data. Using careful experimental methods the relative output uncertainty for the smallest square field size of side 0.5 cm was reduced to better than ±1.00% for all detector types. Monte Carlo simulation data revealed that for the same small field size the relative output measured using unshielded and shielded diodes will be 5% and 10% greater than the actual relative output in water. Further simulation work showed that simplified diode detector models are valid for use in small field dosimetry simulations. The diode detector over-response was also shown to be insensitive to variations in the electron energy and spot size incident on the Bremsstrahlung target. Experimental methods were refined to include the definition of an effective field size, which was shown to remove much of the ambiguity in reporting small field relative output data across a population of linear accelerators. Each of the for mentioned areas of investigation have been shown to be requirements for accurate small field relative.

Table of Contents

List of Tables

List of Figures

List of Abbreviations

AAPM	American Association of Physicists in Medicine
CoP	Code of practice
CV	Coefficient of Variation
EFD	Unshielded diode detector Manufactured by Scanditronix/IBA
f_{clin}	Clinical field size of interest
f_{msr}	Machine-specific reference field
FWHM	Full width half maximum of a distribution
Gy	Gray
GFM	Generalized field model
IMRT	Intensity modulated radiation therapy
$k_{Q_{clin},Q_{msr}}^{f_{clin},f_{msr}}$	Detector specific small field replacement correction factor
Linac	Medical linear accelerator
MC	Monte Carlo
MLC	Multi-leaf collimator
MU	Monitor unit
OF	Output factor
$OR_{det}^{f_{clin}}$	Detector specific output ratio for f_{clin}

$OR_{det_{MC}}^{f_{clin}}$	Monte Carlo calculated $OR_{det}^{f_{clin}}$
PFD	Shielded diode detector Manufactured by Scanditronix/IBA
SBRT	Stereotactic body radiation therapy
S_{cp}	Total scatter factor
SFD	Stereotactic field diode Manufactured by Scanditronix/IBA
SRS	Stereotactic radiosurgery
SSD	Source to surface distance
T60008	Shielded diode detector Manufactured by PTW-Freiburg, Germany
T60012	Unshielded diode detector Manufactured by PTW-Freiburg, Germany
T60016	Shielded diode detector Manufactured by PTW-Freiburg
T60017	Unshielded diode detector Manufactured by PTW-Freiburg
VRT	Variance reduction technique

Chapter 1
Introduction

1.1 General dosimetry considerations

Radiation oncology is a highly developed form of cancer treatment that utilizes high-energy radiation to kill cancer cells by damaging their DNA. Damage occurs to normal cells as well as cancer cells and therefore each treatment must be carefully planned to minimize side effects. External beam radiation therapy treatment techniques generally utilize high energy X-rays produced by a medical linear accelerator (linac) [60]. The treatment objective is to deliver a therapeutic level of radiation to a tumour site while minimizing radiation to the surrounding normal tissues. As Beyzadeoglu *et al* [11] emphasize, accuracy and precision in physical measurements and measuring techniques, combined with clarity in quantities and units, help to increase radiotherapy efficacy.

Radiation is measured and prescribed in terms of absorbed dose (D), often just termed dose, which is defined as the total energy imparted by ionizing radiation to matter per unit mass. More rigorously, dose is defined as the energy imparted (dE) by ionizing radiation to matter at a point in a volume element of mass (dm), such that,

$$D = \frac{dE}{dm}. \qquad (1.1)$$

The convention, under the International System of Units (SI) [54,55], is to report dose using the unit Gray, where $Gy = J \cdot kg^{-1}$. Although the definition of dose is simple no assumptions should be made regarding the simplicity of the actual experimental process of measuring dose or the clinical dosimetry associated with radiation therapy.

1.1.1 Absorbed dose to water for high energy photon beams

Absorbed dose to water is clearly the main quantity of interest in radiation therapy. As such, the International Measurement System (IMS) for radiation metrology [54] provides a framework for the traceability of user reference instruments. The traceability is achieved through calibration of radiation instruments back to a primary standard. Primary standards are provided through Primary Dosimetry Standards Laboratories (PSDLs) at some national and international levels. Although each PSDL may use a different method for the determination of absolute dose to water for a ^{60}Co beam, each PSDL value has been shown to be well within 1.0% - relative to that determined by the Bureau International des Poids et Mesures (BIMP) [54].

The standard clinical practice for determining the absorbed dose to water is to follow a code of practice (CoP). Two such CoPs are the American Association of Physicists in Medicine (AAPM) Task Group Report 51 (TG-

51) [2] and the International Atomic Energy Agency (IAEA) Technical Report Series No. 398 [54]. Common to both CoPs is the use of ionization chambers calibrated in terms of absorbed dose to water. For high energy photon dosimetry the practice is to have a calibration factor that is directly traceable to an absorbed dose to water national standard determined at a PSDL.

Following the TRS-398 formalism the absorbed dose to water (D_w) at the point of measurement can be calculated for a beam of quality *Q* as follows,

$$D_{w,Q} = M_Q \cdot N_{D,w,Q_0} \cdot k_{Q,Q_0} , \qquad (1.2)$$

where M_Q is the fully corrected electrometer reading in coulombs, N_{D,w,Q_0} is the ionization chamber absorbed dose to water calibration factor in the reference beam quality Q_0 and k_{Q,Q_0} is a beam quality correction factor which accounts for the change in chamber response between the reference beam quality and the actual user beam quality Q.

The beam quality correction factor is defined as the ratio of the calibration factors, at beam qualities Q and Q_0 such that,

$$k_{Q,Q_0} = \frac{N_{D,w,Q}}{N_{D,w,Q_0}} = \frac{D_{w,Q}/M_Q}{D_{w,Q_0}/M_{Q_0}} . \quad (1.3)$$

Following a CoP to establish the absorbed dose to water at a point is generally referred to as reference dosimetry. The dose associated with all other beam configurations can then be reported as relative values with respect to the reference conditions. One example would be reporting the relative point dose as a function of change in field size. These relative values are commonly reported as “field factors” [58], “output factors” [90] or “total scatter factors” [59] and are typically determined experimentally using ionization chamber measurements normalized back to the chamber reading under reference conditions. Look-up tables for various symmetric and asymmetric field sizes can then be generated and used, for example, in the commissioning of commercial treatment planning systems.

In recent years radiation therapy techniques have evolved to include the delivery of small field sizes traditionally considered unique to stereotactic radiosurgery (SRS). Linear accelerator based stereotactic body radiation therapy (SBRT) and advanced intensity modulated radiation therapy (IMRT) techniques, such as volumetric modulated arc therapy (VMAT), have been made possible through the improved mechanical accuracy as well as increased stability and dosimetric control of the linac [5]. As with many technological advancements, the delivery methods used in radiation therapy have evolved at a rate that has outpaced the standardization in measuring and reporting relative dose for small field sizes. In short, the required link

between relative and reference dosimetry, which should be based on well established CoPs, has not yet been fully developed for small fields.

1.1.2 A proposed small field dosimetry formalism

Alfonso *et al* [1] has, under the mandate of an international working group, presented a new formalism for reference dosimetry of small and non-standard fields. The authors extend clinical reference dosimetry based on absorbed dose to water to include small static fields. A number of new definitions were used in the proposed formalism and are as follows:

f_{ref} is the conventional reference field in dosimetry CoPs at which the calibration coefficient of an ionization chamber in terms of absorbed dose to water has been provided by a standards laboratory.

f_{msr} is the machine-specific reference field, for static modalities or treatment machines that cannot establish the conventional reference field.

f_{clin} is the clinical radiation field at which the absorbed dose to water needs to be determined.

The absorbed dose to water for the machine-specific reference field is related to the conventional CoP reference field as follows,

$$D_{w,Q_{msr}}^{f_{msr}} = M_{Q_{msr}}^{f_{msr}} \cdot N_{D,w,Q_0} \cdot k_{Q,Q_0} \cdot k_{Q_{msr},Q}^{f_{msr},f_{ref}} \quad . \tag{1.4}$$

$k_{Q_{msr},Q}^{f_{msr},f_{ref}}$ accounts for the difference in ionization chamber response in the fields f_{ref} and f_{msr} and is defined as follows,

$$k_{Q_{msr},Q}^{f_{msr},f_{ref}} = \frac{D_{w,Q_{msr}}^{f_{msr}} \Big/ M_{Q_{msr}}^{f_{msr}}}{D_{w,Q}^{f_{ref}} \Big/ M_{Q}^{f_{ref}}} \quad . \tag{1.5}$$

Although defining $k_{Q_{msr},Q}^{f_{msr},f_{ref}}$ is rigorous, and represents a natural extension from the established CoPs, it is not unreasonable to assume that for most linear accelerator based systems the change in beam quality between the conventional reference field and a well chosen machine-specific reference field will be small and therefore $k_{Q_{msr},Q}^{f_{msr},f_{ref}}$ will typically be set to unity.

The relative dose for f_{clin}, with respect to f_{msr}, is defined as follows,

$$D_{w,Q_{clin}}^{f_{clin}} = D_{w,Q_{msr}}^{f_{msr}} \cdot \Omega_{Q_{clin},Q_{msr}}^{f_{clin},f_{msr}} \quad , \tag{1.6}$$

where $\Omega_{Q_{clin},Q_{msr}}^{f_{clin},f_{msr}}$ is defined as a field factor that converts the absorbed dose to water from the machine-specific reference field to that of the clinical field size of interest. $\Omega_{Q_{clin},Q_{msr}}^{f_{clin},f_{msr}}$ is by definition a ratio of absorbed doses to water

and can loosely be thought of as being equivalent to the traditional definition of an output factor. However, for small and non-standard field sizes one cannot assume that the ratio of detector readings will be equivalent to the ratio of absorbed doses to water and therefore, unlike traditional output factors used for standard field sizes, a correction factor must be applied to the measurement ratio. As such,

$$\Omega_{Q_{clin},Q_{msr}}^{f_{clin},f_{msr}} = \frac{M_{Q_{clin}}^{f_{clin}}}{M_{Q_{msr}}^{f_{msr}}} \cdot k_{Q_{clin},Q_{msr}}^{f_{clin},f_{msr}}, \qquad (1.7)$$

where $k_{Q_{clin},Q_{msr}}^{f_{clin},f_{msr}}$ corrects for the ratio of detector readings not being equivalent to the point dose ratio in water. However, as Alfonso *et al* note, if $k_{Q_{clin},Q_{msr}}^{f_{clin},f_{msr}}$ can be shown to be close to unity for a given detector then the ratio of readings will be sufficient in reporting the associated field factor. The authors continue and clearly state that $k_{Q_{clin},Q_{msr}}^{f_{clin},f_{msr}}$ needs to be taken into account for any detector not satisfying this condition. Using equations [1.6] and [1.7] the correction factor can be written as follows,

$$k_{Q_{clin},Q_{msr}}^{f_{clin},f_{msr}} = \frac{D_{w,Q_{clin}}^{f_{clin}} \Big/ M_{Q_{clin}}^{f_{clin}}}{D_{w,Q_{msr}}^{f_{msr}} \Big/ M_{Q_{msr}}^{f_{msr}}}. \qquad (1.8)$$

1.2 Small field dosimetry

The application of field size specific output factors is fundamental to clinical radiation therapy dosimetry. For field sizes ≥ 4.0 cm x 4.0 cm [58,59,90], determining output factors experimentally can be considered standard practice. However, as Das *et al* [33] note, experimental small field dosimetry can be challenging given the lack of lateral charged particle equilibrium, spectral changes as a function of field size, detector choice and subsequent perturbations of the charged particle fluence. Aspradakis *et al* [5] summarize the implications of these challenges and note that most of the dosimetric tools routinely used in the clinic are inappropriate for small fields and that almost every aspect associated with radiation therapy dosimetry must be scrutinized for its appropriateness for use with small fields.

1.2.1 Detector selection

Traditional Farmer type ionization chambers are not suitable dosimeters for small fields as the active volume is often wider than the field itself - which results in extreme beam perturbations and unavoidable problems with volume averaging. To address this limitation many vendors have made small volume thimble ionization chambers and solid-state diode detectors commercially available. However, as Laud *et al* [71] notes, one can expect an underestimation in measured relative output from ionization chambers and an overestimation from silicon diode detectors.

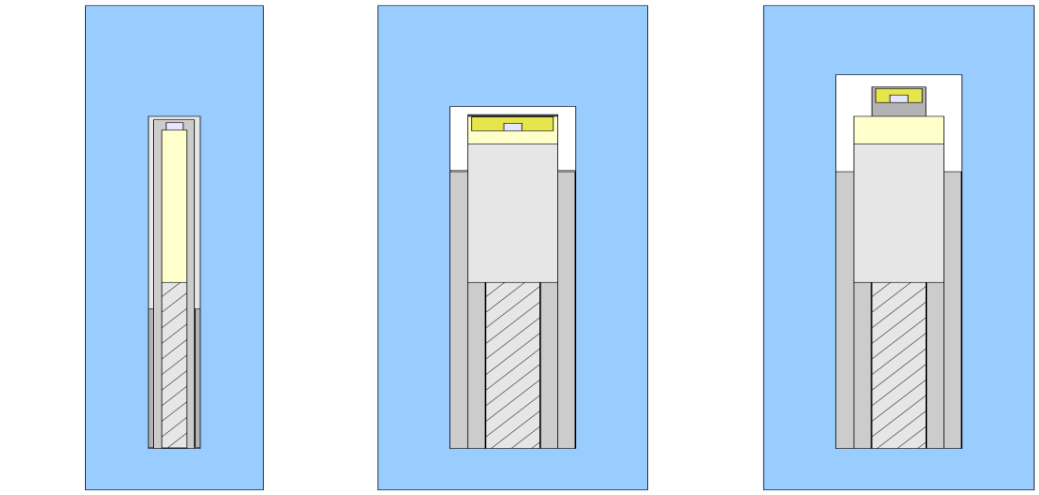

(A) (B) (C)

Figure 1.1 Schematic diagrams showing the detector geometries of the (A) stereotactic field diode (SFD) from IBA/Scanditronix and the (B) T60017 unshielded diode and (C) T60016 shielded diode from PTW. The SFD and PTW chips are surrounded by ABS plastic (grey) and epoxy (yellow) respectively. The T60017 filter plate is shown as thick line above the epoxy layer and below the water-equivalent RW3 cap (white). The diagonal-striped grey represents the coaxial cable with the darker outermost grey cylinder representing the stainless steel stem.

Clearly there is no ideal commercial detector for small field dosimetry, yet detector choice can be made following two general rules: (i) the detector has a small active volume and (ii) the detector is constructed with the least amount of beam perturbing materials. For field sizes ≤ 1.0 cm x 1.0 cm commercial diode detectors, with an active area ≤ 1.0 mm^2, appear to be a reasonable choice. These detectors suffer less volume averaging than ion chambers and other diodes with larger active areas - notably the electron

field diode (EFD) and photon field diode (PFD), which McKerracher and Thwaites [82] quote as under-responding by 6.2% for a 0.5 cm stereotactic collimator.

1.2.2 Experimental considerations

The significant influence experimental set-up has on small field relative output measurements cannot be overlooked. Apart from the work of Sauer and Wilbert [97], McKerracher and Thwaites [81,82,83] and Li *et al* [73], most other experimental data presented in the literature lack clear uncertainty analysis. This is unfortunate as measurements should only be presented and interpreted within the context of experimental uncertainties. Sauer and Wilbert do just that for field sizes of 0.4 cm x 0.4 cm and 0.8 cm x 0.8 cm by reporting the standard deviation on SFD and PFD measured output factors at ±0.03 and ±0.01 per $cGy \cdot MU^{-1}$ respectively. McKerracher and Thwaites use the coefficient of variation (CV) to access the precision associated with experimental small field head scatter factor (S_c) measurements (CV between 0.1 and 0.3). The authors comment on real differences in values measured using multiple diode detector and mini-phantom combinations (CV greater than 1.0).

Li *et al* develop an evaluation of output uncertainties associated with position and volume averaging encountered when using a pinpoint chamber (PTW N31006) and an SFD. For a field size of 0.5 cm x 0.5 cm the output uncertainty that results from positional errors was shown to be the same for

each detector at less than ±1.0%, with the output uncertainty due to volume averaging quoted at approximately ±0.5% for the SFD. The authors note that the position effect is most important, and that reducing the positional uncertainty reduces the volume averaging effect, which in turn reduces the total uncertainty.

At the time the thesis was started the preceding summary represented the current “state-of-affairs” regarding experimental small field dosimetry. It was clear that a CoP type approach to measurement methodology had not yet been fully explored, nor had the expression of experimental uncertainties been systematically included in a CoP approach to small field dosimetry. In addition, the Alfonso *et al* paper had only recently been published so no work had been done regarding the experimental requirements for implementing the proposed small field dosimetry formalism.

1.3 Monte Carlo methods

1.3.1 General considerations

At the root of the Monte Carlo method is a simple computational structure whereby a process, for example the mean free path of a photon within a given volume, is computed as an average value taken over many individual particle histories [3,32]. For N histories of an independent event (x_i) the mean (μ) and variance (σ^2) of a simulation are calculated as follows,

$$\mu = \frac{1}{N}\sum_{i=1}^{N} x_i \tag{1.9}$$

and

$$\sigma^2 = \frac{1}{N-1}\sum_{i=1}^{N} \left(x_i - \mu\right)^2, \tag{1.10}$$

with the statistical uncertainty on the mean calculated such that,

$$\delta = \frac{\sigma}{\sqrt{N}}\,. \tag{1.11}$$

From Equation (1.11) one can see that the accuracy of a Monte Carlo simulation is “proportional to one over square root N” - the implication being that a reduction in the simulation uncertainty to $\frac{\delta}{k}$ requires $k^2 N$ histories.

1.3.2 Monte Carlo simulations in radiation transport

The Monte Carlo method used in the simulation of radiation transport employs computer generated random numbers and the probability distributions governing the individual interactions of electrons and photons [57]. More specifically, the Monte Carlo method provides a numerical solution to the Boltzmann transport equation that, as Bielajew [32] notes, directly uses the fundamental microscopic physical laws of electron-atom

and photon-atom interactions. As a large number of individual histories are modelled the result approaches the average scored quantity within the specified geometry - calculated to within a statistical uncertainty.

The efficiency (ε) of coupled photon-electron simulations is generally taken to be as follows,

$$\varepsilon = \frac{1}{T \cdot \sigma^2} \tag{1.12}$$

where *T* is the computational time needed to calculate the quantity of interest to within the statistical variance characterized by σ^2 [65,110,113].

Simulation methods which result in an increase in the efficiency, without introducing systematic errors in the calculation of the scored quantities, are generally referred to as variance reduction techniques (VRTs) [32]. The efficiency of a simulation can be increased by either reducing the variance or reducing the computational time per particle history. Kawrakow and Fipple [65] note that: (1) decreasing the variance per particle can be achieved, for example, by increasing the importance of particles that have a large influence on the scored quantity and (2) reducing the computing time per particle history by, for example, reusing certain quantities associated with a particle history, particle splitting or forcing an interaction.

1.3.2.1 Photon transport

The photon interaction processes at energies relevant to radiotherapy dosimetry (10 keV to 40 MeV) are pair production, Compton scattering, the photoelectric effect and Rayleigh scattering [58,59,90]. The physics associated with each interaction will not be presented here but instead an important link between the photon mean free path and the application of the Monte Carlo method in radiation therapy dosimetry is highlighted along with a very useful variance reduction technique.

The interaction distances of photons with energies between 10 keV and 40 MeV are of the order of 1 - 60 $g \cdot cm^{-2}$ for low Z materials such as water. The implication, with regards to Monte Carlo simulation of photon transport, is that many millions of photon histories can be modelled with modest computational resources [32]. The fact that any given photon will interact only a few times in macroscopic objects (such as water tank phantom) means that Monte Carlo simulations can be run to an acceptable level of statistical uncertainty - usually taken to be less than ± 1.0%. Although many millions of photon histories can be simulated there may be instances where an increase in the simulation efficiency would be desirable. One such case would be a detector geometry simulated in a typical water tank phantom geometry.

As noted above, to increase the efficiency of a simulation one can either increase the importance of particles that have a large influence on the scored quantity or force an interaction. One approach that combines

elements of both methods is photon cross section enhancement (XCSE). The XCSE variance reduction technique increases the photon cross section by a free parameter *b*>1 (i.e. “forces the interaction”) within a defined region which surrounds the volume of interest (i.e. “increase the importance of particles that have a large influence”). In practice the XCSE technique can be employed by using large XCSE factors in and around the simulated detector located within a water tank geometry (see Wulff *et al* [113] for examples of the efficiency gains associated with the XCSE variance reduction technique).

1.3.2.2 Charged particle transport

Electron and positron interactions relevant to Monte Carlo simulations used in radiotherapy and dosimetry are Møller scattering of electrons from atomic electrons, Bhabha scattering of positrons from atomic electrons, Bremsstrahlung photon generation, positron annihilation, elastic scattering and excitation of atoms and molecules by electrons and positrons. Again, the physics associated with each interaction process [58,59,90] is not presented in detail. Instead a brief description of the very important condensed history method of electron transport will be discussed.

In general, a relativistic electron will undergo between 10^5 and 10^6 individual interactions before slowing down. Faithfully simulating each electron interaction over the required number of individual histories would be impractical - due mainly to the required computational resources. Although an electron undergoes a large number of interactions the reality is that

relatively few of the individual interactions result in a great deal of energy loss or directional change [46,47]. Therefore, as Berger first proposed [9], one can combine the effects of many small interactions into a single condensed history. The cumulative effect of the individual interactions is taken into account by sampling, from appropriate multiple scattering distributions, the change in energy and direction of a particle at the end of the step.

Although the condensed history technique of charged particle transport has made radiotherapy relevant Monte Carlo simulations possible, the end user must be cognizant of the approximations being made and be wary of introducing systematic errors which result from the introduction of the condensed history step length parameter [12]. The step length parameter associated with a condensed history is used to control the maximum permitted fractional energy loss per step [63,64]. In the presence of interfaces between different materials and/or scoring regions the condensed history technique must also employ a boundary crossing algorithm [13,61].

In addition to the boundary crossing algorithms many Monte Carlo routines terminate the history of an electron when the transport range is such that it cannot possibly reach another boundary. In this instance the simulation deposits the residual energy in the current region. However, by terminating the history the possibility of a Bremsstrahlung photon being created and escaping from the region is eliminated as a potential event. To control this approximation an energy threshold is defined, above which no range

rejection is performed and therefore there is little loss in Bremsstrahlung photon creation [62].

1.3.3 Monte Carlo simulation in radiotherapy and dosimetry

In radiation therapy applications the Monte Carlo method can be used to simulate radiation transport within a specified geometry. Examples of the most common geometries simulated in radiation therapy dosimetry would be the medical linear accelerator head, radiation detectors and patient geometries derived from CT data sets. Developed as part of the OMEGA (Ottawa Madison Electron Gamma Algorithm) project [93], BEAM, DOSXYZ and DOSRZ are all user code additions to the original EGS4 Monte Carlo system [86]. The following is a brief overview of the BEAMnrc [94], DOSXYZnrc [109] and DOSRZnrc [95] user codes that utilize the updated EGSnrc Monte Carlo simulation package [67].

1.3.3.1 BEAMnrc, DOSXYZnrc and DOSRZnrc

BEAMnrc, originally referred to as BEAM, was designed to be used in the simulation of radiation transport within a geometry that represents the radiation therapy treatment unit – typically a medical linear accelerator [60]. The convention used in building a model of an accelerator head is to define the z-axis of the simulation as the beam central axis; this axis is then used as the origin for all other spatial requirements. One builds a BEAMnrc model of a linear accelerator head by configuring a series of component modules (CM) to dimensions provided by the manufacturer. Typical component

modules used in modelling an accelerator head are: SLABS, CONS3R, FLATFILT, CHAMBER and JAWS.

The primary output of a BEAMnrc simulation is a phase space file. This file contains information on all particles crossing the xy-plane located at a fixed point along the z-axis. The xy-plane is referred to as a scoring plane, where any number of scoring planes can be defined and located along the accelerator head z-axis. A phase space file contains information on each particle: the energy (E), the xy-position (X,Y), the direction cosines with respect to the x and y-axis (U,V), the direction cosine of the angle with respect to the z-axis (SIGN(W)), the particle weight (WT), the charge (IQ), the number of times the particle has crossed the scoring plane (NPASS) and other particle history information (LATCH) [94].

DOSXYZnrc is the most recent version of the original DOSXYZ user code. DOSXYZnrc facilitates the calculation of dose distributions within a rectilinear phantom [109]. The code allows sources such as monoenergetic diverging or parallel beams, phase-space data generated by BEAMnrc simulations, or a model-based beam reconstruction produced by BEAMDP [76]. Photon-electron transport is simulated in a Cartesian volume and energy deposition scored in designated volume elements (voxels). Each voxel is assigned a physical density that represents the true material confined to that volume element. The dimensions are variable yet are typically smaller than 1.0 mm x 1.0 mm x 1.0 mm. For any given simulation a phantom is configured as an array of voxels.

DOSRZnrc is one of a suite of EGSnrc user codes that provides the framework by which geometries can be defined in a cylindrical coordinate system about the z-axis [95]. In general, there are NZ slabs (or regions) which are defined by NZ + 1 planar boundaries - specified within the overall depth of ZBOUND. NR is used to represent the cylinder or ring number as defined by their outer radii - contained within an overall radii of RCYL. The cylinder or ring number is reflected about the axis of rotation and therefore provides a method of indexing each cylindrical volume element - referred to as a sub-region. Each sub-region is denoted by the radial and depth indices (IX,IZ) in the RZ space. The medium within each sub-region is initially set to the background material followed by the assignment of the other materials to specific regions. DOSRZnrc can be set to output the total dose in each region along with the total fractional dose due to electrons entering from the front, back, inside and outside walls of the region. Any fraction of the dose not accounted for by these four entrance walls is assumed to come from electrons that originated within the region itself.

1.3.3.2 Photon cross section enhancement

The photon cross section enhancement technique, as implemented in DOSRZnrc, is described here in a manner that closely follows the NRCC Report PIRS-702(revB) [95]. When a photon interaction is about to occur in a region with cross section enhancement, the incident photon is split into an interacting portion (*1/b*) and a non-interacting portion (*1-1/b*). All particles originating from the interaction carry the weight *w/b*, where *w* is the statistical weight of the original photon. Out of these particles all electrons are kept on

the computational stack and transported, all photons (including relaxation photons, Bremsstrahlung and annihilation photons from subsequent electron transport) are terminated with probability *1/b* so that, if they survive, they have again the weight *w*. The unscattered portion of the incident photon is also terminated with probability *1-1/b* making the weight of survivors *w*. All electrons set in motion in the cross section enhancement region carry the weight *w/b*. It should be noted that there are *b* times more such electrons compared to a normal transport than without cross section enhancement. Note, however, that if an electron that was set in motion outside the cross section enhancement region enters that region, it will have a weight of w_0 and therefore increase the statistical fluctuations. Therefore, in order to use this method effectively, it is a good idea to make the cross section enhancement region slightly larger than the region of interest so that no w_0 weighted electrons can make their way into the volume of interest.

1.3.4 Monte Carlo simulation in small field dosimetry

In an early work, Verhaegen *et al* [108] used the BEAM/EGS4 Monte Carlo code to evaluate the dosimetric characteristics of a 6 MV Clinac-600SR beam. At depths of 1.5 and 5.0 cm the authors reported no variation in stopping powers for field sizes between 1.5 and 5.0 cm and affirmed the use of measured detector ratios within this range as a method of obtaining dose ratios in water. However, they clearly note that for field sizes smaller than 1.5 cm, scatter factors show significant variation with measurement depth and Monte Carlo scoring volume.

For a 15 MV beam, Scott *et al* [98] used an unshielded diode (Scanditronix/IBA) and DOSXYZnrc to measure and simulate small field output factors. To simulate the active volume of the detector the authors use two silicon voxels with a 2.0 mm lateral dimension stacked one on top of the other (z = 0.06 and 0.44 mm respectively). For fields down to 1.5 cm the Monte Carlo results agree very well with experiment, yet for a 0.5 cm field the difference was found to be 4.5% high. The authors comment that this result was not expected as good agreement between modelled and measured profile and percent depth dose data had been achieved. In a subsequent publication, the authors continue their work [99] and investigate the impact simulated focal spot size has on source occlusion and therefore small field scatter factors. The general conclusion was that one should fine tune the modelled electron spot width using both penumbra data and small field output factors.

Francescon *et al* [44] combined experimental measurement and Monte Carlo simulation to estimate the total scatter factor (S_{cp}) for the 5.0, 7.5 and 10.0 mm Cyberknife collimators. The authors model the accelerator head, collimators and four different detectors for EGSnrc simulation. They then used experimental measurement and simulation to determine the incident electron energy and FWHM. With the incident electron parameters established, the authors provide Monte Carlo calculated correction factors for each detector.

At the time the thesis was started the preceding summary represented the current “state-of-affairs” regarding the application of Monte Carlo simulation in small field dosimetry. It was clear that Monte Carlo simulation was going to be a powerful tool in overcoming some of the challenges associated with small field dosimetry. The natural direction was to take the Alfonso *et al* formalism and implement it explicitly as a function of Monte Carlo calculated correction factors. That being said, one should recall that in the Alfonso *et al* paper the authors note that if $k_{Q_{clin},Q_{msr}}^{f_{clin},f_{msr}}$ is close to unity for a given detector then the ratio of readings would be sufficient for reporting small field relative output factors. The implication being that $k_{Q_{clin},Q_{msr}}^{f_{clin},f_{msr}}$ correction factors may not necessarily require Monte Carlo methods.

1.4 Aims and objectives of the research

The principal research question is:

> *“What are the requirements for accurate small field relative dosimetry?”*

In addition, the following research questions will be investigated:

- What are the characteristics associated with the experimental data required for the accurate implementation of the proposed small field dosimetry formalism?

- What level of Monte Carlo model validation is required for the accurate implementation of the proposed small field dosimetry formalism?

- What are the Monte Carlo calculated 6 MV small field replacement correction factors for a comprehensive set of diode detectors and are the correction factors sensitive to changes in the incident electron source parameterization?

- What level of detail is required in diode detector models to produce accurate correction factors?

- Is there an emerging detector technology well suited for small field relative output dosimetry?

- Can experimental methods and the reporting of small field dosimetric results be standardized?

1.5 Overview

The Alfonso *et al* paper outlines a well thought out dosimetry formalism for reporting corrected relative output for small and non-standard fields. However, many necessary questions regarding the implementation of the proposed formalism remained. The main body of this thesis describes the original work undertaken to address some of the outstanding details regarding the proposed formalism. The thesis work is clearly novel, as evidenced by the associated publications, and covers both experimental methods and the use of Monte Carlo simulation.

The chapters are presented in a chronological order that follows the research path and publication trail. As such, each chapter includes references to other published works that were current at the time the associated manuscript was written. Presenting the thesis material in this manner will provide the reader insight into the developments associated with small field dosimetry that were being published by other investigators during the course of this project. The thesis is organized in the following manner.

- **Chapter 2: Experimental small field 6 MV output ratio analysis for various diode detector and accelerator combinations**

    - Characterize the experimental data required for the accurate implementation of the proposed small field dosimetry formalism.

- Show the difference in measured output ratio as a function of diode detector and accelerator head design.
- Investigate the differences in the delivery precision as a function of linac head design and collimation.

- **Chapter 3: Implementing a Monte Carlo based small field dosimetry formalism for a comprehensive set of diode detectors**

  - Systematically show the steps required to benchmark a combined linear accelerator and detector model for use in the proposed small field dosimetry formalism.
  - Present the Monte Carlo calculated $k_{Q_{clin},Q_{msr}}^{f_{clin},f_{msr}}$ correction factors for a comprehensive set of diode detectors.

- **Chapter 4: Diode detector model simplification for Monte Carlo small field photon dosimetry and correction factor sensitivity to source parameterization**

  - Establish the level of detector detail required for the accurate implementation of the proposed formalism.
  - Investigate the sensitivity of the calculated correction factors to linear accelerator source parameterization.
  - Highlight the influence of volume averaging and the importance of reporting correction factors back to a point like volume.

- **Chapter 5: Small field dosimetric characterization of a new 160-leaf MLC**

    - Revisit the experimental data required for the accurate implementation of the proposed small field dosimetry formalism for a new MLC design.
    - Explore the use of a scintillator based dosimetry system as a means of experimentally determining the $k_{Q_{clin},Q_{msr}}^{f_{clin},f_{msr}}$ correction factors for a set of diode detectors.
    - Report experimental characterization of the penumbral width as a function of collimation design as well as field size changes for various collimator rotational angles.

- **Chapter 6: A methodological approach to reporting corrected small field relative outputs**

    - Address the issue of field size as used in the proposed small field dosimetry formalism.
    - Present a field size metric which can be used to appropriately correlate relative output to the measured dosimetric field size.
    - Explore the suitability of applying published $k_{Q_{clin},Q_{msr}}^{f_{clin},f_{msr}}$ correction factors across a population of linacs.

General conclusions of the work will be summarized in the last chapter, along with a discussion on whether the research aims were achieved. The

impact and novel contributions of the thesis will be highlighted and an up-to-date literature review presented. Suggestions for future work are also given.

Chapter 2
Experimental small field 6 MV output ratio analysis for various diode detector and accelerator combinations

2.1 Introduction

It is widely accepted that for field sizes smaller than 3.0 cm x 3.0 cm output factors cannot be measured with the same level of accuracy and precision required when performing standard clinical dosimetry. The challenges associated with small field dosimetry can be directly related to source occlusion, lateral charged particle disequilibrium and non-negligible detector perturbations.

Detector selection for small field output dosimetry is clearly problematic. Laud *et al* [71] emphasize high spatial resolution and water equivalence as attributes desirable in a small field dosimeter. The authors note that one can expect an underestimation in measured relative output from ionization chambers, due to an increase in lateral electronic disequilibrium, and an overestimation in measured relative output from diode detectors, due to the high atomic number of the active layer and the surrounding silicon substrate. Alanine-EPR [10,20] and plastic scintillation dosimeters [8,68,69,111] have shown promise but require specialized equipment and are generally not available for routine clinical use.

The goal of this work was to measure 6 MV small field, detector specific, output ratios (OR_{det}) using the SFD and the PTW T60008, T60012, T60016 and T60017 field diodes on both a Varian iX and Elekta Synergy accelerator, to estimate the Type-A standard uncertainty and characterize the measurement precision.

2.2 Methods

Commercial diode detectors are generally categorized into two types: shielded (photon) and unshielded (electron). As Griessbach *et al* [48] explain, shielded diodes have a shield of high atomic number placed at the backside (T60008) or surrounding (T60016) the silicon chip. The shielding eliminates the disproportionate number of low-energy scattered photons responsible for diode detector over-response in large fields. In unshielded diodes the shielding material is replaced with a polymer plastic [80] and therefore eliminates the excessive electron backscatter from the shield into the active volume. The set of diode detectors used in this study were of both types, with the T60008 and T60016 being shielded and the SFD, T60012, and T60017 being unshielded. These diodes were selected as they each have a similar active area quoted by the manufacturers at ≤ 1.0 mm^2. The silicon chip used in the photon field diode (PFD) and electron field diode (EFD) has a quoted diameter of 2.0 mm and suffers from significant volume averaging uncertainty at the smallest field sizes, and therefore they were not used in this study.

Measurements were performed on a Varian iX and an Elekta Synergy medical linear accelerator (linac) at a nominal 6 MV beam energy. Field size was set using the standard collimators; jaws only on the Varian linac and the combination of MLCi2 and diaphragm for the Elekta - noting that the Elekta design replaces the upper diaphragm pair with the MLC. A mean output ratio was calculated for each detector-linac combination at nominal square field sizes of 3.0, 1.0, 0.9, 0.8, 0.7, 0.6 and 0.5 cm with respect to a square field size of 5.0 cm. Measurements were made at depths of 1.5, 5.0 and 10.0 cm with the long axis of the detector parallel to the beam axis such that the active volume was positioned at isocenter. Positional fine tuning was performed to ensure the active volume was centred on the beam central axis and not just the light field.

The water tank phantom used with each linac was different. Initial Varian iX measurements were made in a scanning water tank that incorporated a stepper motor driven linear actuator (Ultra Motion Inc., Cutchogue, NY) having a quoted positional accuracy of ±0.001 mm/step. However, the positional accuracy perpendicular to the actuator axis was estimated at ± 0.2 mm, therefore output measurements were repeated in a smaller water phantom which provided a comparable ± 0.2 mm positional accuracy. The Elekta Synergy measurements were made using a PTW MP3 scanning water tank. This device has a quoted positional accuracy of ± 0.1 mm. The positional accuracy on both systems is estimated to be better than ± 0.2 mm.

Measurements were repeated three times with the water phantom, detector position and jaw/collimator reset between each experimental session. Five readings were taken for each field size during each experimental session. To characterize the Type-A uncertainty associated with experimental set-up, the standard error on the mean detector output ratio was calculated across the three experimental sessions [77,78]. The coefficient of variation (CV) was [85] calculated over the five readings from each experimental session, with the average CV calculated across the three independent experimental sessions.

This approach characterizes the measurement precision associated with the performance of the detector-linac system alone, which is better represented by the uncertainty on the mean OR_{det} across the three experimental sessions. Using this methodology identifies two distinct Type-A uncertainty contributions: one due to detector and beam fluctuations (with a constant set-up) and another due to re-establishing the entire set-up. If one assumes the repeated readings follow a normal distribution then a coverage factor k = 2.0 would provide a 95% confidence interval. However, given the sample size used in this study it is more appropriate to evaluate the Type-A uncertainty coverage using the t-distribution [78,85]. Therefore a coverage factor k = 2.0 provides a more representative confidence interval of 90%.

Another set of measurements were made to investigate the influence of jaw position accuracy on OR_{det} precision. A set of five readings were taken during the last experimental session with the jaws (Varian) or

MLC/diaphragms (Elekta) repositioned between each reading. The CV was then calculated using the five readings and compared to the CV value with no collimator repositioning. By not changing the detector and phantom set-up the jaw position accuracy, as it relates to relative output precision, was isolated.

The Varian iX measurements were repeated using the Millennium MLC. OR_{det} were measured using the T60017 diode at d = 5.0 cm with and without the MLC used in the collimation. An initial set of measurements were made with X-jaw and MLC leaves set to give the same field size. The X-jaw field width was then increased by 1.0 and 2.0 mm larger than the field width defined by the MLC. The aim was to remove the effect of the positional error in the X-jaw while still minimizing the tongue-and-groove leakage. In all cases the Y-jaw position was unchanged.

The Elekta MLC is positioned by the control system using a leaf off-set factor. The baseline leaf off-set is determined during an MLC calibration procedure yet can be adjusted to change each leaf-bank position relative to the calibration value. T60017 measurements at d = 5.0 cm were repeated to investigate the change in small field output as a function of leaf off-set away from the calibration value.

2.3 Results

Shown in Figures 2.1 and 2.2 are the mean OR_{det} values at each depth for all detector-linac combinations. For field sizes smaller than 3.0 cm the measured OR_{det} were not consistent across all detectors. However, there does appear to be a grouping in OR_{det} correlated to detector design - with the T60008 and T60016 being shielded and the SFD, T60012 and T60017 being unshielded. This is not unexpected as the shielded diodes do have a metal shield and are likely to have a greater response than unshielded diodes at small field sizes, where low-energy scattered photons are not so significant. Although the SFD, T60012 and T60017 are all categorized as unshielded diodes, the SFD measured OR_{det} were generally less than those measured with the T60012 and T60017. As this difference was consistent across both linacs, the indication would be that there are detector differences influencing OR_{det} measurement at small field sizes.

Plotted in Figures 2.3 and 2.4 are the percent uncertainties associated with the data shown in Figures 2.1 and 2.2. The uncertainty was found to be consistent across all detector-linac combinations. For square field sizes of 3.0, 1.0 and 0.5 cm, the standard uncertainty was generally less than ±0.25%, ±0.50% and ±1.25% respectively. However, this was not the case for every instance and validates the assumption that the predominant source of experimental uncertainty was geometric and associated with the change in water phantom and detector position as well as the collimator resetting.

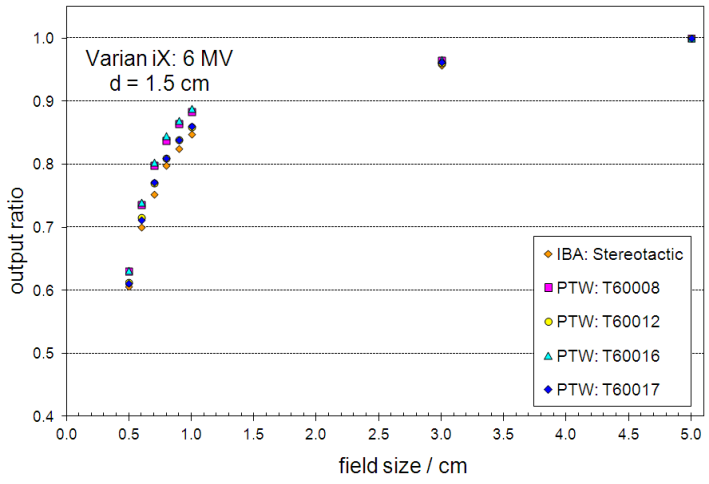

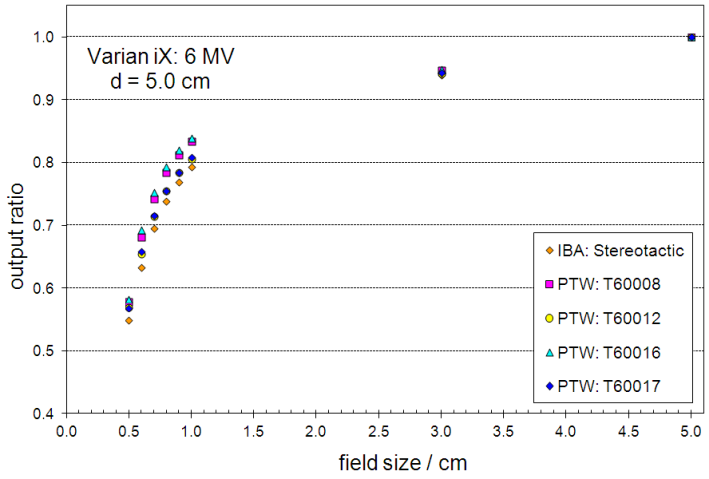

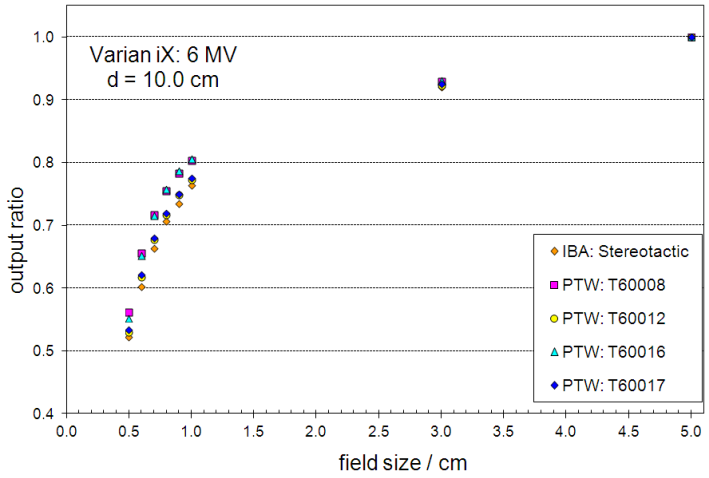

Figure 2.1 Shown above are isocentric detector output ratios measured with respect to a 5.0 cm square field size at d = 1.5, 5.0 and 10.0 cm for the Varian iX.

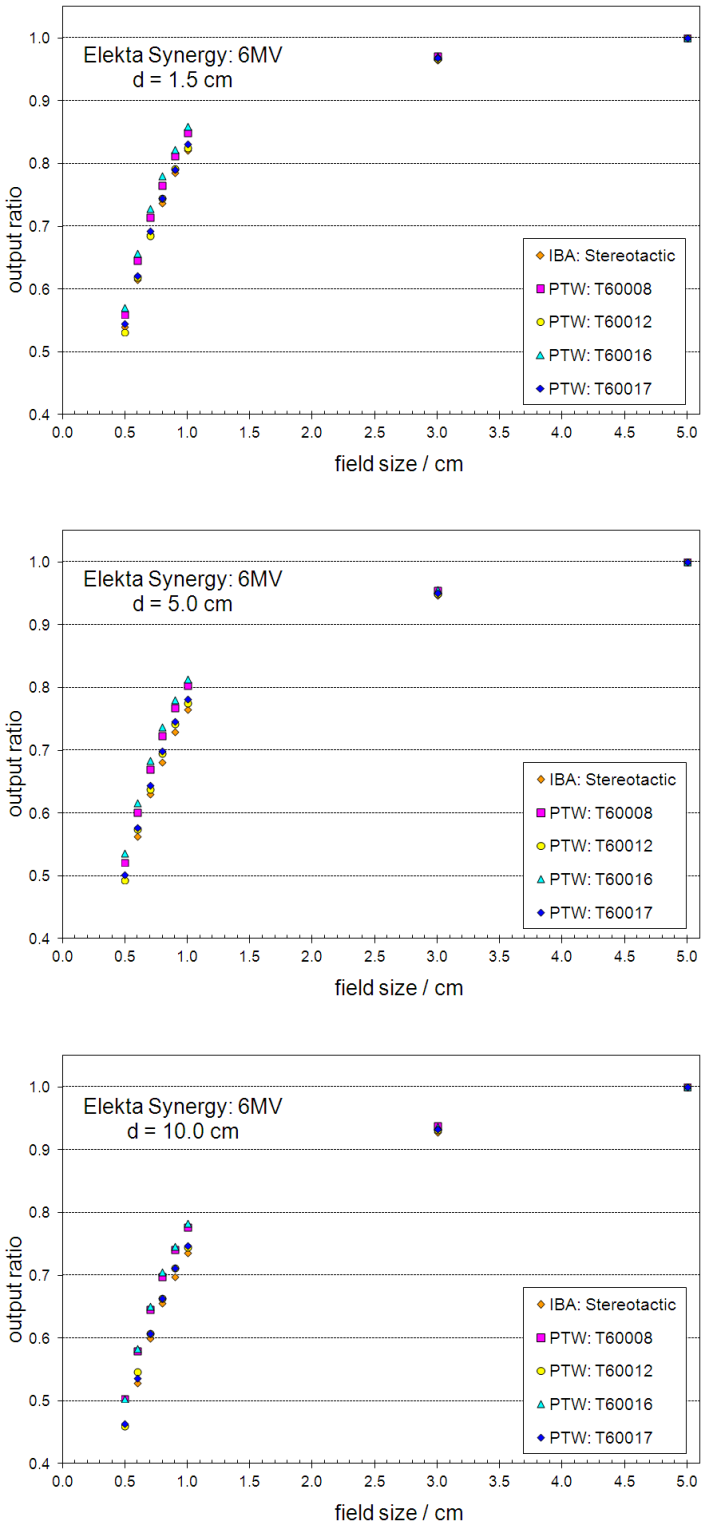

Figure 2.2 Shown above are isocentric detector output ratios measured with respect to a 5.0 cm square field size at d = 1.5, 5.0 and 10.0 cm for the Elekta Synergy.

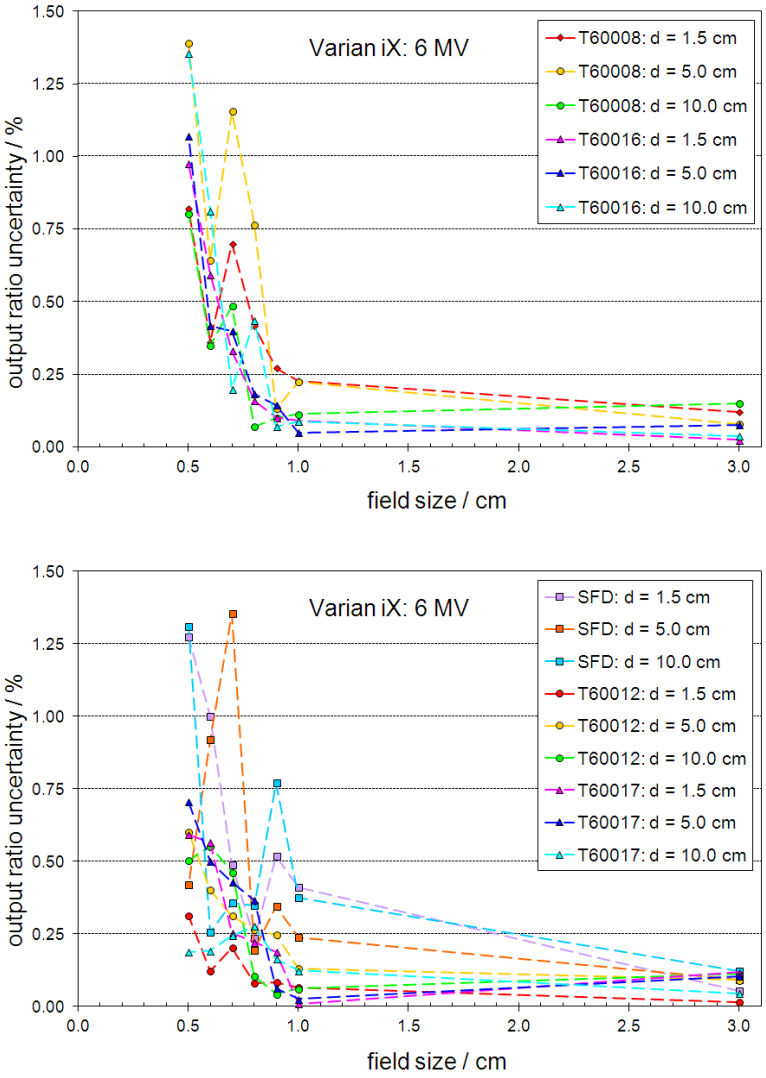

Figure 2.3 Shown above are the standard percent uncertainties associated with the experimental output ratios shown in Figure 2.1.

Plotted in Figures 2.5 and 2.6 are the average CV for each detector-linac combination calculated across the three independent measurement sets. At field sizes greater than 1.0 cm, the average CV ranged between 0.03% and 0.08% - yet was very nearly constant for any one detector-linac combination. As the field size was reduced to 0.5 cm, the CV did reveal a modest increase to 0.10% for the Varian linac. However, for the same field size reduction the CV revealed an increase to more than 0.15% for the Elekta.

The greater CV increase is thought to be the result of variations in the electron spot size and/or shape incident on the target but may also be due, in part, to an initial source wobbling as report by Sonke *et al* [103].

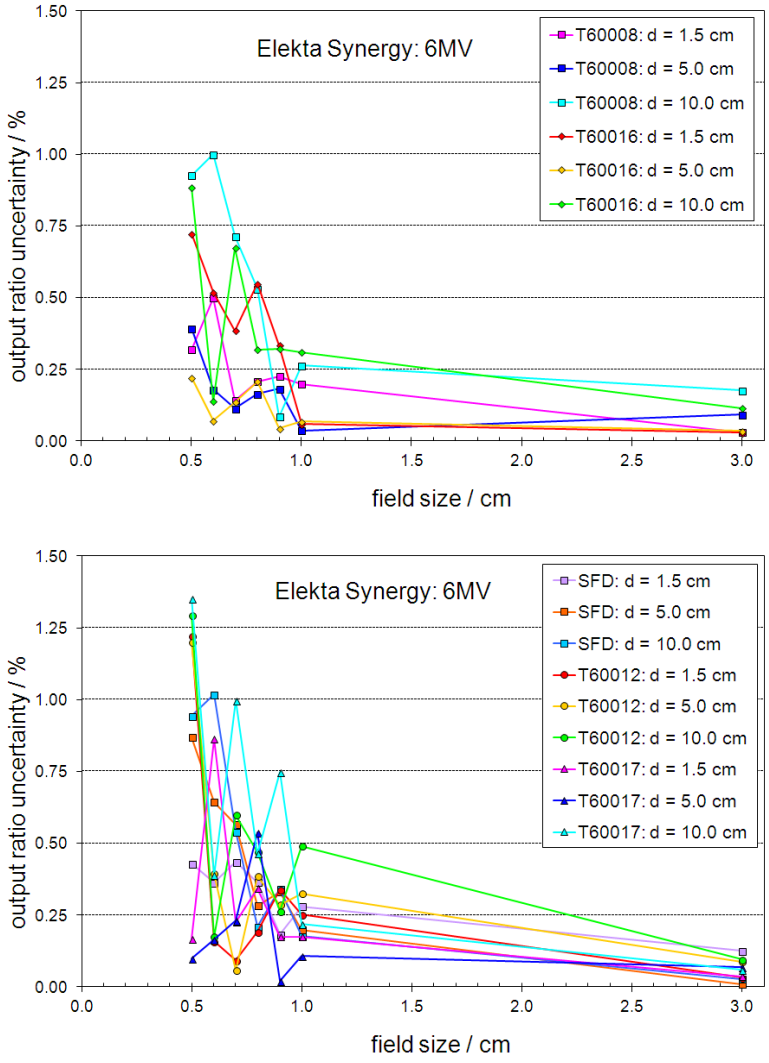

Figure 2.4 Shown above are the standard percent uncertainties associated with the experimental output ratios shown in Figure 2.2.

The CV for each detector-linac combination with the collimators repositioned between each of the 5 readings is shown in Figures 2.7 and 2.8. A paired t-test showed that all the Elekta data sets, except for the SFD and T60017

data at d = 10.0 cm, are statistically equivalent to the data acquired with the collimation position unchanged. This was clearly not the case for the Varian measurements which showed an 8-fold increase in the CV at the smallest field sizes. Clearly the positional accuracy of the Varian jaw is problematic at field sizes smaller than 0.7 cm. To investigate this further, we recorded the jaw position primary read-out for square field sizes from 0.5 cm to 30 cm.

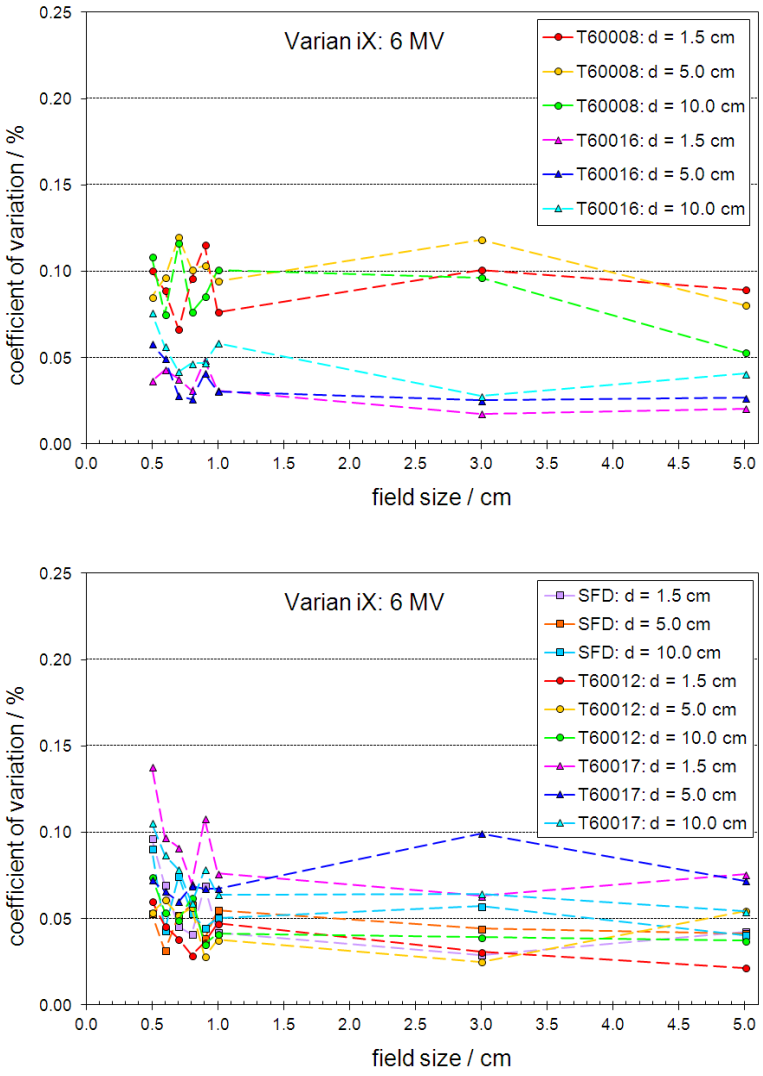

Figure 2.5 Plotted above are the average CV for each detector calculated across the three independent measurement sets made on the Varian linac.

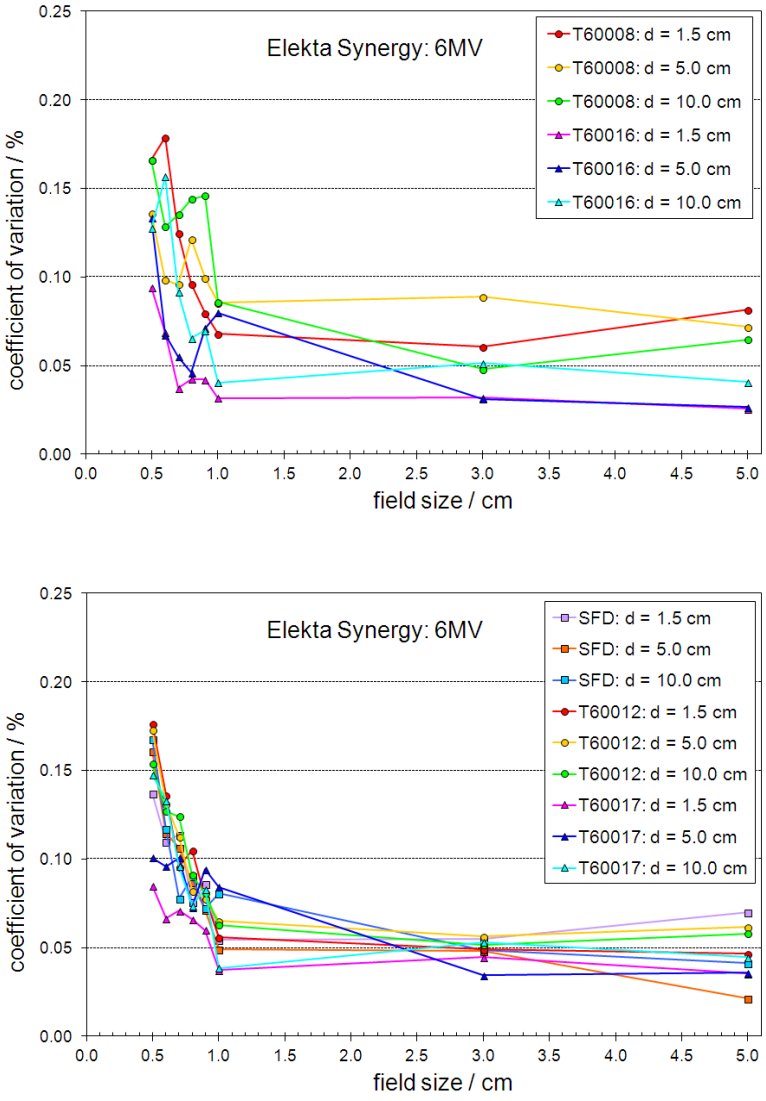

Figure 2.6 Plotted above are the average CV for each detector calculated across the three independent measurement sets made on the Elekta linac.

The primary read-out displays the voltage back to the control system from the primary potentiometer used to track the jaw position. The control system resolves the potentiometer voltage to ± 0.001 V, which correlates to a positional accuracy of ± 0.25 mm for the X-jaw and ± 0.57 mm for the Y-jaw. The difference in positional accuracy results, in part, from using a potentiometer with a fixed range (-8.0 to + 8.0 V) in combination with jaw

pairs which have different travel limits: X-jaw travel limits are -2.0 cm to 20.0 cm, Y-jaw travel limits are -10.0 cm to 20.0 cm. Shown in Figure 2.9 is the primary voltage read-out plotted as a function of jaw position for square field sizes of side 0.5 cm to 30 cm.

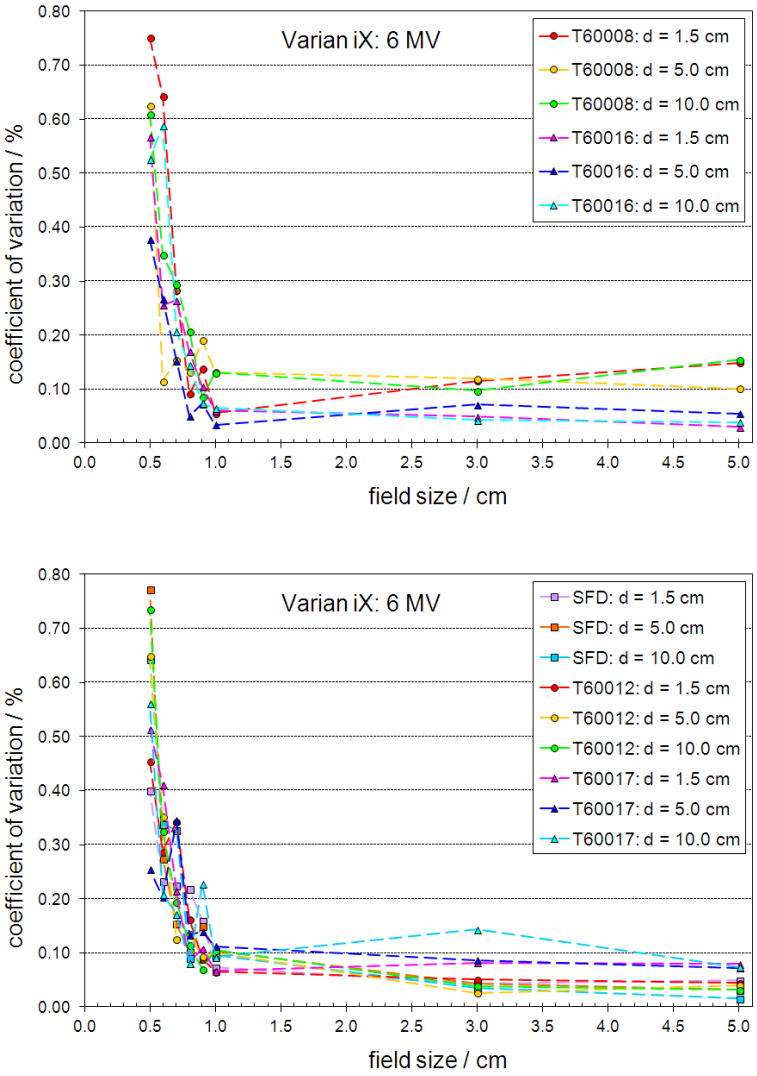

Figure 2.7 Plotted above is the CV calculated for Varian linac when the collimating system was repositioned between each of the 5 readings.

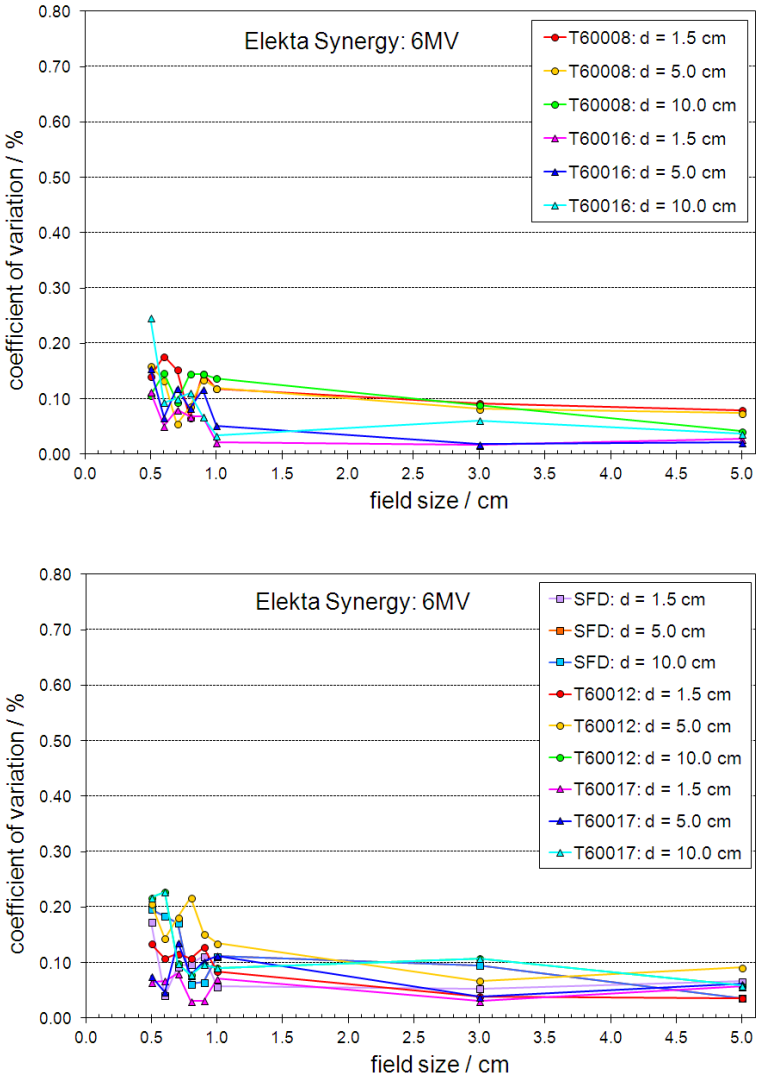

Figure 2.8 Plotted above is the CV calculated for Elekta linac when the collimating system was repositioned between each of the 5 readings.

Shown in Figure 2.10 is the percent increase in relative output on the Varian linac with the X-jaw located in line and back from the MLC leaf tips. The data shows there is very little difference in output when using the jaws alone or together with the MLCs - when both define the same field size. As one would expect, when the X-jaw was set back from the MLC leaf tip, the relative output increased. With the X-jaw set back by 2.0 mm, the leaf-tip leakage was non-negligible and resulted in an output increase of nearly 8%. The X-

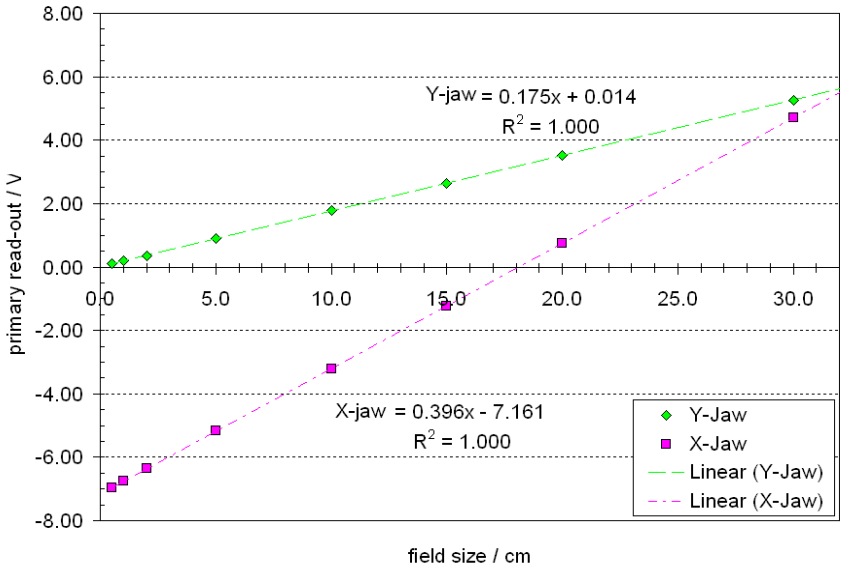

Figure 2.9 The primary voltage read-out on the Varian iX plotted as a function jaw position for square field sizes of side 0.5 cm to 30 cm.

Jaw was then repositioned between each of the five readings and CV calculated as before. One can see in Figure 2.11 that with the X-jaw set back from the MLC leaf tips by 2.0 mm, the OR_{det} precision improved to a level consistent with that associated with no X-jaw repositioning.

Shown in Figure 2.12 is the percentage difference between the original Elekta OR_{det} data obtained using the baseline MLC off-set and that measured as a function of leaf off-set adjustment (-10, -5, 0, 5, 10). For field sizes smaller than 1.0 cm x 1.0 cm a realistic change in leaf off-set up to 10 units can produce significant change in OR_{det}. Clearly the greatest change in OR_{det}, as a function of leaf off-set, occurs for the smallest field sizes. One can see that a negative offset, which produces a smaller field size, results in

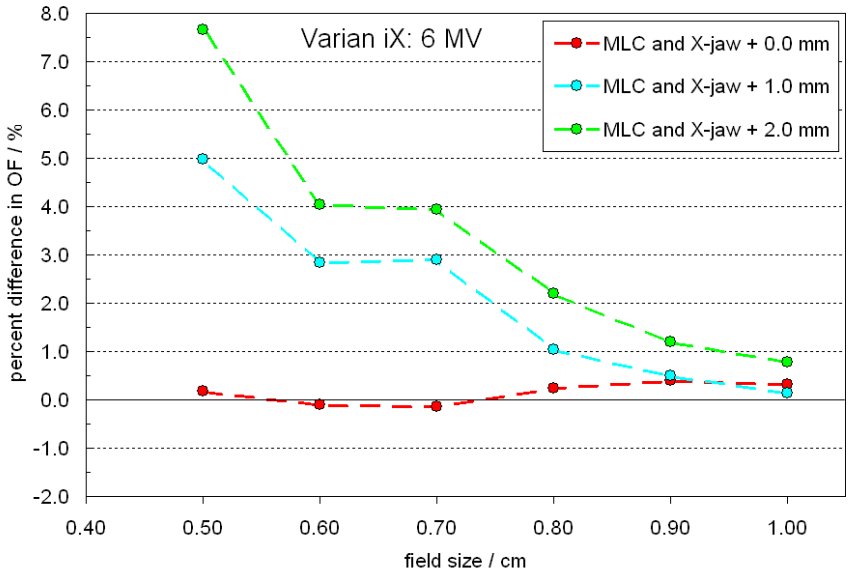

Figure 2.10 Percentage increase in OR_{det} as a function of field size for X-jaw positions set inline and back from the MLC leaf tip.

a greater OR_{det} difference than an equivalent positive offset. This difference is due to the increased source occlusion that occurs for the smallest field size [5,33]. Although the Elekta collimation system appears to have a greater positional precision the output ratio accuracy requires a nearly constant leaf off-set.

2.2 Discussion

As the focus of this portion of the work is on relative output measurement characterization one cannot overlook the problem systematic differences between the nominal and actual field size have on reporting experimental OR_{det} values. Sub-millimetre field size differences do not produce dissimilar

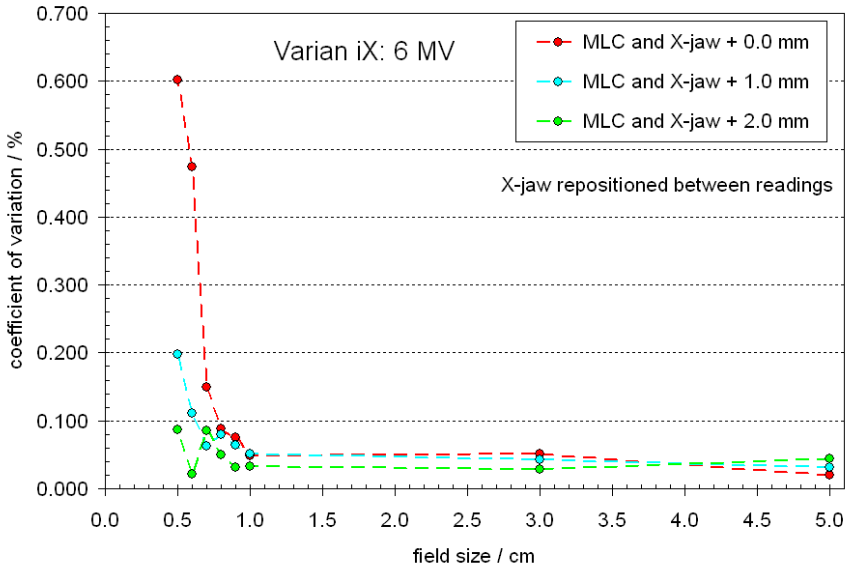

Figure 2.11 Plotted are CV values for measurements taken with the X-jaw located in line and back from the MLC leaf tips.

OR_{det} for large field sizes. However, that is clearly not the case for the small fields, where just such a difference will produce significant change in output. To address this we made accurate profile measurements for square field sizes smaller than 1.0 cm on the Varian linac using the SFD in combination with the linear actuator device. In all cases the measured field sizes were systematically smaller than the nominal by 0.5 mm (at the 50% level) [33]. As this appears to be a common attribute of Varian jaw collimation [98], reporting output as a function of field size is clearly problematic. We have chosen to report our data with respect to the nominal field size and emphasize this detail should be taken into consideration when reporting and assessing small field output data. In any case, accurate profile measurements and uncertainty analysis of collimator position must be considered when presenting small field output factor data.

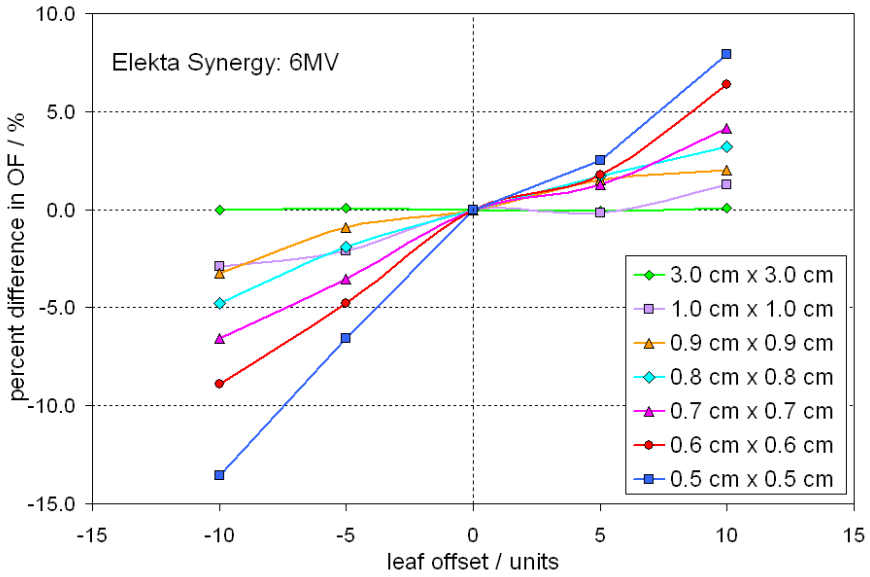

Figure 2.12 Shown above is the percent difference in OR_{det} for the Elekta Synergy 6 MV as a function of leaf offset adjustment away from the baseline established during MLC leaf calibration.

There were also differences in the measured OR_{det} as a function of detector design [79]. The results presented by Daşu *et al* [34], McKerracher and Thwaites [81,82,83] and Sauer and Wilbert [97] all suggest that a shielded diode will over respond by a greater amount than an unshielded diode when measuring small field relative output (only the PFD, EFD and SFD diodes were investigated by these authors). We find the PTW shielded diodes also over-respond in the small fields which, as Griessbach *et al* [48] explains, is predominantly due to the metal shield placed behind the silicon chip. However, regardless of diode choice the measured output ratios do not represent the total scatter factors. In short, there is a systematic difference between the measured relative output and the total scatter factor for small fields. It would appear that there exists no means by which to derive the diode detector specific correction factors from the measurements alone and

therefore an independent approach such as Monte Carlo simulation would be required.

Alfonso *et al* [1] has proposed a Monte Carlo based formalism for reference dosimetry of small and nonstandard fields. The convention is to multiply the ratio of detector readings by a Monte Carlo calculated correction factor, which accounts for the difference in detector response as a function of field size. Although the application of Monte Carlo simulation in small field dosimetry appears to be gaining favour within the community, Das *et al* note that one cannot assume Monte Carlo simulation will provide a gold standard without the appropriate experimental validation. Francescon *et al* [44] combined experiment and Monte Carlo simulation to determine correction factors for a selection of detectors used to measure output factors for the Cyberknife 5.0, 7.5 and 10.0 mm collimators. However, it would appear the authors only made one set of experimental measurements at a single depth and therefore did not fully characterize the associated experimental uncertainty. The experimental output ratio analysis presented here provides the additional information required for accurate Monte Carlo model validation.

4.5 Conclusion

Unlike other studies that present output factor data measured on a single treatment machine using a disparate selection of detectors, we have

presented OR_{det} data measured with shielded and unshielded diodes on two different linear accelerator head designs. The characterization clearly shows there are differences in the small field OR_{det} between shielded and unshielded diodes and differences in the associated delivery precision as a function of linac design.

Chapter 3
Implementing a Monte Carlo based small field dosimetry formalism for a comprehensive set of diode detectors

3.1 Introduction

The work presented in Chapter 2 and that of Heydarian *et al* [52], McKerracher and Thwaites [79], Sauer and Wilbert [97] have added to the body of knowledge with respect to experimental small field dosimetry. Yet each author notes there are limitations associated with experimental small field dosimetry and suggest that Monte Carlo simulations are required to develop a complete understanding of small field dosimetry.

Monte Carlo simulation can be a powerful tool in overcoming some of the challenges associated with small field dosimetry. As noted earlier, Alfonso *et al* [1] propose a field factor that converts the absorbed dose to water for the machine-specific reference field (f_{msr}), with a beam quality (Q_{msr}), to the absorbed dose to water for the clinical field size of interest (f_{clin}) of beam quality (Q_{clin}). The authors note that the field factors can be calculated using Monte Carlo simulation alone but can also be measured as the ratio of detector readings multiplied by detector specific Monte Carlo calculated correction factors. The later is an attractive approach as it combines experimental data with correction factors calculated using detailed detector

simulations, thereby reducing the potential for systematic errors in a Monte Carlo only approach.

The goal of this portion of the work was to implement the newly proposed small field dosimetry formalism for a comprehensive set of diode detectors. The source parameters of a BEAMnrc modelled Varian 6 MV linac head were first fine-tuned using profile data. A comprehensive set of commercial diode detectors were modelled using DOSRZnrc and the combined linac-detector simulations validated against experiment. The relative small field output factors in water, and detector specific correction factors, were then calculated according to the newly proposed formalism.

3.2 Methods

3.2.1 Experimental measurements

The first step in benchmarking any Monte Carlo linac model is to acquire good data. The positional uncertainty of the Wellhöfer water tank system was evaluated to determine if it could be used for small field profile measurements. The differences between the water tank controller displayed position and the actual measured position was assessed for positional step sizes of 0.01, 0.03 and 0.05 cm. The difference was found to be consistent with the positional uncertainty quoted by the manufacturer at ± 0.2 mm (See Figure 3.1).

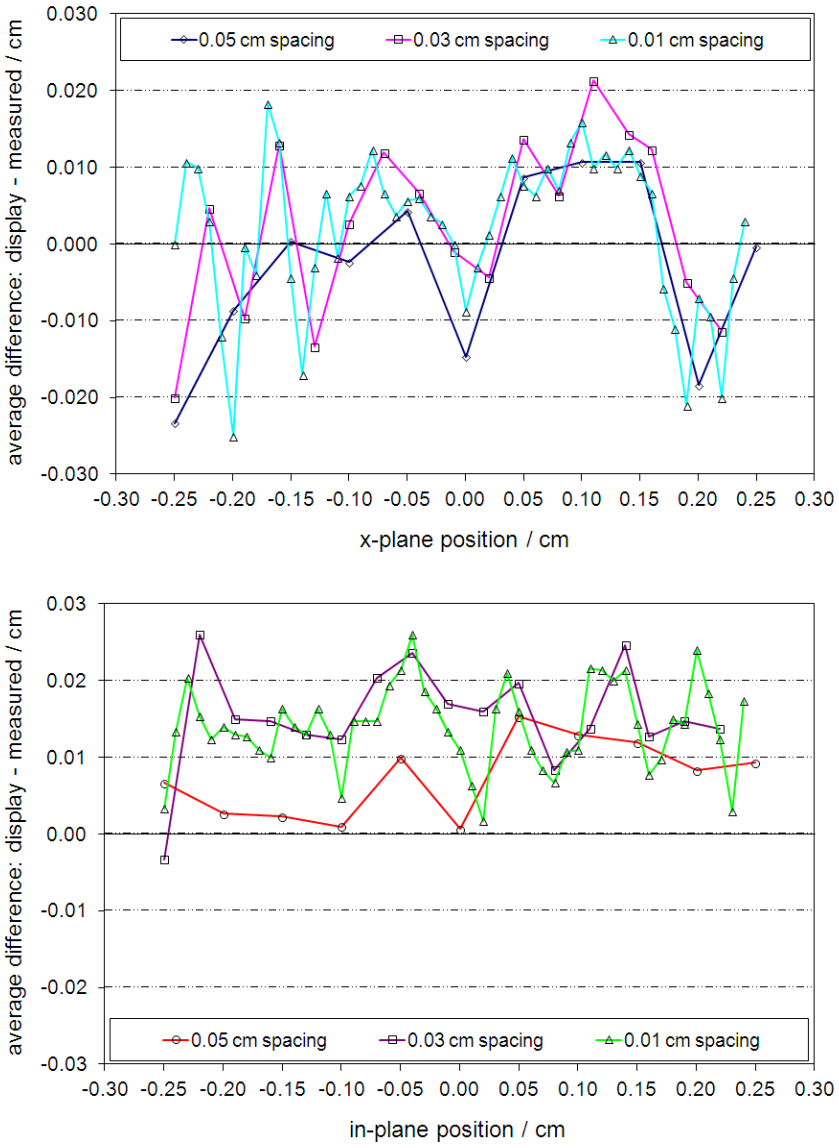

Figure 3.1 Water tank positional test results averaged over three measured data sets. The results can be thought of as representing the average detector position for multiple profile measurements for a square field size of side 0.5 cm taken with a positional resolution of 0.01, 0.03 and 0.05 cm.

This level of positional uncertainty was deemed unacceptable and would have introduced errors in the small field penumbral widths. A stepper motor

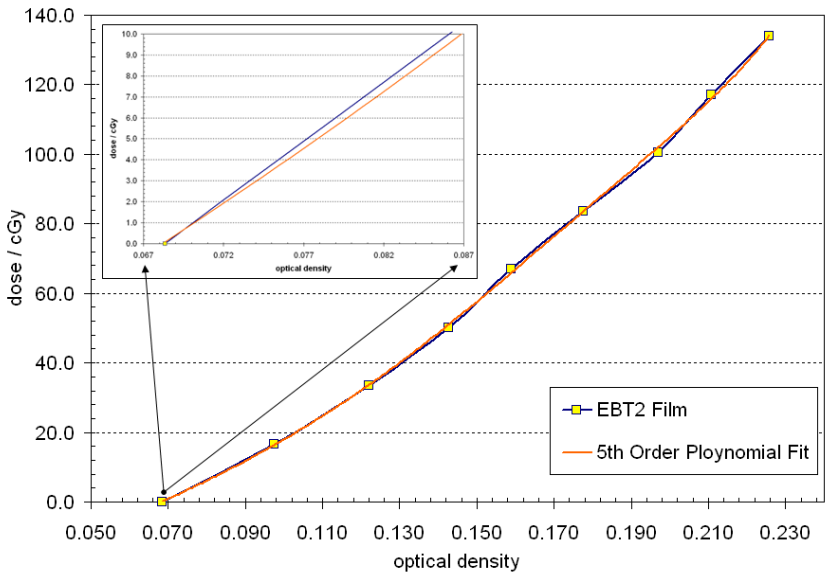

Figure 3.2 EBT2 film calibration curve and 5th order polynomial fit.

driven linear actuator (Ultra Motion Inc.) was incorporated into our water tank to minimize the influence of positional errors. With a manufacturer quoted positional accuracy of ±0.001 mm/step, the uncertainty in detector position was reduced to less than the standard ±0.1 mm quoted by most water tank manufacturers.

The stereotactic field diode (SFD) from Scanditronix/IBA was used to acquire profile data in water at a depth of 10.0 cm. This was performed for nominal jaw collimated square field sizes of sides 0.5, 0.6, 0.7, 0.8, 0.9 and 1.0 cm. EBT2 film was used to corroborate the SFD measurement (see Figure 3.2 for film calibration curve). A central profile was acquired using the film and compared to the SFD measurements. The film did suffer moderately from the documented spatial non-uniformity [49] but was intended to substantiate the diode measurements and, in turn, validate the profile

equivalence between the SFD measured profiles and a best estimate of the actual beam profile in water.

Experimental detector specific output ratios are defined as the ratio of detector readings (*M*) taken between the clinical field size of interest (f_{clin}) and the machine-specific reference field (f_{msr}) such that,

$$OR_{det}^{f_{clin}} = \frac{M_{Q_{clin}}^{f_{clin}}}{M_{Q_{msr}}^{f_{msr}}} . \qquad (3.1)$$

$OR_{det}^{f_{clin}}$ values were measured using the SFD, T60008, T60012, T60016 and T60017 field diodes for the same small field sizes. Five isocentric experimental readings were taken at depths of 1.5, 5.0 and 10.0 cm. This was repeated during three independent experimental sessions and used to calculate an average experimental value. All experimental $OR_{det}^{f_{clin}}$ values were taken relative to a machine-specific reference field of 5.0 cm x 5.0 cm, which is common practice for small field dosimetry, where an intermediate reference field is used to relate small field output to the conventional reference field size of 10.0 cm x 10.0 cm. A thorough evaluation of the experimental uncertainties associated with the small field output ratio measurements were presented in Chapter 2.

3.2.2 BEAMnrc and DOSXYZnrc simulations

A BEAMnrc model of a Varian 2100 series linear accelerator head, originally commissioned in a manner consistent with TG-105 [22], was used as the starting point [6]. The original electron source parameters were as follows: 6.2 MeV mono-energetic with a circularly symmetric Gaussian FWHM = 0.140 cm. Although the original electron FWHM was consistent with that measured by Sham *et al* [101] some question remained concerning the application of this model for small field dosimetry.

Small field profile data was used as an initial surrogate for determining the incident electron energy and FWHM. A series of simulations were run with the following electron energy and Gaussian FWHM combinations: 6.0, 6.1 and 6.2 MeV with the FWHM decreased in steps of 0.010 cm from 0.150 to 0.100 cm. The initial history number was set at 2.5 x 10^7. Selective Bremsstrahlung splitting (SBS) was used with a maximum splitting number of 1000 in place of directional Bremsstrahlung splitting (DBS). This was done to avoid complications associated with fat photon [66] dose scored to the monitor unit chamber. Phase space (PHSP) data was scored above the linac jaws, denoted as a $BEAM_A$ simulation (See Appendix A.1). Each $PHSP_A$, with a total particle count of approximately 1.0 x 10^9, was used as the source for the field size specific $BEAM_B$ simulations (See Appendix A.2). The azimuthal particle redistribution method developed by Bush *et al* [14] was used to reduce the latent phase space uncertainty and provided a much more uniform particle distribution across the small fields (See Figure 3.3).

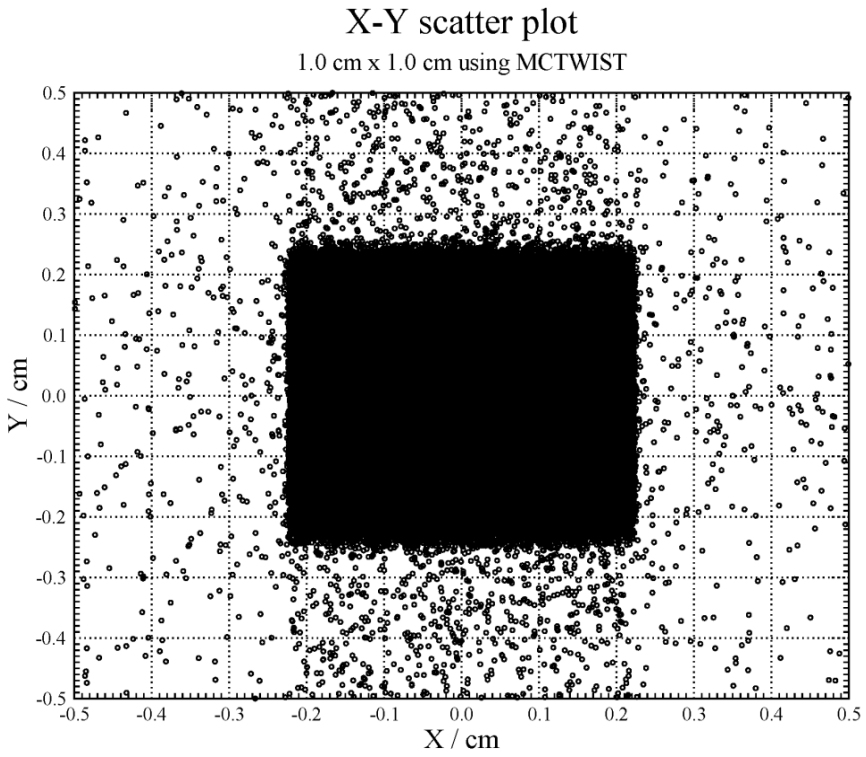

Figure 3.3 A BEAMDP [76] scatter plot generated from a 1.0 cm x 1.0 cm $PHSP_B$ file scored directly below the lowest jaw. $PHSP_A$ was redistributed using the MCTWIST component module.

DOSXYZnrc simulations were run with the history number set to give a statistical uncertainty less than ± 0.5% within a voxel dimension of 0.05 cm x 0.05 cm x 0.25 cm (See Appendix A.3). Profile data was first evaluated for nominal square field sizes of side 0.5 and 1.0 cm. This helped to establish which source parameters resulted in data consistent with experiment and that which were obviously inconsistent. The remaining field sizes were then simulated and compared to experiment.

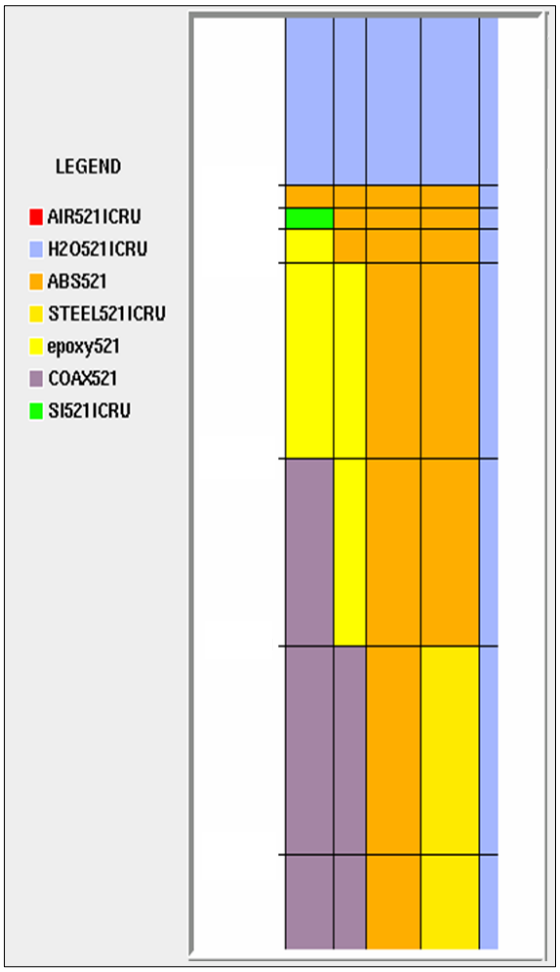

Figure 3.4 The stereotactic field diode as modelled in DOSRZnrc [95] but without dimensions so as not to breach the non-disclosure agreement with Scanditronix/IBA.

3.2.3 DOSRZnrc diode detector modelling

Commercial diode detectors are typically designated as shielded (photon) or unshielded (electron), with the shielded diodes having a layer of high atomic number material just behind (T60008) or surrounding (T60016) the silicon chip. The set of diode detectors used in this study were of both types, with the T60008 and T60016 being shielded and the SFD, T60012, and T60017

being unshielded. These diodes were selected as they each have a similar active area quoted by the manufacturers at ≤ 1.0 mm^2.

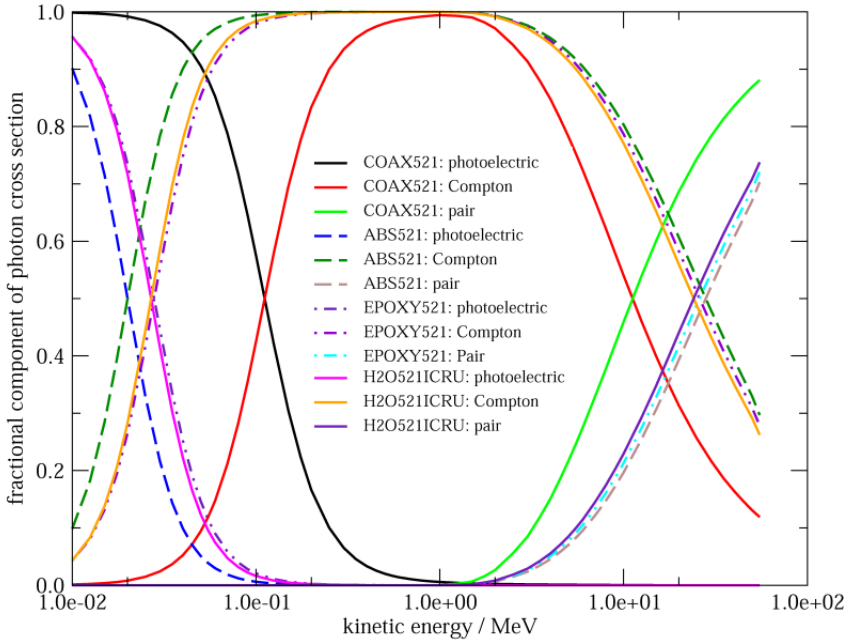

Figure 3.5 Photon cross-section data generated from the PEGS4 data created for the coaxial cable, epoxy and ABS plastic materials [67].

Detailed drawings supplied by each vendor were used to model the detector geometries in DOSRZnrc [17,95]. Figure 3.4 shows the SFD geometry but in general each detector model included the stainless steel stem, coaxial cable, active volume modelled as pure silicon, a housing/enclosure material (ABS and/or epoxy) and a protective cover material (solid water and/or plastic). The T60008 and T60016 models also included the high density shielding material. The SFD model was qualitatively validated using mammography images similar to that presented by McKerracher and Thwaites [80]. To reduce boundary crossing, the geometry of the coaxial cable was approximated as a homogeneous mixture of copper and polyethylene.

PEGS4 data were created for the coaxial cable, ABS and several epoxy compounds (See Figure 3.5). Three simulation geometries were created for each detector model correlating to the isocentric measurements made in water, at depths of 1.5, 5.0 and 10.0 cm (See Appendix A.4).

The DOSRZnrc history number was varied and particle recycling number (NRCYL) set automatically to ensure a statistical dose uncertainty scored to the active volume that ranged between ± 0.6% and ± 0.8% for the small fields and less than ± 0.5% for the reference field. The EGSnrc transport parameters ECUT, PCUT and ESTEP were set to 0.521 MeV, 0.01 MeV and 0.25 respectively. The EXACT boundary crossing algorithm was used in combination with the PRESTA-II condensed history electron step algorithm and ESAVEIN = 2.0 MeV. Dose per incident particle was scored using the IFULL = entrance regions. Each simulation was run using the field size specific phase space data for the following source parameter combinations: electron energies at 6.0, 6.1 and 6.2 MeV each with a FWHM = 0.100, 0.110 and 0.120 cm.

3.2.4 Output ratio calculations

The method developed by Popescu *et al* [91] was followed to account for the change in backscatter dose to the monitor chamber as a function of field size. Using this convention ensured the simulated machine output per monitor unit was modelled correctly. For each set of detailed detector simulations the Monte Carlo output ratios were calculated as follows,

$$OR_{det_{MC}}^{f_{clin}} = \left(\frac{D_{det_{MC}}^{f_{clin}}}{D_{det_{MC}}^{f_{msr}}} \right) \cdot \left(\frac{D_{monitor_{MC}}^{f_{msr}}}{D_{monitor_{MC}}^{f_{clin}}} \right), \qquad (3.2)$$

where $D_{det_{MC}}$ and $D_{monitor_{MC}}$ represent the total dose scored to the active volume of the modelled detector and the monitor chamber component module in the BEAM$_B$ simulations respectively. The superscripts *msr* and *clin* follow the Alfonso naming scheme and are used to denote the machine-specific reference field size and the clinical field size of interest. Simulated detector specific output ratios were compared to measurement using a standard percent difference evaluation.

3.2.5 Calculating the detector specific correction factors

Using the convention of Alfonso *et al*, the absorbed dose to water at a reference point in a phantom for a clinical field size, f_{clin}, of beam quality, Q_{clin}, is given by,

$$D_{w,Qclin}^{f_{clin}} = D_{w,Q_{msr}}^{f_{msr}} \cdot \Omega_{Q_{clin},Q_{msr}}^{f_{clin},f_{msr}}. \qquad (3.4)$$

Ω is a field factor that converts absorbed dose to water for the machine-specific reference field to the clinical field of interest. The field factor can be

measured as the ratio of detector readings (Eq. (3.1)) multiplied by a Monte Carlo calculated correction factor (*k*) such that,

$$\Omega_{Q_{clin},Q_{msr}}^{f_{clin},f_{msr}} = OR_{det}^{f_{clin}} \cdot k_{Q_{clin},Q_{msr}}^{f_{clin},f_{msr}}. \qquad (3.5)$$

If we assume the dosimeter readings are directly proportional to the absorbed dose within the active volume of the detector, the Monte Carlo correction factor in Eq. 3.5 will be as follows,

$$k_{Q_{clin},Q_{msr}}^{f_{clin},f_{msr}} = \frac{\left(\frac{D_{w_{MC}}^{f_{clin}}}{D_{w_{MC}}^{f_{msr}}}\right)}{\left(\frac{D_{det_{MC}}^{f_{clin}}}{D_{det_{MC}}^{f_{msr}}}\right)}. \qquad (3.6)$$

The beam quality indices Q_{clin} and Q_{msr} have been removed from the ratio for simplicity but are implied through the use of the f_{clin} and f_{msr} nomenclature. To calculate the correction factor of Eq. (3.6), dose to the active volume of the detector and an all water geometry were simulated. Monte Carlo calculated dose to water, denoted as $D_{w_{MC}}$, was scored using DOSRZnrc and the same active volume boundaries found in each detector model. Simulations were run for each field size using the same phase space data, random number seeds, and EGSnrc input parameters. However, the history number was now set to give a statistical uncertainty less than ± 0.4%.

Each simulation was set to use the photon cross-section enhancement (XCSE = 64) variance reduction technique within a 1.0 cm shell. Reducing the statistical uncertainty for the all water simulation ensured the correction factors calculated using Eq. (3.6) could be reported to within ± 1.0%.

3.3 Results

3.3.1 Small field profiles: measurement and DOSXYZnrc comparison

Shown in Figure 3.6 are the SFD and EBT2 profile data. Although there is a good agreement between most of the data there were some differences as noted by the arrows. These differences are believed to result from inherent non-uniformities in the film but did not alter the overall agreement between the two data sets. Clearly there is excellent agreement between the two data sets both in the beam aperture and outside the geometric field. The work of Sutherland and Rogers [104] suggests that electron disequilibrium resulting from narrow beam configurations does not change the absorbed-dose energy dependence of EBT2 film, therefore the profile agreement between the SFD and EBT2 data not only confirms there is negligible SFD volume averaging (see Sahoo *et al* [96] and Li *et al* [73]) but also establishes there is little detector over-response in the penumbral region of the narrow beam geometry. The profile data is also consistent with that of Sham *et al* [101] and Ding *et al* [38] who showed good agreement between Monte Carlo simulated small field profiles in water and SFD measurement.

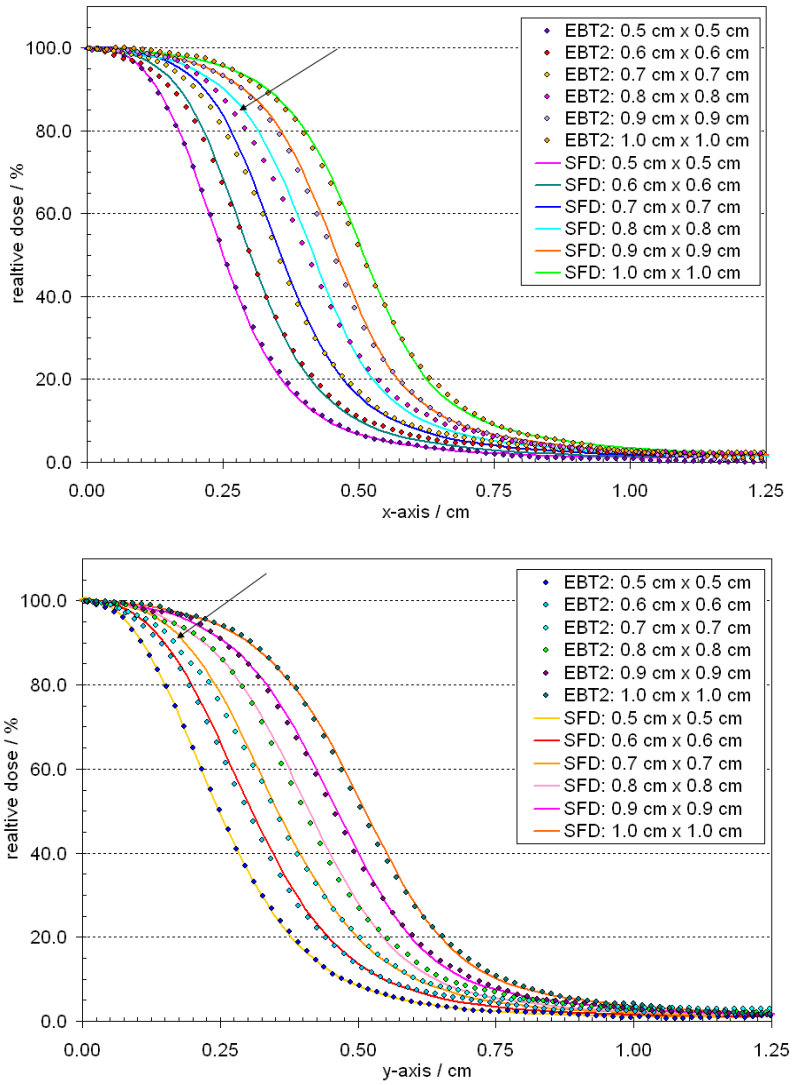

Figure 3.6 Comparison between EBT2 film and SFD profile measurements along the x-axis (top) and y-axis (bottom).

In all cases the measured field sizes were smaller than the nominal by approximately 0.05 cm. This is not necessarily a surprise as the jaw encoders are calibrated in a somewhat subjective procedure that uses jaw positions at -9.0, -4.0, 2.0, 8.0, 14.0 and 19.0 cm.

There were also very small differences found between the measured field widths across each axis, however, the decision was made to model each field as symmetric using the following dimensions: 0.95, 0.85, 0.75, 0.65, 0.55 and 0.45 cm. All subsequent profile and output data used in benchmarking the model were calculated using phase space data for these new field sizes (see Table 3.1).

Table 3.1 Listed here is the nominal, measured and simulated field sizes used for the work presented in this chapter.

Field Size	Profile		Output
Nominal (cm)	Measured (cm)	MC Simulation (cm)	MC Simulation (cm)
1.0 x 1.0	0.932 x 0.930	0.930 x 0.930	0.950 x 0.950
0.9 x 0.9	0.840 x 0.838	0.840 x 0.840	0.850 x 0.850
0.8 x 0.8	0.750 x 0.760	0.750 x 0.760	0.750 x 0.750
0.7 x 0.7	0.646 x 0.650	0.650 x 0.650	0.650 x 0.650
0.6 x 0.6	0.566 x 0.550	0.560 x 0.550	0.550 x 0.550
0.5 x 0.5	0.450 x 0.458	0.450 x 0.460	0.450 x 0.450

Initial simulations with source parameters fixed at 6.1 MeV with a FWHM = 0.150 cm produced penumbral widths much broader than measurement (see Figure 3.7). As the FWHM was decreased from 0.150 to 0.110 cm the fit became progressively better. However, for all but the smallest field size the fit worsened at a FWHM = 0.100 cm. There was very little difference

between profile data for each of the simulated incident electron energies and therefore only the 6.1 MeV case is plotted.

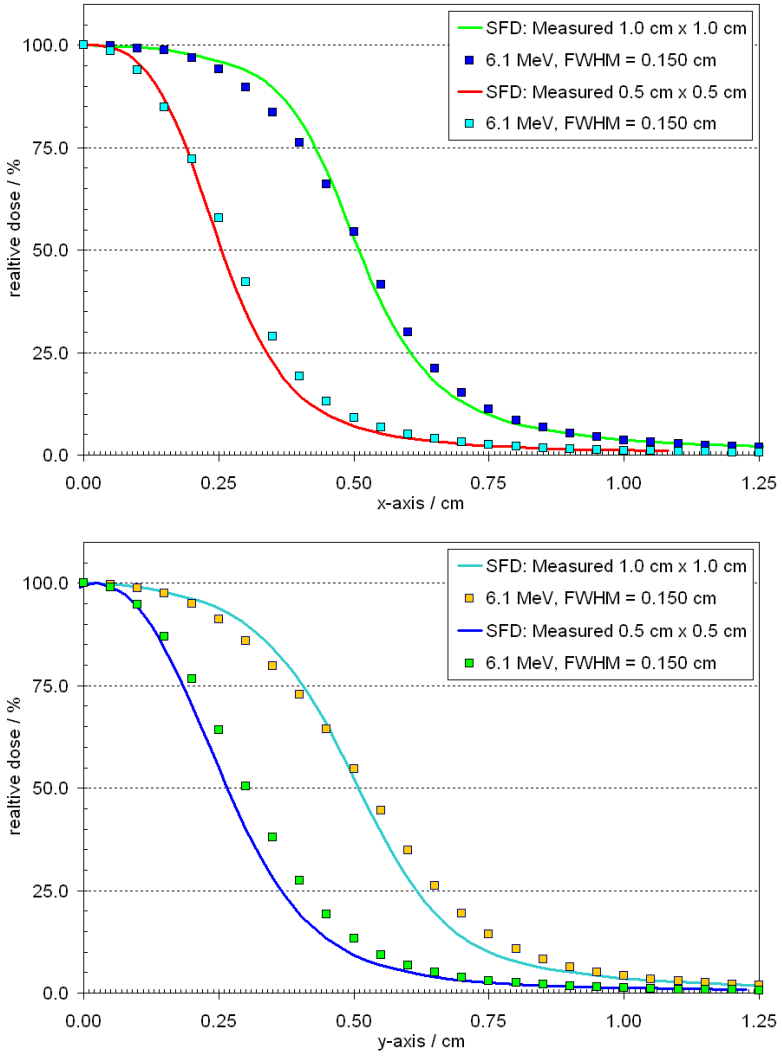

Figure 3.7 SFD measured profile data and DOSXYZnrc simulation data for an incident electron source parameterization of 6.1 MeV and FWHM = 0.150 cm.

Shown in Figure 3.8 is the profile data for a source parameter combination of 6.1 MeV with a FWHM = 0.110 cm. One can see there is generally good agreement between the measured and simulated data. However, it should

be noted there is a small difference in the y-axis data for the smallest field size. This may hint at a limitation of the y-axis jaw model, a difference in the electron FWHM across the two axes or an inadequacy in modelling the spatial distribution of the incident electrons as a Gaussian. That being said, the difference was very small and therefore the circularly symmetric Gaussian was deemed a good representation of the actual distribution and facilitated the use of the azimuthal particle redistribution methodology.

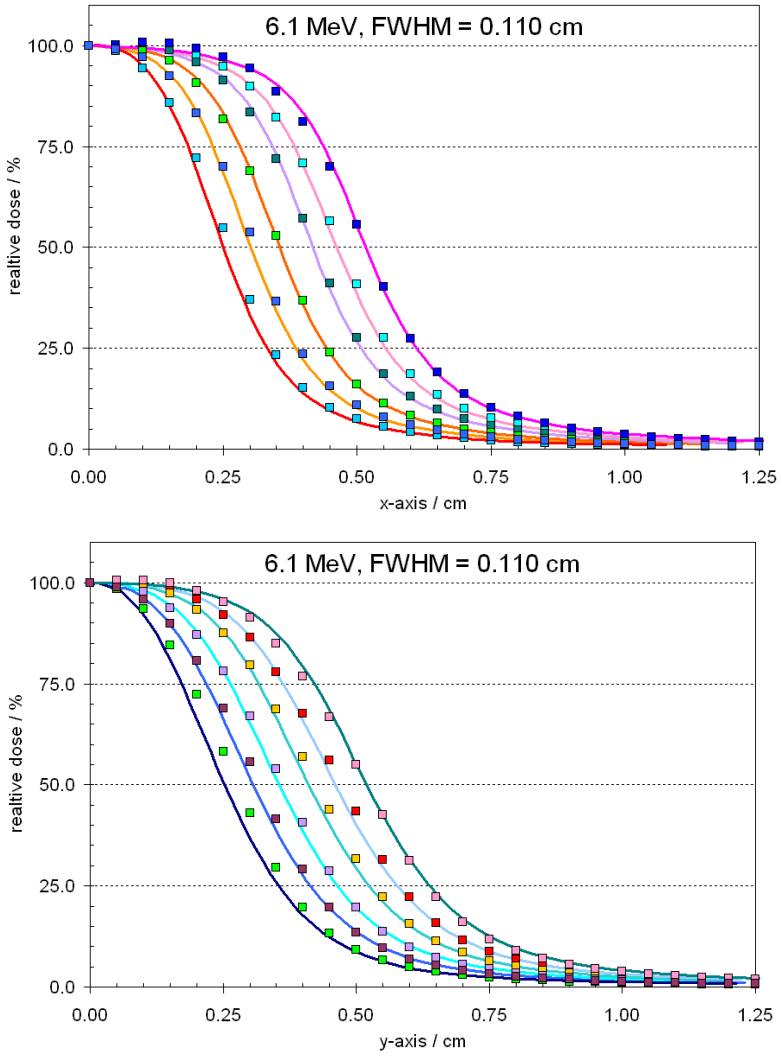

Figure 3.8 Profile comparison between the SFD measurement data (lines) and DOSXYZnrc simulations (squares).

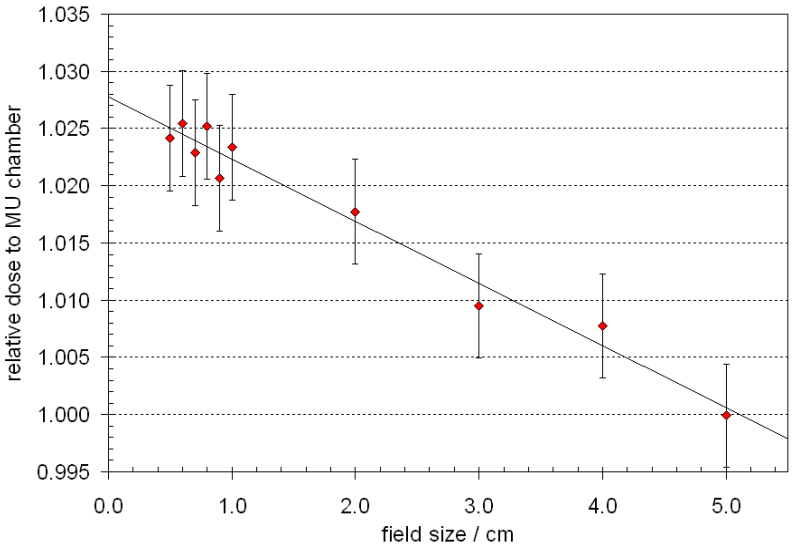

Figure 3.9 The change in backscatter dose to the MU chamber as a ratio with respect to the machine-specific reference field of 5.0 cm x 5.0 cm.

3.3.2 Backscattered dose to the monitor chamber

Figure 3.9 is a plot of the relative backscattered dose to the monitor chamber taken with respect to the machine-specific reference field of 5.0 cm. This data illustrates the importance of including the relative dose to monitor chamber in small field output simulations. As Popescu *et al* note, if one does not account for the difference in monitor chamber backscatter dose an error up to 2.0% may be introduced into simulated output for field sizes between 3.0 cm x 3.0 cm and 30.0 cm x 30.0 cm. It appears from the data shown here that a similar error of up to 2.0% can be introduced into simulated small field output if the dose to the monitor chamber is not correctly accounted for.

3.3.3 Detector specific output ratios: measurement and DOSRZnrc comparison

The percent difference between the SFD measured and simulated output ratios are shown in Figures 3.10, 3.11 and 3.12. The electron energy and FWHM were as follows: 6.0, 6.1 and 6.2 MeV and 0.100, 0.110 and 0.120 cm. The comparison clearly shows that regardless of incident electron energy, a FWHM = 0.100, 0.110 and 0.120 cm produced output ratios that are greater than, equal to, and less than experiment for the smallest field sizes. The best agreement between experiment and simulation was found for the 6.2 MeV electron energy with a FWHM = 0.110 cm. A decision was made to run all further simulations using 6.2 MeV as this energy coincided with the incident electron energy determined during the original TG-105 type commissioning [22].

Plotted in Figures 3.13 thru 3.16 are the percent difference data between measurement and simulation for the remaining detectors (T60008, T60012, T60016 and T60017). One can see the same trend emerging as a function of FWHM. For each detector a FWHM = 0.110 cm resulted in simulated output ratios consistent with experiment. However, it should be noted there was nearly a 2.0% difference in the T60016 and T60017 data at the smallest field size. As noted in Chapter 2, the positional accuracy of the Varian jaw is problematic at field sizes smaller than 0.7 cm and therefore the difference between simulated and experimental output ratios would most likely be due to jaw position rather than detector modelling.

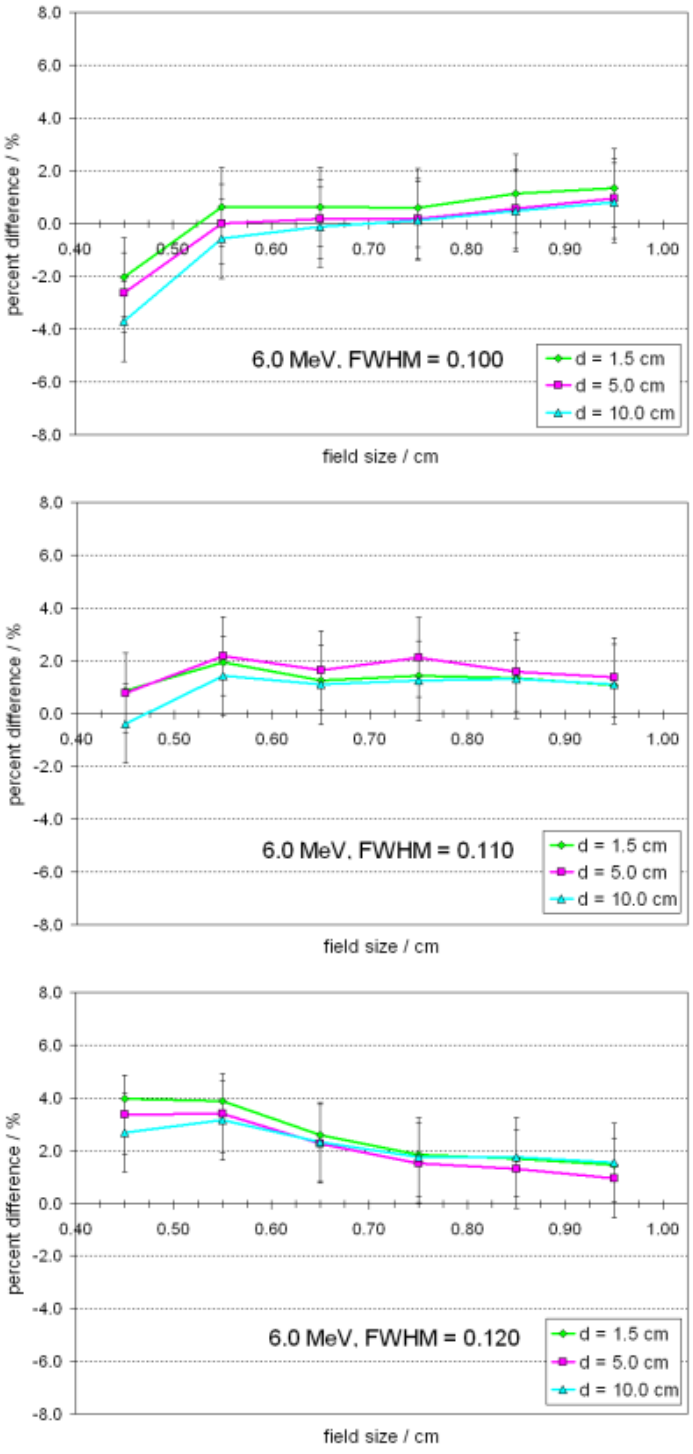

Figure 3.10 The percent difference between the measured and simulated $OR_{det_{MC}}^{f_{clin}}$ for the SFD detector. The electron energy and FWHM were as follows: 6.0 MeV and 0.100, 0.110 and 0.120 cm.

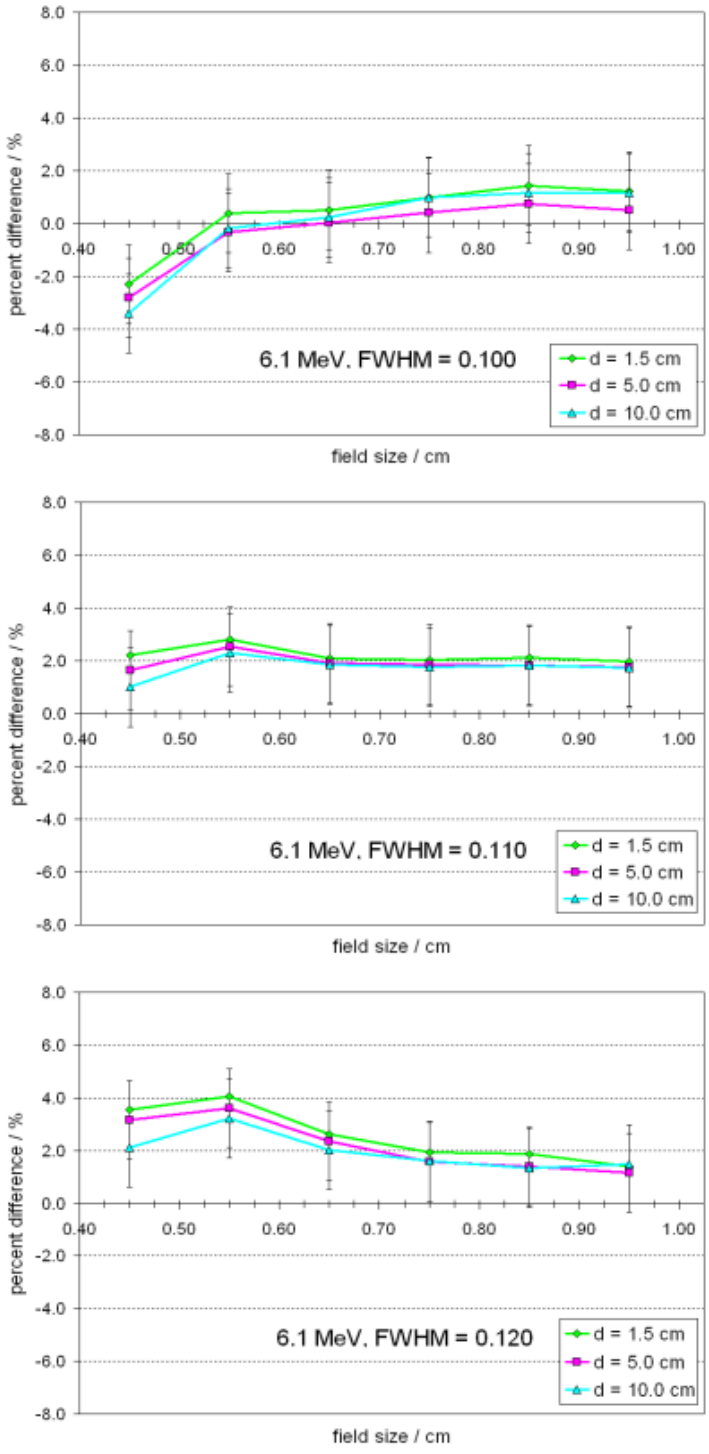

Figure 3.11 The percent difference between the measured and simulated $OR_{det_{MC}}^{f_{clin}}$ for the SFD detector. The electron energy and FWHM were as follows: 6.1 MeV and 0.100, 0.110 and 0.120 cm.

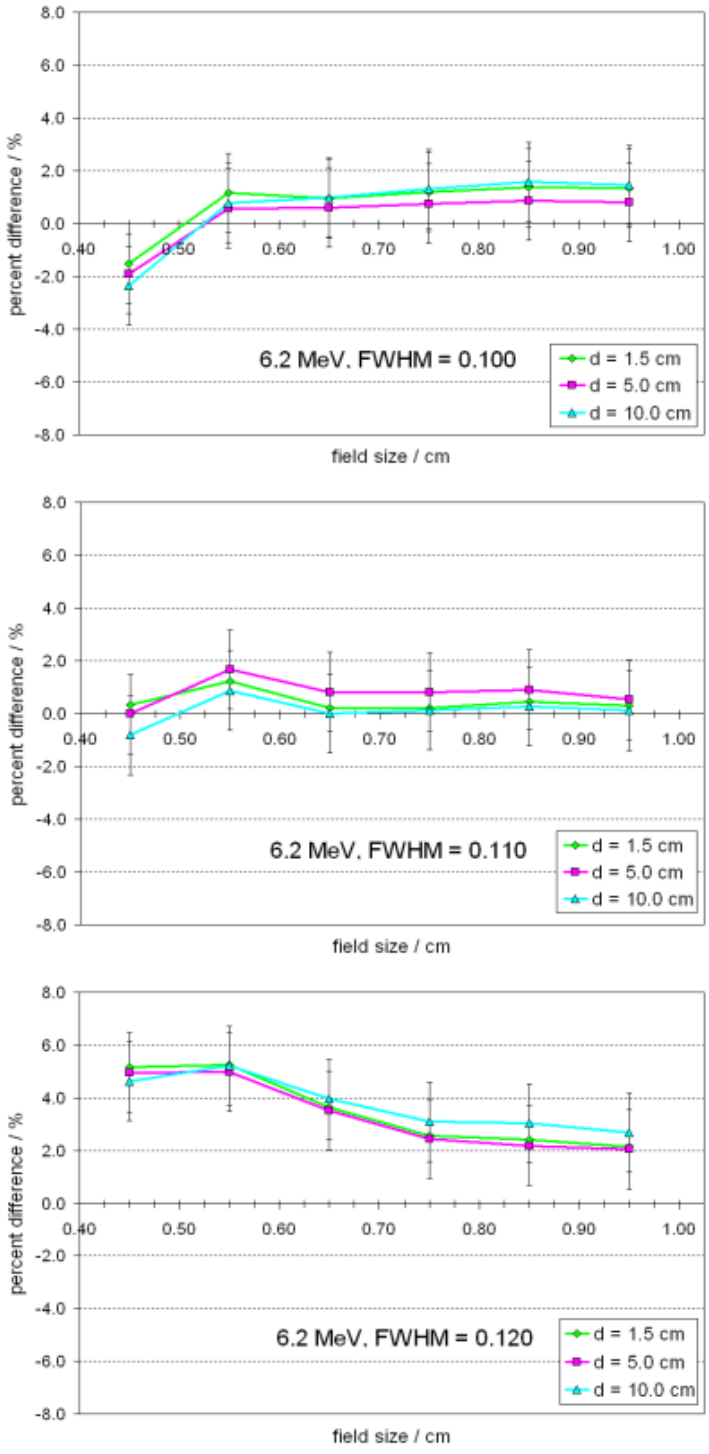

Figure 3.12 The percent difference between the measured and simulated $OR_{det_{MC}}^{f_{clin}}$ for the SFD detector. The electron energy and FWHM were as follows: 6.2 MeV and 0.100, 0.110 and 0.120 cm.

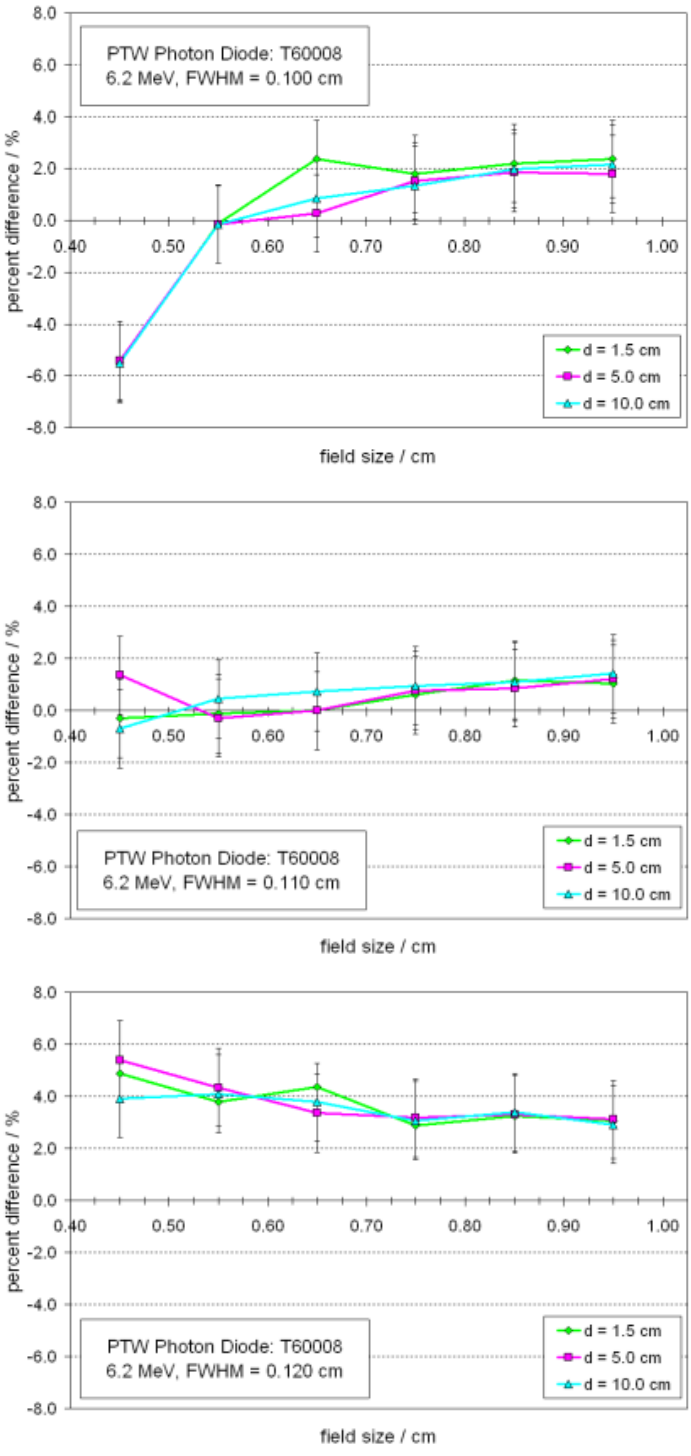

Figure 3.13 The percent difference between the measured and simulated $OR_{det_{MC}}^{f_{clin}}$ for the T60008 detector. The electron energy and FWHM were as follows: 6.2 MeV and 0.100, 0.110 and 0.120 cm..

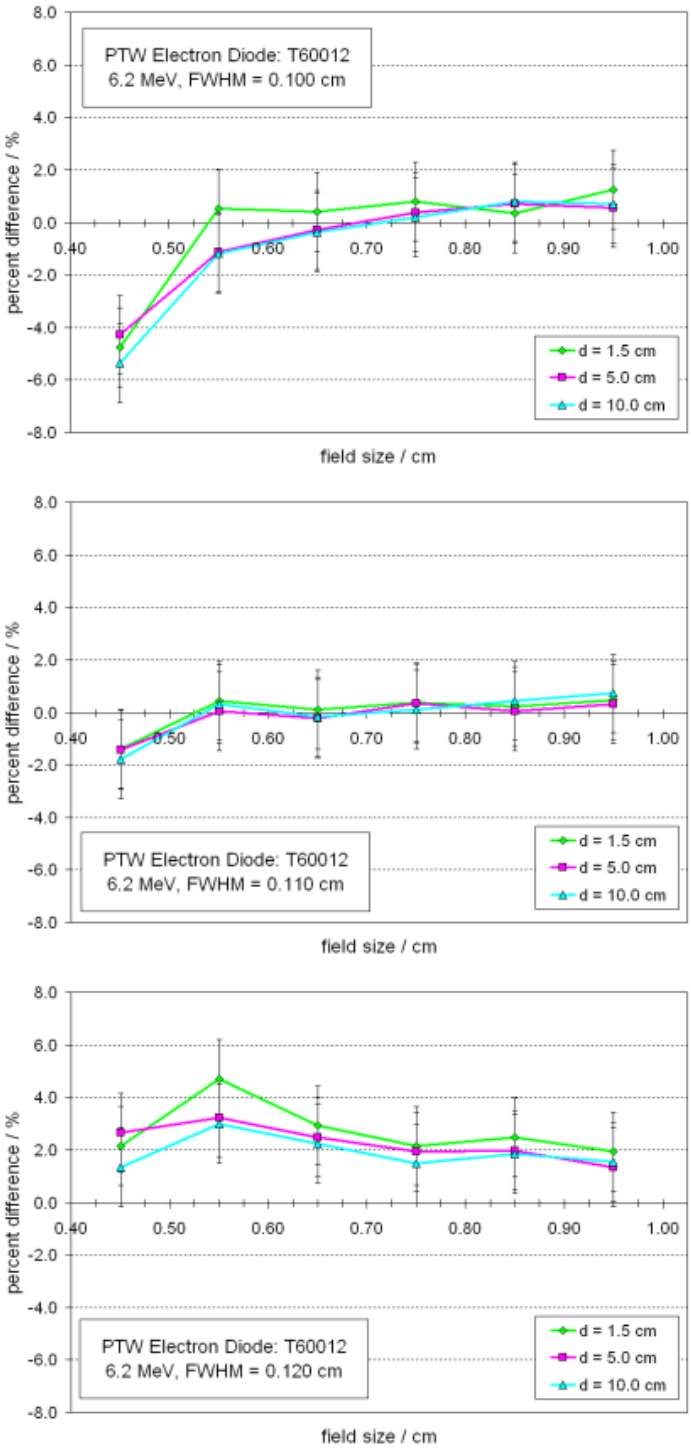

Figure 3.14 The percent difference between the measured and simulated $OR_{det_{MC}}^{f_{clin}}$ for the T60012 detector. The electron energy and FWHM were as follows: 6.2 MeV and 0.100, 0.110 and 0.120 cm.

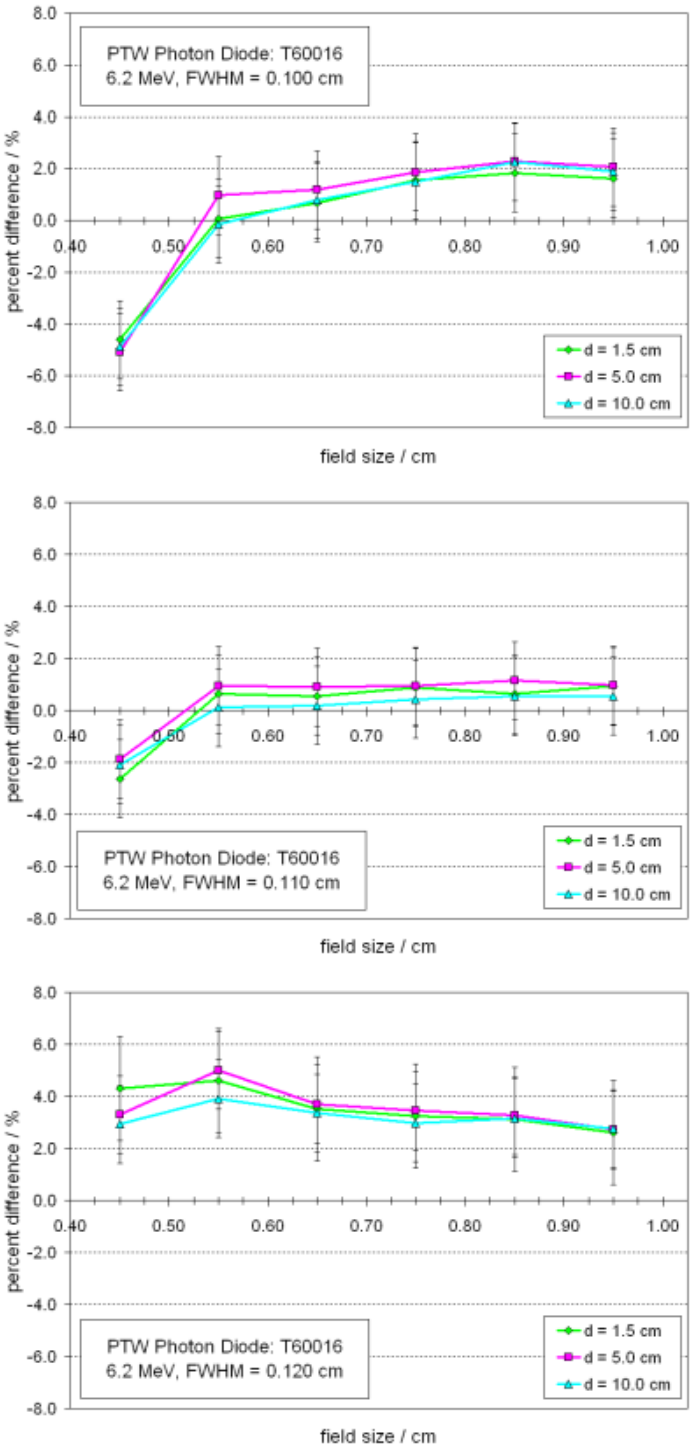

Figure 3.15 The percent difference between the measured and simulated $OR_{det_{MC}}^{f_{clin}}$ for the T60016 detector. The electron energy and FWHM were as follows: 6.2 MeV and 0.100, 0.110 and 0.120 cm.

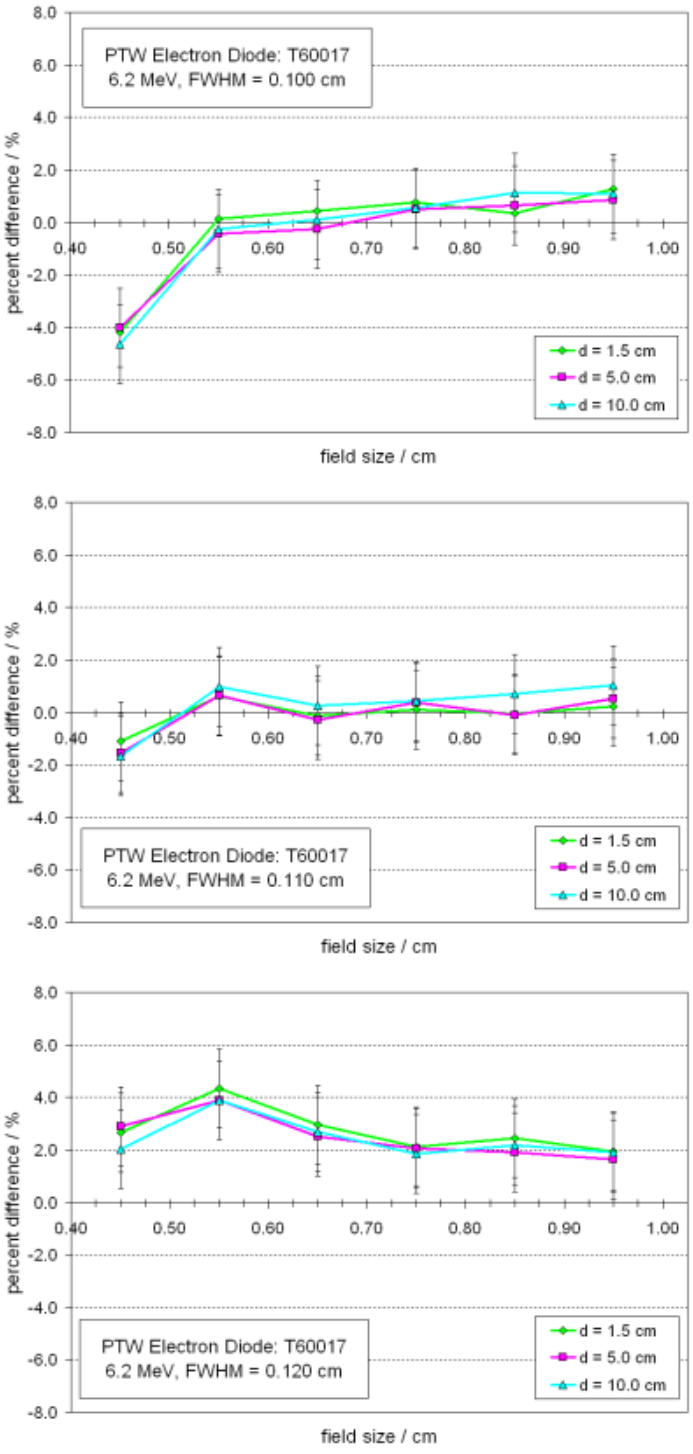

Figure 3.16 The percent difference between the measured and simulated $OR_{det_{MC}}^{f_{clin}}$ for the T60017 detector. The electron energy and FWHM were as follows: 6.2 MeV and 0.100, 0.110 and 0.120 cm.

The simulated $OR_{det_{MC}}^{f_{clin}}$ calculated using a FWHM = 0.100 and 0.120 cm were clearly greater and less than experiment. This sensitivity to changes in FWHM is attributed to the relative source occlusion at the smallest field size. For small fields, fixing the collimator and increasing (decreasing) the source FWHM results in increased (decreased) occlusion. If the simulated source FWHM is increased beyond the actual width, more of the source will be occluded and therefore the simulated output ratios will be less than measurement. In a similar manner, if the source FWHM is decreased beyond the actual width, the simulated output ratio will be greater than measurement. This is what is observed in Figures 3.10 thru 3.16.

3.3.4 Diode detector correction factor analysis

$OR_{det_{MC}}^{f_{clin}}$ were calculated at depths of 1.5, 5.0 and 10.0 cm relative to a square field of side 5.0 cm for simulated field sizes between 0.45 cm and 1.00 cm incremented in steps of 0.05 cm. The all water simulations were also run for each case. The complete data set is shown in Tables 3.2 and 3.3. The associated correction factors, calculated according to Eq (3.6), are presented in Table 3.4. One can see two trends emerge: (1) for each diode the correction factors are the same at all three depths to within the statistical uncertainty and (2) the correction factors required for the shielded diodes are approximately twice that required for the unshielded diodes.

Re-simulations of the T60016 and T60017 diodes at d = 1.5, 5.0 and 10.0 cm for an SSD = 100 cm set-up were run to investigate whether the observed correction factor depth independence was due to using an isocentric set-up. Unlike using an SAD set-up, an SSD set-up will result in a field edge to active volume distance that changes as a function of depth. It was initially expected that using an SSD set-up would result in correction factors that changed as a function of depth, yet this proved not to be the case. Regardless of depth, the simulated output ratios for the SSD set-up were found to be on average 0.010 greater than those calculated for an SAD set-up. Although the output ratios were different, the correction factors were found to be the same within the uncertainties. For the smallest field size the average difference between SAD and SSD correction factors at d = 5.0 and 10.0 were + 0.57% and - 0.85% for the T60016 and T60017 respectively.

The two fold increase in correction factor required for the shielded diodes results, in part, from the significant secondary backscatter off the high density shielding materials located just behind the silicon chip [36]. Plotted in Figure 3.17 is the relative dose to the silicon chip scored through the back surface: all water, T60016 and T60017 diodes. The contribution through the back surface of the shielded diode was found to be constant at 18%. This differs significantly from the 6% to 8% contribution found for the unshielded diode and water only simulations.

Table 3.2 Simulated and measured relative output for water and shielded diodes at depths of 1.5, 5.0 and 10.0 cm.

Relative Output		5.0 cm	3.0 cm	1.0 cm	0.95 cm	0.90 cm	0.85 cm	0.80 cm	0.75 cm	0.70 cm	0.65 cm	0.60 cm	0.55 cm	0.50 cm	0.45 cm
Water	**1.5 cm**	1.000	0.964	0.850	0.838	0.827	0.814	0.794	0.784	0.761	0.738	0.710	0.676	0.638	0.588
	5.0 cm	1.000	0.946	0.801	0.783	0.774	0.760	0.745	0.727	0.708	0.686	0.657	0.625	0.587	0.539
	10.0 cm	1.000	0.931	0.772	0.753	0.744	0.729	0.714	0.696	0.677	0.654	0.626	0.593	0.558	0.512
PTW T60008 (measured)	**1.5 cm**	1.000	0.971 (0.964)	0.886	0.876 (0.884)	0.869	0.855 (0.865)	0.847	0.833 (0.839)	0.818	0.801 (0.801)	0.772	0.739 (0.741)	0.710	0.657 (0.636)
	5.0 cm	1.000	0.949 (0.947)	0.835	0.824 (0.834)	0.817	0.807 (0.814)	0.794	0.781 (0.787)	0.764	0.746 (0.746)	0.720	0.692 (0.688)	0.659	0.599 (0.590)
	10.0 cm	1.000	0.935 (0.930)	0.806	0.792 (0.803)	0.785	0.775 (0.783)	0.762	0.748 (0.755)	0.732	0.713 (0.717)	0.689	0.655 (0.657)	0.627	0.569 (0.563)
PTW T60016 (measured)	**1.5 cm**	1.000	0.968 (0.966)	0.889	0.879 (0.889)	0.873	0.864 (0.870)	0.852	0.838 (0.845)	0.821	0.799 (0.804)	0.771	0.735 (0.740)	0.697	0.648 (0.632)
	5.0 cm	1.000	0.948 (0.948)	0.840	0.829 (0.839)	0.824	0.810 (0.819)	0.801	0.786 (0.794)	0.763	0.745 (0.752)	0.717	0.685 (0.692)	0.649	0.592 (0.581)
	10.0 cm	1.000	0.930 (0.930)	0.810	0.800 (0.806)	0.791	0.782 (0.786)	0.768	0.754 (0.758)	0.735	0.715 (0.716)	0.683	0.651 (0.652)	0.615	0.564 (0.552)

Table 3.3 Simulated and measured relative output for unshielded diodes at depths of 1.5, 5.0 and 10.0 cm.

Relative Output		5.0 cm	3.0 cm	1.0 cm	0.95 cm	0.90 cm	0.85 cm	0.80 cm	0.75 cm	0.70 cm	0.65 cm	0.60 cm	0.55 cm	0.50 cm	0.45 cm
PTW T60012 (measured)	**1.5 cm**	1.000	0.960 (0.961)	0.868	0.855 (0.860)	0.849	0.838 (0.840)	0.823	0.808 (0.811)	0.792	0.771 (0.771)	0.746	0.713 (0.716)	0.678	0.620 (0.612)
	5.0 cm	1.000	0.943 (0.942)	0.816	0.802 (0.806)	0.794	0.784 (0.784)	0.769	0.753 (0.755)	0.735	0.717 (0.715)	0.690	0.654 (0.655)	0.625	0.577 (0.569)
	10.0 cm	1.000	0.920 (0.923)	0.779	0.766 (0.773)	0.757	0.745 (0.749)	0.731	0.716 (0.717)	0.699	0.679 (0.678)	0.653	0.616 (0.618)	0.589	0.539 (0.530)
PTW T60017 (measured)	**1.5 cm**	1.000	0.962 (0.956)	0.869	0.857 (0.860)	0.850	0.840 (0.840)	0.824	0.810 (0.810)	0.793	0.773 (0.772)	0.747	0.709 (0.714)	0.679	0.621 (0.615)
	5.0 cm	1.000	0.944 (0.943)	0.816	0.803 (0.809)	0.795	0.785 (0.784)	0.770	0.754 (0.756)	0.736	0.717 (0.715)	0.691	0.655 (0.659)	0.625	0.578 (0.570)
	10.0 cm	1.000	0.921 (0.925)	0.779	0.767 (0.776)	0.757	0.746 (0.751)	0.731	0.717 (0.720)	0.699	0.679 (0.681)	0.653	0.617 (0.624)	0.599	0.541 (0.533)
SFD (measured)	**1.5 cm**	1.000	0.960 (0.958)	0.857	0.844 (0.848)	0.835	0.824 (0.826)	0.808	0.793 (0.798)	0.776	0.756 (0.761)	0.730	0.698 (0.705)	0.662	0.614 (0.618)
	5.0 cm	1.000	0.946 (0.937)	0.805	0.792 (0.791)	0.781	0.771 (0.770)	0.755	0.739 (0.742)	0.722	0.701 (0.704)	0.675	0.646 (0.648)	0.611	0.565 (0.566)
	10.0 cm	1.000	0.926 (0.921)	0.768	0.757 (0.761)	0.747	0.734 (0.738)	0.719	0.704 (0.709)	0.686	0.666 (0.670)	0.639	0.610 (0.613)	0.577	0.532 (0.531)

Table 3.4 Correction factors calculated using the all water and detector specific simulation data presented in Tables 3.2 and 3.3.

Correction Factor		5.0 cm	3.0 cm	1.0 cm	0.95 cm	0.90 cm	0.85 cm	0.80 cm	0.75 cm	0.70 cm	0.65 cm	0.60 cm	0.55 cm	0.50 cm	0.45 cm
PTW T60008	**1.5 cm**	1.000	0.993	0.959	0.956	0.951	0.952	0.938	0.941	0.930	0.922	0.920	0.915	0.899	0.895
	5.0 cm	1.000	0.998	0.959	0.950	0.947	0.942	0.938	0.931	0.926	0.919	0.913	0.904	0.892	0.901
	10.0 cm	1.000	0.995	0.959	0.950	0.948	0.940	0.938	0.931	0.924	0.917	0.909	0.905	0.889	0.900
PTW T60012	**1.5 cm**	1.000	1.004	0.980	0.979	0.975	0.971	0.965	0.971	0.961	0.957	0.952	0.949	0.941	0.948
	5.0 cm	1.000	1.003	0.983	0.976	0.975	0.970	0.968	0.965	0.963	0.957	0.952	0.956	0.940	0.944
	10.0 cm	1.000	1.006	0.989	0.983	0.983	0.978	0.977	0.972	0.968	0.963	0.959	0.963	0.948	0.949
PTW T60016	**1.5 cm**	1.000	0.996	0.956	0.953	0.948	0.942	0.933	0.936	0.926	0.924	0.921	0.920	0.916	0.906
	5.0 cm	1.000	0.998	0.954	0.944	0.940	0.939	0.929	0.924	0.928	0.921	0.917	0.913	0.906	0.907
	10.0 cm	1.000	1.000	0.953	0.941	0.940	0.932	0.930	0.923	0.921	0.915	0.916	0.911	0.907	0.908
PTW T60017	**1.5 cm**	1.000	1.002	0.978	0.978	0.973	0.969	0.964	0.969	0.960	0.955	0.951	0.954	0.939	0.947
	5.0 cm	1.000	1.002	0.982	0.975	0.974	0.969	0.967	0.964	0.962	0.956	0.951	0.955	0.939	0.933
	10.0 cm	1.000	1.001	0.991	0.982	0.982	0.978	0.977	0.972	0.968	0.963	0.959	0.960	0.947	0.945
SFD	**1.5 cm**	1.000	1.005	0.992	0.992	0.991	0.988	0.983	0.989	0.981	0.977	0.974	0.969	0.964	0.957
	5.0 cm	1.000	1.001	0.996	0.989	0.991	0.986	0.987	0.984	0.980	0.978	0.973	0.969	0.961	0.955
	10.0 cm	1.000	1.005	1.001	0.995	0.997	0.993	0.993	0.990	0.986	0.983	0.980	0.972	0.966	0.961

3.4 Discussion

In reviewing the literature on Monte Carlo small field dosimetry it becomes apparent that a TG-105 type approach to commissioning a Monte Carlo linac model may be insufficient. As demonstrated in this work, the preferred approach would be to further fine tune the incident electron source parameters by performing an additional consistency check between measured and simulated small field profiles and detector specific output ratios. Measuring and simulating output ratios at multiple depths further refines the methodology and maximizes the chance of an optimized incident electron energy being selected. Clearly this type of approach to accelerator head model commissioning complements the large field methodology and may eliminate the introduction of systematic errors associated with incorrect source parameterization.

To make any assertions regarding source parameters one must first ensure the detector geometry is correctly modelled. Unlike the work of Scott *et al* [98,99], where small field total scatter factors were derived using only a chip in water model, the data presented here has been calculated for a comprehensive set of geometrically correct diode detector models. Validating the combined linac-detector models against experiment is robust, in-line with the multi-detector approach taken by Francescon *et al* [41] and consistent with the TG-105 philosophy.

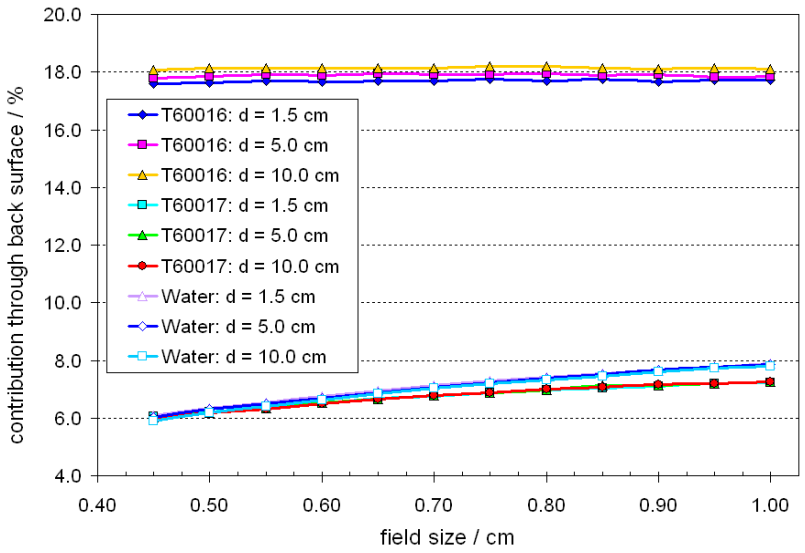

Figure 3.17 The percent contribution of the total dose scored to the active volume received through the back surface of the silicon chip and the equivalent volume of the all water geometry.

The corrections required for the unshielded diodes investigated show that measured output ratios, relative to a 5.0 cm x 5.0 cm field, are consistently greater than the in-water output factors. This is further pronounced for the shielded diodes, where scattered photons and electrons from the shielding material result in an increased dose to the sensitive volume, thereby contributing a larger fraction of the total signal as a function of field size decrease.

Eklund and Ahnesjö [42] present small field data which appears to contradict the results presented here and the work of Haryanto *et al* [50], Araki *et al* [4], Francescon *et al* [44,45], Scott *et al* [98,99], Griessbach *et al* [48], and most recently Pantelis *et al* [88]. The Monte Carlo results shown by Eklund and Ahnesjö [42] predict a decrease in unshielded diode detector response at

the smallest field sizes. Unfortunately, the authors do not model the complete detector geometry nor do they validate the combined linac-detector model with respect to experimental measurement. In fact, they only show measured data for square field sizes of side 3.0 to 20.0 cm. This is regrettable as the thrust of their paper was modelling diode response factors for small fields.

In addition to correctly modelling the detector geometry one must also properly simulate backscattered dose to the monitor chamber. However, none of the fore mentioned authors include backscattered dose to the monitor chamber into the simulated relative output calculations. Francescon *et al* [41] does note the effect on the Cyberknife model was initially tested and found to be less than 0.5%. They speculate the effect is lower than in conventional linear accelerators due to the unique geometry of the collimating system, the smaller volume of the monitor chamber and the smaller reference field size. To date, backscattered dose to the monitor chamber for small field simulations for a Varian iX linac have not been reported. Ding [37] reports a 2.5% variation in the backscattered dose to the monitor chamber for field sizes varying from 4.0 cm x 4.0 cm to 40.0 cm x 40.0 cm. The data shown here reveals the change in dose scored to the MU chamber for small fields to be consistent with that reported in the literature for large fields.

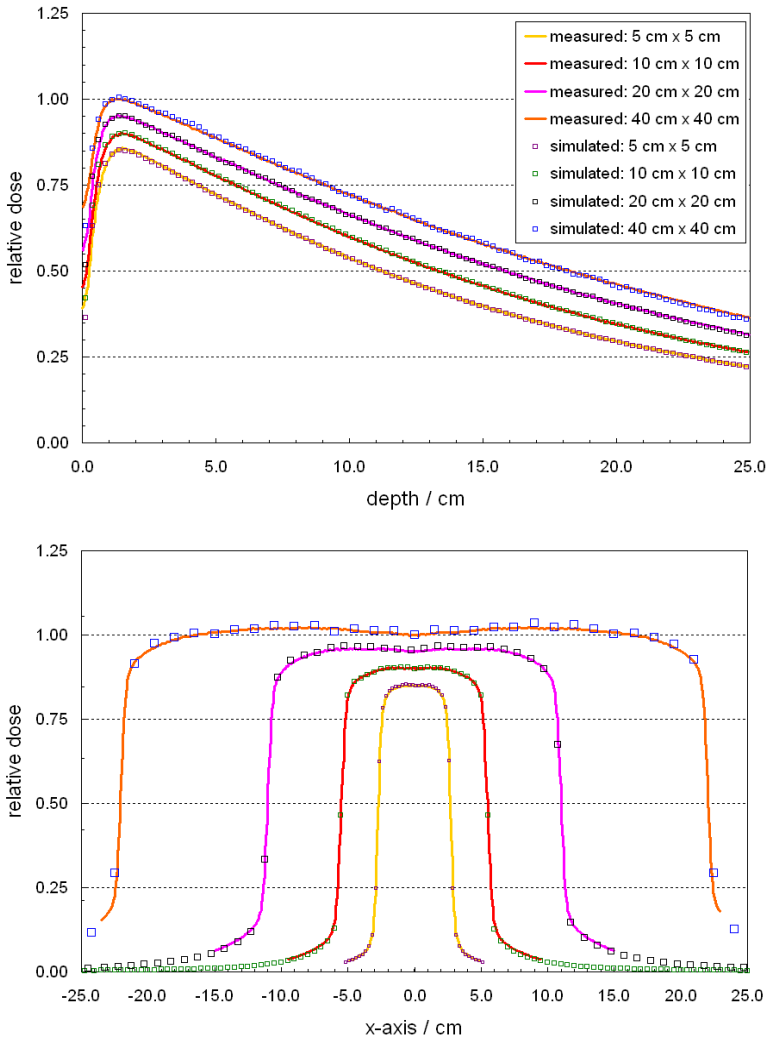

Figure 3.14 The percentage depth dose and profile data for 5, 10, 20 and 40 cm square fields measured using a CC04 ionization chamber (IBA/Scanditronix). The normalization factors applied to each field size are arbitrary and used for display purposes only.

Percent depth dose (pdd) and profile data for simulated 5.0 cm x 5.0 cm, 10.0 cm x 10.0 cm, 20.0 cm x 20.0 cm and 40.0 cm x 40.0 cm field geometries are shown in Figure 3.14. The data is presented with respect to measurements made using a CC04 ionization chamber (IBA/Scanditronix) and demonstrates a more general validation of the head model. The

experimental relative output factors, with respect to a 10.0 cm x 10.0 cm, were 0.893, 1.000, 1.101 and 1.196 respectively. Monte Carlo all water simulated relative output, presented in the same order, were 0.899, 1.000, 1.092 and 1.152. Clearly there is good agreement with exception of the 40.0 cm x 40.0 cm Monte Carlo data, which was found to be 3.7% lower than measurement. As Chetty *et al* [22] note, output ratios are significantly influenced by the increase in head scattered radiation common for large fields. The increase in head scatter results from extra-focal sources arising from the flattening filter and/or primary collimator. As the field size is increased the extra-focal sources are often completely exposed. The difference in output factor noted above may well result from the actual geometry of the primary collimator being slightly different from that presented in the detailed drawings supplied from the vendor. Although this is worth investigating it would not change the results of this small field study.

It becomes clear that if the correction factor convention proposed by Alfonso *et al* is to be implemented into standard clinical practice, a protocol-like approach to Monte Carlo small field beam commissioning and detector modelling may be beneficial to the community. However, given the comprehensive data set presented here a clinical user may not need to work through the entire linac-detector modelling process [39]. It is expected that the detector specific correction factors presented in Table 3.4 can be applied to experimental small field output ratios consistent with those reported in Tables 3.2 and 3.3. Although there has been no prescribed methodology proposed in the literature yet, this would include relative output ratio

measurements having been made in a treatment beam with the same beam quality ($TPR_{20,10}$ = 0.673) [87]. In addition, the correction factors presented in Table 3.4 should only be applied for the same measured field sizes and not the nominal.

Essentially, a clinical user would have to repeat the measurement portion of this work, evaluate the consistency between the two data sets and then apply the correction factors. Having such a comprehensive set of detector specific small field correction factors available should make the conversion process from measured output ratios to in-water output factors simple and consistent.

3.4 Conclusions

A number of general conclusions come out of working through the proposed small field dosimetry formalism: (1) Monte Carlo calculated small field, detector specific, output ratios and in-water output factors are very sensitive to the simulated source parameterization and therefore rigorous linac model commissioning must be pursued prior to use, (2) backscattered dose to the monitor chamber should be included in simulated output ratio calculations, (3) the corrections required for diode detectors are design dependent and therefore detailed detector modelling is required and (4) the reported detector specific correction factors may be applied to experimental small field $OR_{det}^{f_{clin}}$ data which is consistent with that of the simulations.

Chapter 4
Diode detector model simplification for Monte Carlo small field photon dosimetry and correction factor sensitivity to source parameterization

4.1 Introduction

The importance of systematic experimental validation of accelerator and detector models used in Monte Carlo simulations was demonstrated in Chapter 3. A thorough implementation of a proposed Monte Carlo based small field dosimetry formalism was also presented and for the smallest field sizes investigated $k_{Q_{clin},Q_{msr}}^{f_{clin},f_{msr}}$ for shielded and unshielded diodes were found to be 0.90 and 0.95 respectively. Francescon *et al* [45] has present similar $k_{Q_{clin},Q_{msr}}^{f_{clin},f_{msr}}$ values for the PTW T60012 unshielded diode for the Elekta Synergy® and Siemens Primus linac head designs at a nominal 6 MV beam energy. The authors further investigate the sensitivity of $k_{Q_{clin},Q_{msr}}^{f_{clin},f_{msr}}$ to changes in source parameterization on both the Elekta and Siemens head designs and find that $k_{Q_{clin},Q_{msr}}^{f_{clin},f_{msr}}$ can be considered dependent only on field size.

In an earlier work, Scott *et al* [98] used a simple DOSXYZnrc model of the electron field diode (EFD) and explored various aspects of small field dosimetry at 15 MV. The impact of simulated focal spot size, the resulting source occlusion and subsequent change in small field relative output were

all investigated. The authors conclude that one should fine tune the modelled electron spot size using both profile data and small field output factors [99], yet do not rigorously validate the application of the simplified detector model. The authors do however present ($D_{w_{MC}}^{f_{clin}} / D_{Si_{MC}}^{f_{clin}}$) data for square field sizes ranging from 0.5 cm to 10.0 cm, which when recast as a normalized response factor, ($D_{Si_{MC}}^{f_{clin}} / D_{w_{MC}}^{f_{clin}}$)/($D_{Si_{MC}}^{f_{10x10}} / D_{w_{MC}}^{f_{10x10}}$), reveal a 3.5% silicon-to-water over-response at the 0.5 cm field size. This can be considered modest validation for using the simplified detector model, as the over-response is consistent with that predicted by detailed detector modelling. However, the results do contradict the normalized response data for a simplified unshielded diode detector model as presented by Eklund and Ahnesjö [42].

The goal of this portion of the work was to investigate whether simplified diode detector models can be used within the proposed small field dosimetry formalism. In addition, the influence of active volume dimension on output ratio and response factor was investigated, as was the influence of source parameterization on $k_{Q_{clin},Q_{msr}}^{f_{clin},f_{msr}}$ for the Varian iX linac head design.

4.2 Methods

A BEAMnrc [93] model of a nominal 6 MV Varian iX linear accelerator head, of beam quality $TPR_{20,10}$ = 0.673, was used throughout this portion of the

study. The baseline electron source parameterization was as follows: 6.2 MeV mono-energetic with a circularly symmetric Gaussian FWHM = 0.110 cm. The convention of Popescu *et al* [91] was followed in defining the accelerator head model into parts A and B. The $BEAM_A$ portion of the model included the target, primary collimator, flattening filter and MU chamber – this eliminated re-simulating the circularly symmetric components of the linac head. Phase space ($PHSP_A$) data was scored below the MU chamber and used as the source for field size specific $BEAM_B$ simulations. The $BEAM_B$ model consisted of the MU chamber, mirror and collimator jaws. Azimuthal particle redistribution [14] was used in the $BEAM_B$ simulations to reduce the latent $PHSP_B$ uncertainty. The method developed by Popescu *et al* was used to ensure simulated machine output per monitor unit was correctly modelled and gave results that were in agreement with the experimental measurement.

4.2.1 Detector geometry and model simplification

The stereotactic field diode, T60016 shielded and T60017 unshielded diodes were selected for this study as they each have an active area quoted by the manufactures at ≤ 1.0 mm^2. The full detector geometries were modelled in DOSRZnrc [95] and included the stainless steel stem, coaxial cable, housing and enclosure materials and high density shielding. The T60016 shielded diode has a metal shield placed around the silicon chip to compensate for the silicon over-response to low-energy photons. For the T60017 unshielded diode, the metal shield is replaced with epoxy and

therefore the excessive backscatter of electrons from the shield into the active volume is eliminated. However, the T60017 does have a thin, high density, filter plate located upstream of the chip itself. Each active volume was modelled as a 0.240 mm thick disk of pure silicon at the front face of a larger disk of overall thickness equal to 0.500, 0.525 and 0.400 mm for the SFD, T60016 and T60017 respectively. The active volume radius was 0.300 mm within a chip radius of 0.500 mm for the SFD and 0.564 mm within a chip radius of 0.750 mm for both the T60016 and T60017. To reduce boundary crossing, the geometry of the coaxial cable was approximated as a homogeneous mixture of copper and polyethylene. PEGS4 data were created for the coaxial cable, ABS and several epoxy compounds.

The methodology used to investigate the accuracy of simplified detector models was to start with the all water geometry and add components until the percent difference in $OR_{det_{MC}}^{f_{clin}}$ between each of the simplified and complete detector models was less than 1.0%. The first component added to each of the simplified detector models was the silicon chip, which is equivalent to the approximation employed by Scott *et al* [98,99] and Eklund and Ahnesjö [42]. The next detector components added were any high density regions in and around the silicon chip. The simulated output ratio was calculated for each detector geometry (simplified or not) as follows,

$$OR_{det_{MC}}^{f_{clin}} = \left(\frac{D_{det_{MC}}^{f_{clin}}}{D_{det_{MC}}^{f_{msr}}} \right) \cdot \left(\frac{D_{monitor_{MC}}^{f_{msr}}}{D_{monitor_{MC}}^{f_{clin}}} \right). \qquad (4.1)$$

$D_{det_{MC}}^{f_{clin}}$, $D_{det_{MC}}^{f_{msr}}$, $D_{monitor_{MC}}^{f_{clin}}$ and $D_{monitor_{MC}}^{f_{msr}}$ represent the dose per incident particle scored to the active volume of the detector model and linac monitor unit chamber for the f_{clin} and f_{msr} simulations respectively. Incorporating ($D_{monitor_{MC}}^{f_{msr}} / D_{monitor_{MC}}^{f_{clin}}$) into the output ratio calculation correctly accounts for the change in backscatter dose to the monitor chamber as a function of field size, which has been shown to be 2.5% greater for a square field size of side 0.5 cm with respect to a square field size of side 5.0 cm.

All simulations were run such that the statistical dose uncertainty scored to the active volume was approximately ±0.5%. The EGSnrc transport parameters ECUT, PCUT and ESTEP were set to 0.521 MeV, 0.01 MeV and 0.25 respectively. The EXACT boundary crossing algorithm was used in combination with the PRESTA-II condensed history electron step algorithm, ESAVEIN = 2.0 MeV and the photon cross-section enhancement (XCSE = 64) variance reduction technique within a 1.0 cm shell. Each simulation was run using $PHSP_B$ data for jaw collimated field sizes of side 0.5, 0.6, 0.7, 0.8, 0.9, 1.0 and 3.0 cm with a jaw collimated 5.0 cm x 5.0 cm field used as the f_{msr}. The active volume of each detector model was located at isocenter for depths in water of 1.5, 5.0 and 10.0 cm.

4.2.2 The influence of active volume dimension on response factor

The all water geometry and the simplified silicon chip in water model were used to investigate the change in output ratio, and normalized response factor, as a function of active volume size. $OR_{w_{MC}}^{f_{clin}}$ and $OR_{Si_{MC}}^{f_{clin}}$ represent the Monte Carlo calculated output ratios for the all water and simplified silicon chip in water models respectively. The active volume size perpendicular to the central beam axis was varied in the DOSRZnrc models using the following radii: R = 0.125 mm to 0.750 mm in increments of 0.125 mm and from 0.75 mm to 2.50 mm in increments of 0.25 mm.

In each case the active volume dimension was the same for the all water and chip in water simulations. $OR_{w_{MC}}^{f_{clin}}$ and $OR_{Si_{MC}}^{f_{clin}}$ were calculated for a square f_{clin} of side 0.5 cm with respect to a square f_{msr} of side 5.0 cm at d = 5.0 cm only. The simulations were run using an incident electron energy of 6.2 MeV and a FWHM = 0.110 with the history number set automatically to give a statistical uncertainty of less than ± 0.5% on the dose scored to the active volume per incident particle.

The normalized response factor, as used by Eklund and Ahnesjö [42] and Francescon *et al* [45], is calculated such that,

$$RF = \frac{\left(\frac{D_{Si_{MC}}^{f_{clin}}}{D_{w_{MC}}^{f_{clin}}} \right)}{\left(\frac{D_{Si_{MC}}^{f_{msr}}}{D_{w_{MC}}^{f_{msr}}} \right)}, \qquad (4.2)$$

and is simply the inverse of $k_{Q_{clin},Q_{msr}}^{f_{clin},f_{msr}}$ as defined by Alfonso *et al* [1]. Two sets of response factor data were calculated using the same set of active volume sizes described above for a square field of side 0.5 with respect to the square field of side 5.0 cm. The first data set was calculated using equivalent active volumes for $D_{Si_{MC}}^{f_{clin}}$, $D_{Si_{MC}}^{f_{msr}}$, $D_{w_{MC}}^{f_{clin}}$ and $D_{w_{MC}}^{f_{msr}}$. The second data set was calculated using $D_{w_{MC}}^{f_{clin}}$ and $D_{w_{MC}}^{f_{msr}}$ values for the 0.125 mm volume only. Calculating the response factor in this manner relates the dose scored to the various simulated silicon chip sizes to dose scored to a point like small volume of water.

4.2.3 Sensitivity of $k_{Q_{clin},Q_{msr}}^{f_{clin},f_{msr}}$ to source parameterization

The sensitivity of $k_{Q_{clin},Q_{msr}}^{f_{clin},f_{msr}}$ to variations in electron energy and FWHM were investigated using each of the simplified detector models and a water only geometry with an equivalently small scoring volume. The first set of $k_{Q_{clin},Q_{msr}}^{f_{clin},f_{msr}}$ data was calculated for an electron energy fixed at 6.2 MeV with the Gaussian spatial distribution varied as follows: FWHM = 0.100, 0.110, 0.120, 0.130, 0.140 and 0.150 cm. This range of values was chosen as a reasonable representation of actual FWHM values and is consistent with that reported in the literature [101]. The second set of data was for electron energies at 5.5, 5.8, 6.0, 6.2 and 6.5 MeV with the spatial distribution fixed at a FWHM = 0.110 cm. These energies encompass the upper [23] and lower [102] modelling limits as reported in the literature. All simulations were run as described in the previous section at d = 5.0 cm only and used the same

initial random number seeds to maximize the correlation in $k^{f_{clin},f_{msr}}_{Q_{clin},Q_{msr}}$ calculated for the various source parameterizations.

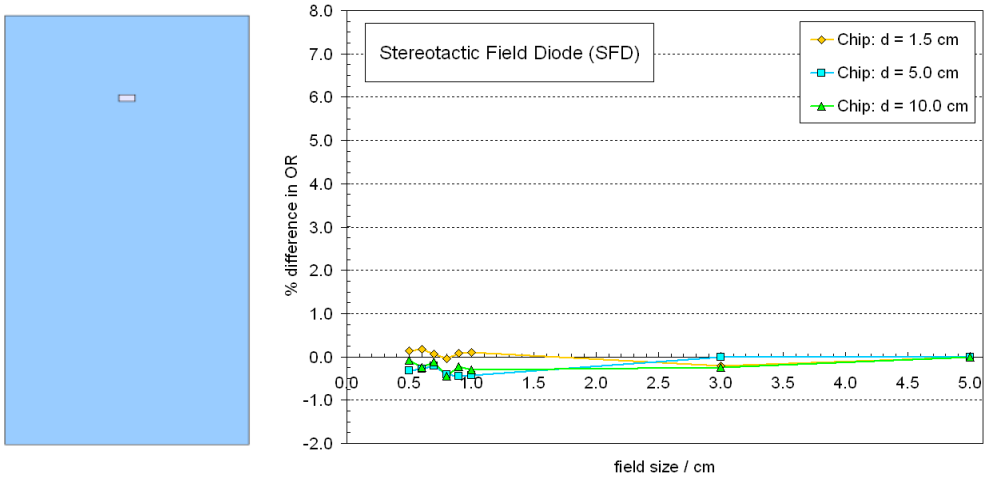

Figure 4.1 The percent difference in $OR^{f_{clin}}_{det_{MC}}$ between the complete SFD unshielded diode model and a chip in water model.

4.3 Results

4.3.1 Model simplification: Percent difference in output and correction factors

Shown in Figure 4.1 are the percent difference in $OR^{f_{clin}}_{det_{MC}}$ calculated between the complete SFD model and an equivalent silicon chip volume in water. Modelling the detector as a chip in water produced simulated output ratios to within 1% of that calculated using the complete detector models. Thus for this diode, a simplified SFD, which does not include the surrounding

materials, protective cover, stainless steel stem and coaxial cable, can be used to calculate $OR_{det_{MC}}^{f_{clin}}$ for the SFD detector.

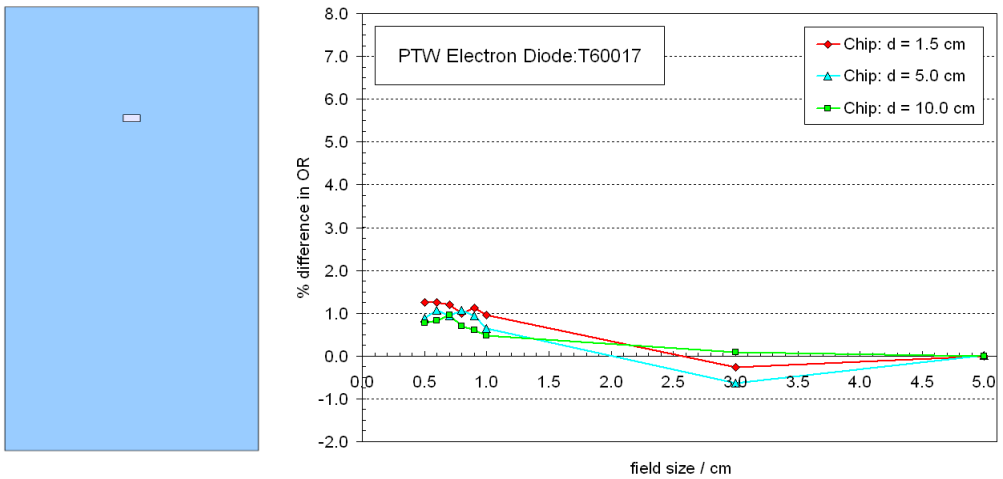

(A)

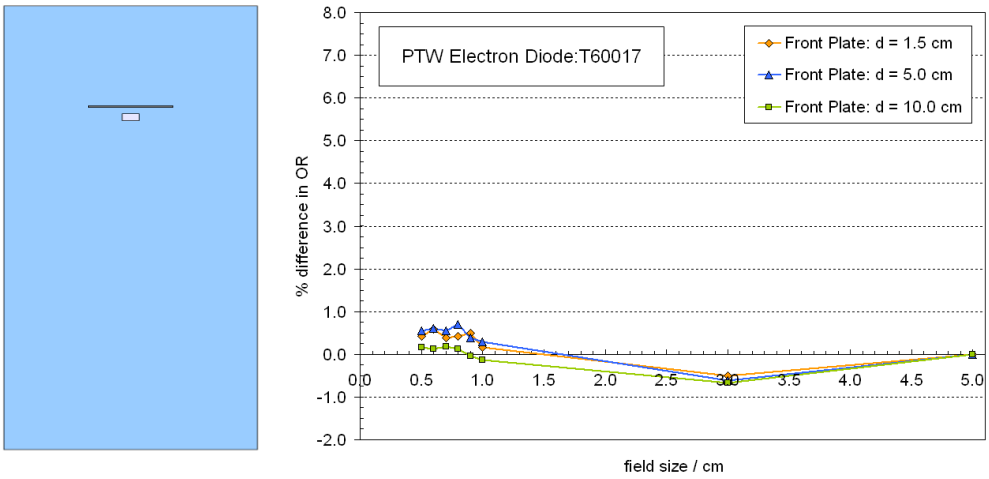

(B)

Figure 4.2 The percent difference in relative output between the complete T60017 unshielded diode model and (A) a chip in water and (B) a chip in water plus the thin filter plate located in front of the silicon chip itself.

Shown in Figure 4.2 are the percent differences in $OR_{det_{MC}}^{f_{clin}}$ between the complete T60017 unshielded diode model and two different simplified

models: (A) just the equivalent silicon chip volume in water and (B) the same silicon chip volume in water, but also including the thin filter plate located upstream. The percent difference data does show that the T60017 diode model can be simplified (Figure 4.2(B)) to produce output ratios within 1.0% of that calculated using the complete model. The percent difference was greater at d = 1.5 and 5.0 cm than at d = 10.0 cm and suggests that the filter plate produces a spectral perturbation removed by the surrounding materials at the shallower detector depths. Regardless, the difference in output ratio between the simplified (including filter plate) and complete detector models are within 1.0% and clearly show that materials other than the chip are required in modelling electron diodes from PTW as noted by Francescon *et al* [45].

Shown in Figures 4.3 and 4.4 are the percent difference in simulated $OR_{det_{MC}}^{f_{clin}}$ between the complete T60016 shielded diode model and that of just the equivalent silicon chip volume in water and other models which include the high density “plate”, “well” and “can”. The percent difference data demonstrates the influence each component of the shielding geometry has on the simulated output ratios. Although more of the detector geometry is required, the data does support the use of a simplified model - when $OR_{det_{MC}}^{f_{clin}}$ is to be calculated to within 1.0% of the complete detector simulation.

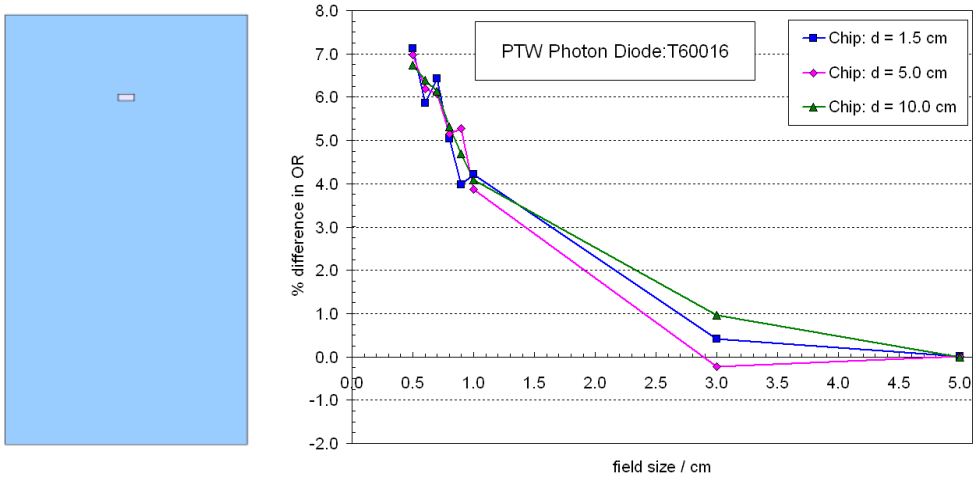

(A)

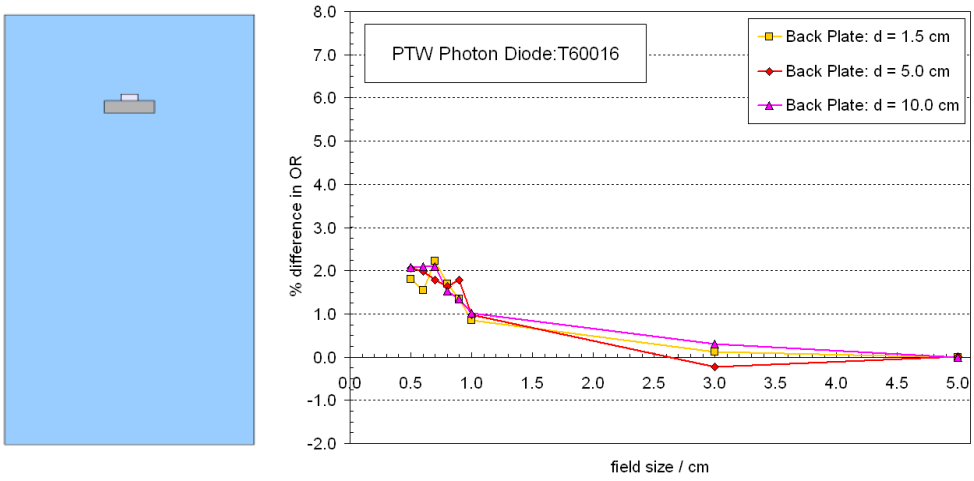

(B)

Figure 4.3 The percent differences in simulated $OR_{det_{MC}}^{f_{clin}}$ between the complete T60016 model and the (A) chip in water, (B) chip in water plus the high density backing "plate" as shown.

The average (± 1 SD) percent difference taken over all values shown in Table 1 was -0.63% (± 0.53%). The detector specific values for the simplified SFD, T60016 and T60017 models were as follows: -0.67% (± 0.53%), -0.66% (± 0.70%) and -0.55% (± 0.40%). Due to the statistical nature of the calculations the percent difference distribution was very nearly Gaussian and

ranged between -1.55% and + 0.25%. The negative percent difference is the result of a systematic output ratio under-response from the simplified detector models and corroborates the assumption that most of the housing materials alter measured relative output ratios at small fields to less than 1.0%. In most cases the percent difference is less than the total statistical uncertainty associated with the calculated values at approximately ± 1.00%.

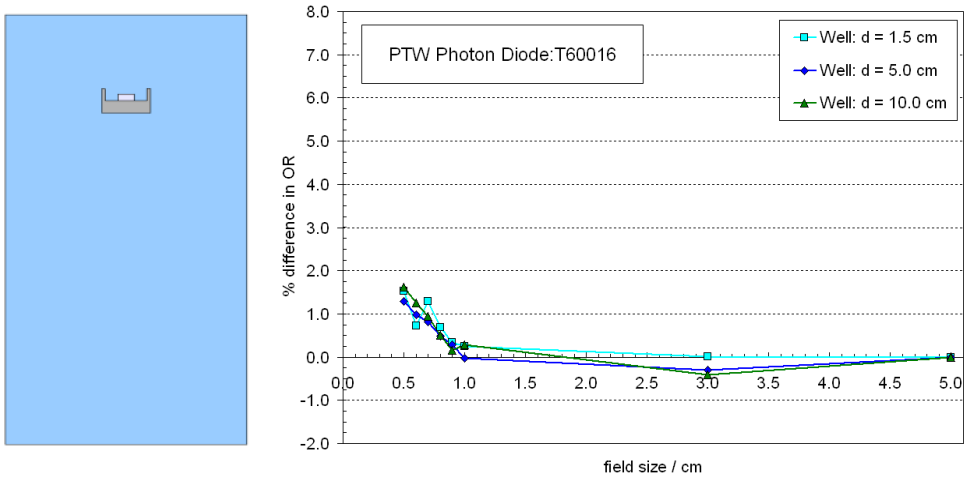

(A)

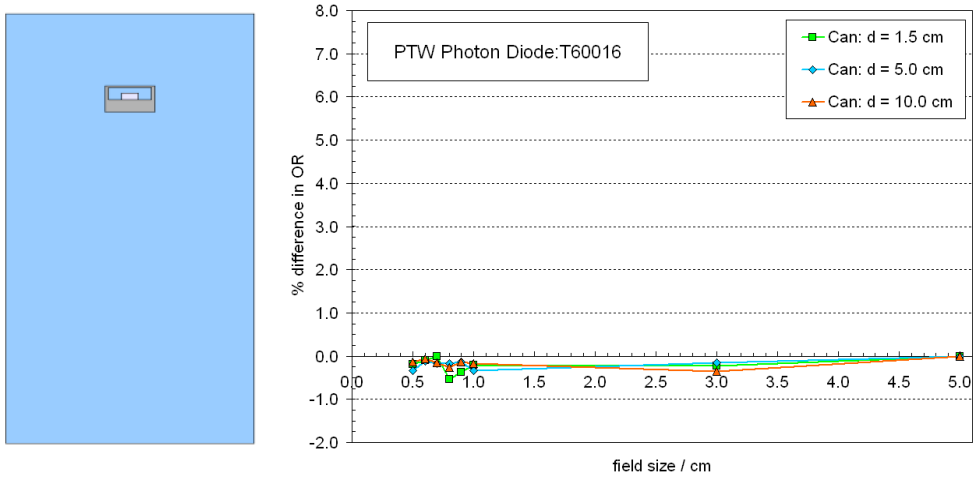

(B)

Figure 4.4 The percent differences in simulated $OR_{det_{MC}}^{f_{clin}}$ between the complete T60016 model and the (A) “well” and (B) “can” as shown.

Table 4.1 The percent difference in $k_{Q_{clin},Q_{msr}}^{f_{clin},f_{msr}}$ calculated using the complete and simplified detector models for a source parameterization of 6.2 MeV with a FWHM = 0.110 cm.

Difference in $k_{Q_{clin},Q_{msr}}^{f_{clin},f_{msr}}$	Square Field Size of Side					
	1.00 cm	0.90 cm	0.80 cm	0.70 cm	0.60 cm	0.50 cm
SFD	0.25%	-0.63%	-0.58%	-0.73%	-1.23%	-1.15%
T60016	-0.56%	-1.55%	-1.46%	-0.27%	-0.41%	0.25%
T60017	0.07%	-0.64%	-0.80%	-0.27%	-1.06%	-0.62%

4.3.2 Active volume dimension, relative response and reporting correction factors

Figure 4.5 shows the $OR_{w_{MC}}^{f_{clin}}$ and $OR_{Si_{MC}}^{f_{clin}}$ data as a function of active volume radius for the square field size of side 0.5 cm with respect to a square field size of side 5.0 cm. As one would expect for small field sizes, the relative output decreases as a function of active volume radius increase for the fixed small field size - this is often referred to as volume averaging. The data for active volume sizes smaller than that of the modelled detectors (R ≈ 0.50 mm) reveals that if the radial chip size could be made smaller, the difference between measured output ratios and the actual relative output in water could be reduced to less than 1.0%. However, the technical challenges associated

with making such a dosimeter would require exploration and the influence of the surrounding materials potentially problematic.

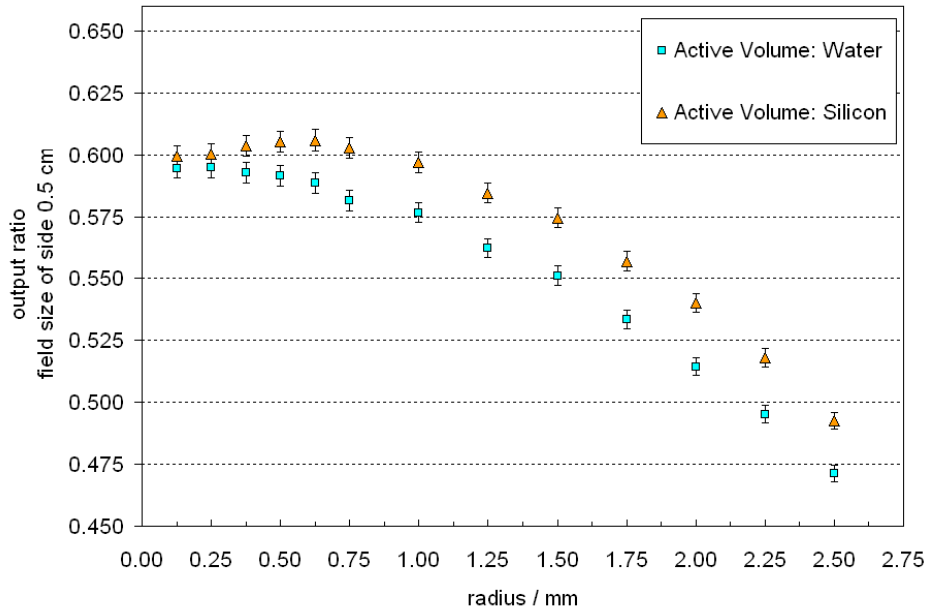

Figure 4.5 The change in $OR_{w_{MC}}^{f_{clin}}$ and $OR_{Si_{MC}}^{f_{clin}}$ as a function of active volume radius for the square f_{clin} of side 0.5 cm with respect to a square f_{msr} of side 5.0 cm.

Plotted in Figure 4.6 are the normalized response factors for a square field size of side 0.5 cm calculated using: (1) equivalent silicon and water volumes and (2) a constant, point like, water volume of radius 0.125 mm. A number of important aspects related to calculating and reporting small field diode detector correction factors can be elicited from this data. The first, and most obvious, is the difference in reporting detector response using equivalent and point like water volumes respectively. One can see that calculating the correction between equivalent volumes of silicon and water

for radii greater than that of the detectors modelled in this work (R ≈ 0.50 mm) results in a reported over-response for all cases.

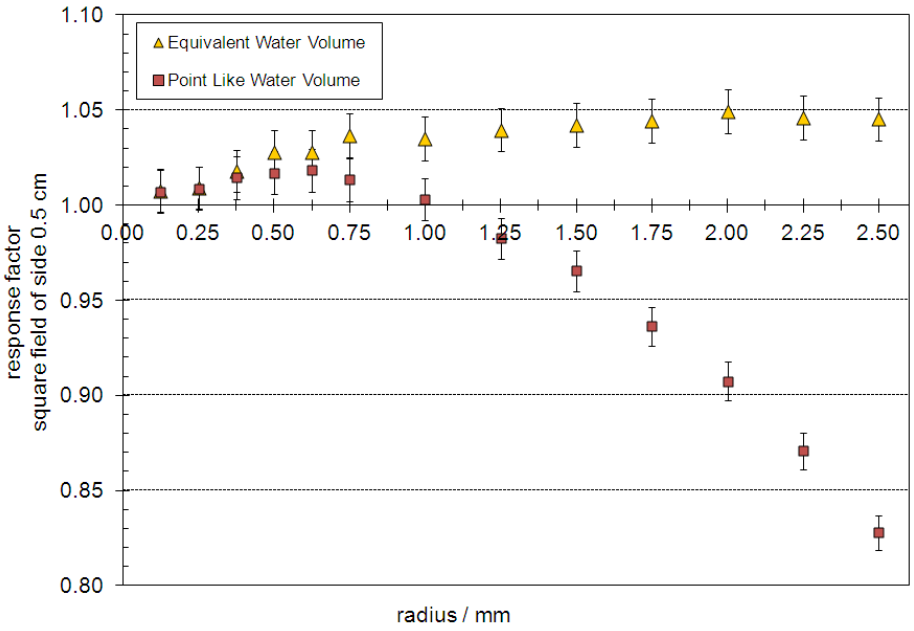

Figure 4.6 The change in response factor plotted as a function of active volume radius, for a square field size of side 0.5 cm, calculated using an equivalent water volume as that of the silicon chip and a point like water volume of radius 0.125 mm.

The dosimetry formalism set out by Alfonso *et al* specifies that the absorbed dose to water be reported to a reference point and not an equivalent volume of water. Therefore, providing response factors and/or $k_{Q_{clin},Q_{msr}}^{f_{clin},f_{msr}}$ for R ≥ 0.625 mm using equivalent volumes is clearly inaccurate. At a chip radius of 1.00 mm, which is approximately equal to that of the electron field diode, the silicon over-response is off-set by the volume effect - resulting in no correction. However, silicon diode detectors with an active volume radius

greater than 1.00 mm will under respond with respect to the absorbed dose to water at a point like small volume and therefore will require a correction that is greater than unity.

4.3.3 Sensitivity to source parameterization

Although the simplified detector models do produce $k_{Q_{clin},Q_{msr}}^{f_{clin},f_{msr}}$ that differ very slightly from that of the complete models, they were deemed suitable for investigating the influence of source parameterization. Figures 4.7 and 4.8 show the change in $k_{Q_{clin},Q_{msr}}^{f_{clin},f_{msr}}$, as a function of field size, calculated using the three simplified detector models and various electron energies and FWHMs. At each field size, the required $k_{Q_{clin},Q_{msr}}^{f_{clin},f_{msr}}$ was found to be very nearly equivalent for all source parameterizations.

4.4 Discussion

Testing the application of simplified diode detector models for Monte Carlo small field dosimetry does directly validate the usual assumption that most of the surrounding materials have little influence on small field relative output ratio measurements, except for added high density materials in close proximity to the silicon chip with the shielding used in the T60016 being one clear example.

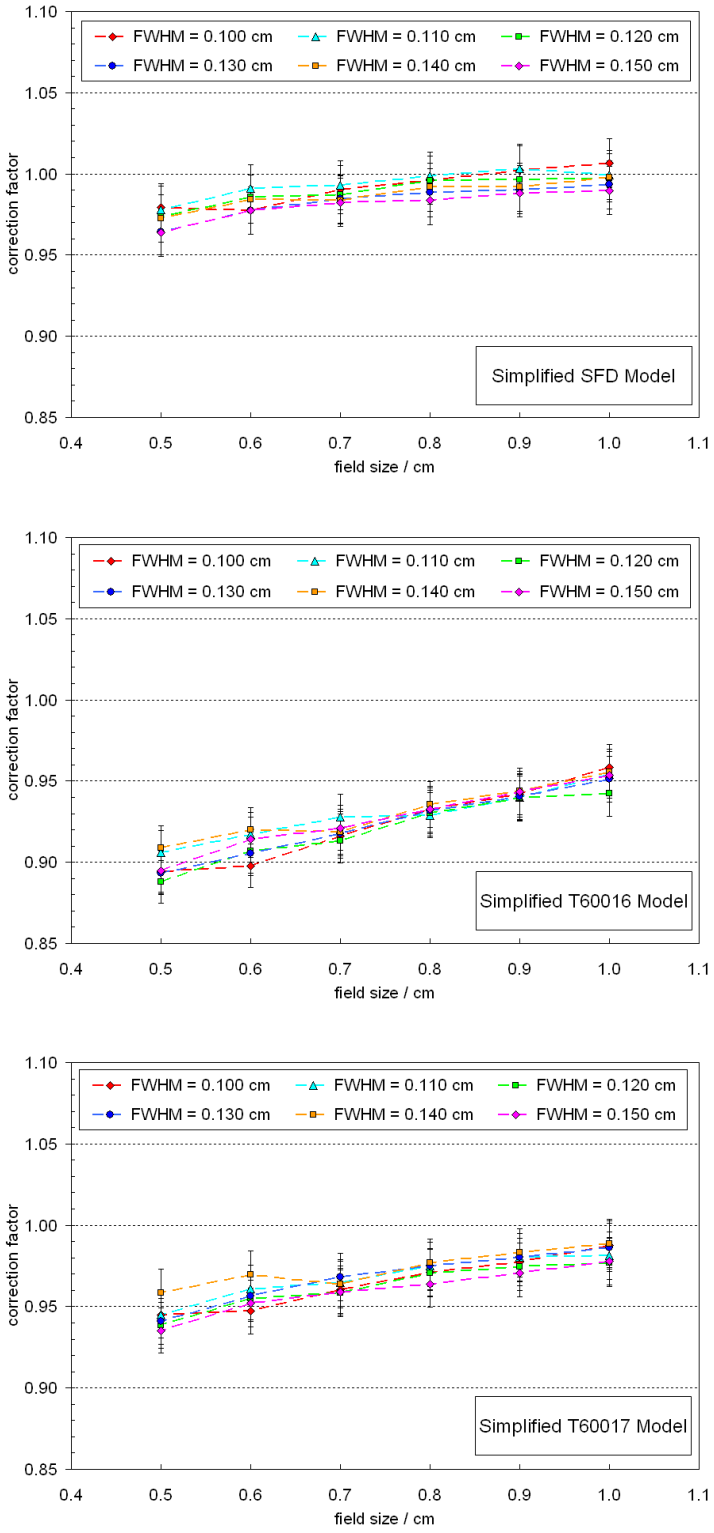

Figure 4.7 $k_{Q_{clin},Q_{msr}}^{f_{clin},f_{msr}}$ calculated using the simplified SFD (top), T60017 (middle) and T60016 (bottom) models and various electron source widths.

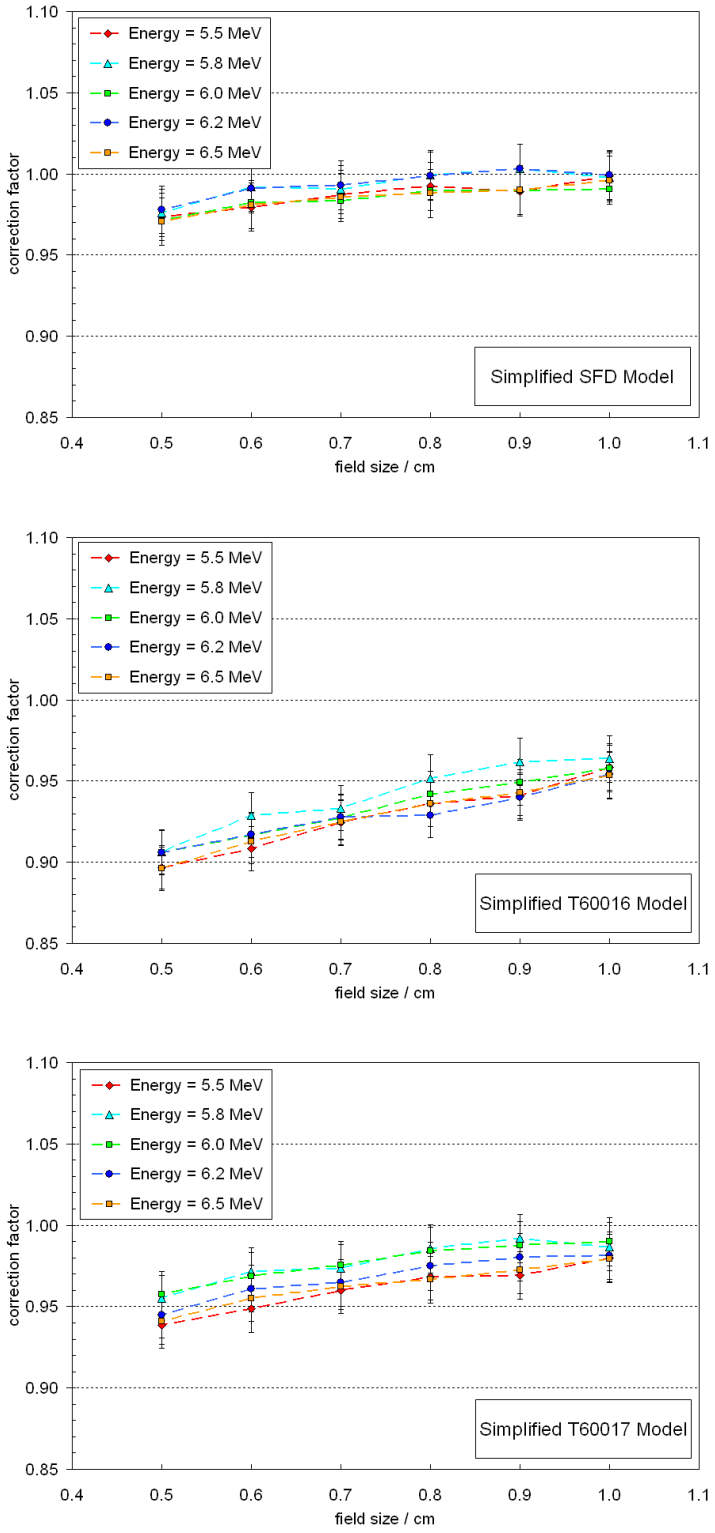

Figure 4.8 $k_{Q_{clin},Q_{msr}}^{f_{clin},f_{msr}}$ calculated using the simplified SFD (top), T60017 (middle) and T60016 (bottom) models and various electron source energies.

The results presented here and the work of Scott *et al* [98,99] revealed good agreement between experimental and Monte Carlo simulated data for simplified SFD and EFD detector models. From the imaging work of McKerracher and Thwaites [80], it appears the SFD and EFD are manufactured using similar materials and differ only in chip diameter and the use of a centering ring for the EFD chip, with the Scott *et al* data suggesting the centering ring has little effect on the accuracy between simulated and measured output ratios. Eklund and Ahnesjö [41] conclude that the spectral perturbations resulting from the encapsulating material of the EFD diode are negligible. Although the Eklund and Ahnesjö data is not specific to small fields the same general result should still hold. This is supported by the near equivalence in $OR_{det_{MC}}^{f_{clin}}$ between the complete and the simplified SFD detector model.

Simplifying detector geometries is an attractive option when one considers the simulation times associated with Monte Carlo small field calculations. Although the average difference in $k_{Q_{clin},Q_{msr}}^{f_{clin},f_{msr}}$ calculated using the complete and simplified models was found to be -0.67%, using simplified models within the recently proposed small field dosimetry formalism could be debated. In short, what may appear to be a negligible difference in simulated $OR_{det_{MC}}^{f_{clin}}$ may result in a systematic error of up to ~1.0% being made when correcting measured, small field, output ratios. However, to ensure the systematic error in correction is less than ~1.0% the effects of any high density shielding materials must be included in the model and the application

of the correction factors for shielded and unshielded diode detectors be made with care.

Systematic differences between data calculated using simplified and complete detector models also pose a problem when trying to interpret analytic methods such as the generalized field model (GFM) of Eklund and Ahnesjö [42]. The authors use the GFM approach to calculate response factor data for a simplified detector model at square field sizes of side 0.5 and 1.0 cm for a simplified chip in water model having a 1.0 mm active volume radius perpendicular to the beam axis. The GFM model alone predicts an increase in response factor for fields of side smaller than 3.0 cm, which contradicted an under-response predicted by the investigators own Monte Carlo simulation data. A correction was then applied to the GFM data to account for the volume effect across the surface area of the silicon chip. The resulting data was found to be in better agreement with the Monte Carlo calculated under-response. However, both data sets contradict the simulation data shown here, which reveals the silicon chip over-response is off-set by the volume effect for an active volume with R = 1.0 mm. In the end, a combined approach using Monte Carlo and analytic methods may provide most useful in characterizing silicon diode detectors for use in small field dosimetry.

It is well documented that if the electron spot cannot be fully viewed from the center of the field, as is the case for small fields, then the geometrical penumbra will extend across the entire field [33,53,112]. The implications for

Monte Carlo simulation of small field geometries is a high sensitivity of central axis relative output to the simulated electron source size (FWHM). Apart from the recent work of Francescon *et al*, there has been little reported on the sensitivity of $k_{Q_{clin},Q_{msr}}^{f_{clin},f_{msr}}$ to changes in the simulated energy and spatial distribution of electrons incident on the target. The near invariance of $k_{Q_{clin},Q_{msr}}^{f_{clin},f_{msr}}$ to changes in the electron energy between 5.5 and 6.5 MeV, and FWHM between 0.100 and 0.150 cm, implies that $k_{Q_{clin},Q_{msr}}^{f_{clin},f_{msr}}$ correction factors reported in Chapter 3 may be applied to experimental data measured on different treatment machines of the same make, model and beam quality ($TPR_{20,10}$ = 0.673). In fact, this is exactly what Pantelis *et al* [89] do by using the published factors of Francescon *et al* [45] to correct relative output data measured on a Cyberknife.

The invariance of $k_{Q_{clin},Q_{msr}}^{f_{clin},f_{msr}}$ to electron spot size should not be dismissed as somewhat trivial as the implications for clinical practice may prove to be of great value. In essence, the clinical implementation of the proposed dosimetry formalism may not require experimental FWHM validation prior to using published $k_{Q_{clin},Q_{msr}}^{f_{clin},f_{msr}}$ values. It is conceivable that only a large field beam quality index be required for clinical implementation. Moreover, using published data, or averaged values as presented here and by Francescon *et al* [45], has the potential to greatly reduce inter-institutional uncertainties when reporting small field dosimetric data. This is however where a code of

practice would assist in outlining the steps required for measuring, reporting and auditing small field dosimetry.

4.5 Conclusion

Three general conclusions come out of this work: (1) detector models can be simplified to produce $OR_{det_{MC}}^{f_{clin}}$ to within 1.0% of those calculated using the complete geometry, (2) diode detectors of smaller active radius require less of a correction and (3) $k_{Q_{clin},Q_{msr}}^{f_{clin},f_{msr}}$ is insensitive to the electron energy and spot size variations investigated.

Chapter 5
Small field dosimetric characterization of a new 160-leaf MLC

5.1 Introduction

External beam radiation therapy treatments have historically been delivered using simple jaw or block collimation, and most traditional linear accelerator based stereotactic radiosurgery (SRS) treatments delivered with fixed circular collimators. In both cases, as in all radiotherapy, the goal of treatment has been to deliver a therapeutic dose of radiation to the target volume while sparing the surrounding normal tissues [11]. The development, and clinical implementation, of the multi-leaf collimator (MLC) has removed many of the constraints associated with fixed block external beam radiotherapy and ultimately facilitated intensity modulation (IMRT) as a viable and widespread treatment modality [15]. SRS treatment techniques using MLC collimation have also evolved and now include dynamic conformal arc therapies (DCA) shown to produce excellent conformality [51]. Clearly the collimator of choice for both external beam and radiosurgery treatment techniques has naturally converged towards the use of MLCs.

The thorough micro-MLC commissioning work of Cosgrove *et al* [25] solidified the use of leaf transmission, leakage and penumbra evaluation as a method of initial collimator characterization for use in SRS applications. The main practical advantage of using the micro-MLC for SRS, as stated by

the authors, was that irregularly shaped target volumes could be treated using a single isocenter instead of traditional cone based, multi-isocenter, arc plans. Subsequent work investigating MLC systems for use in SRS have tended to focus on reporting differences in conformity index (CI) as a function of leaf width [21]. The work of Monk *et al* [84] showed that only a small improvement in CI, as a function of leaf width reduction from 5.0 mm to 3.0 mm (projected at isocenter), can be expected for clinically relevant target sizes between 0.8 cm^3 and 46.7 cm^3. The authors emphasized the real clinical importance of their work was to show a 5% reduction in critical structure volume encompassed by the 50% and 70% isodose levels as a function of leaf width. Dhabaan *et al* [35] present a similar evaluation for the BrainLAB 2.5 mm high definition MLC (HDMLC) compared to the Varian 5.0 mm Millennium 120-MLC. In all cases the dose to normal tissue at the 50%, 70% and 90% isodose levels were generally reduced by between 2.0% and 5.0% - with the greatest reduction of 8.0% correlated to the largest target volumes.

Clearly beam penumbra is of clinical significance when characterizing an MLC for use in small field applications; yet most published dosimetric MLC characterizations have not included penumbral and/or field size width uncertainties as a function of MLC performance. The work presented in Chapter 2 and that of Francescon *et al* [45] have explored various aspects associated with small field relative output uncertainties. The main source of Type-A central axis relative output uncertainty can be attributed to the reproducibility of the collimator position (i.e. field size). However, no

methodology for measuring or reporting on uncertainties associated with penumbral width and/or field size was developed as part of their work.

The work presented in Chapters 3 and 4, and that of Francescon *et al* [44,45], have shown commercial diode detectors to be a reasonable choice for small field dosimetry applications. However, care must be taken when selecting between shielded (photon) and unshielded (electron) diodes. In general, the correction factors required for shielded diodes are approximately twice that required for the unshielded diodes. Ralston *et al* [92] explored the use of an air-core fibre optic scintillation dosimeter (FOD) for small field relative output dosimetry and showed the FOD can be used for the experimental determination of $k_{Q_{clin},Q_{msr}}^{f_{clin},f_{msr}}$ correction factors for other detector types such as shielded and unshielded diodes.

The goal of this portion of the work was to perform a 6 MV small field dosimetric characterization of the Agility 160-leaf MLC available from Elekta - already characterized for conventional field sizes by Cosgrove *et al* [26]. The work presented here includes central axis relative output measurements as well as profile measurement characterization and uncertainty analysis. $k_{Q_{clin},Q_{msr}}^{f_{clin},f_{msr}}$ correction factors were experimentally derived for a number of commercial diode detectors using FOD data measured under the same conditions. For comparison, all measurements and analysis were repeated for the Elekta 80-leaf MLCi2 on a beam matched linac.

5.2 Methods

5.2.1 MLC Description

The 160-leaf Agility MLC makes use of interdigitating leaves with a 5.0 mm leaf width projected at the isocenter. The leaves are mounted on dynamic leaf guides (DLG) that have a total translational travel of 15.0 cm in the MLC direction. The leaves themselves have a total travel distance of 20.0 cm and a minimum definable field size of 0.5 cm x 0.5 cm. The combination of DLG and leaf movement creates an MLC range of motion from 20.0 cm to -15.0 cm. An optical system is used for leaf positioning. Synthetic rubies are mounted on the upper edges of the leaves near the leaf tips, these rubies produce near infra-red (IR) fluorescence when illuminated by ultra-violet (UV) light provided by an LED. The resulting fluorescence is then detected by a filtered camera system and the signal used to locate and monitor leaf position. The Agility head incorporates a pair of sculpted diaphragms which move orthogonally to the direction of leaf travel. The radiation defining faces of the sculpted diaphragms are curved and provide a full shielding thickness at the edge of the field as well as the gap between any closed leaf pair outside the defined field size. The diaphragms have a range of motion from 20.0 cm to -12.0 cm.

5.2.2 Scintillator and diode detector descriptions

The air-core fibre optic scintillation dosimeter [69,70], as described by Liu *et al* [74], makes use of a cylindrical BC400 polyvinyl plastic scintillator (ρ = 1.032 g·cm^{-3}) that is 1.0 mm in both length and diameter (see Figure 5.1). The scintillator is coupled to a 120 mm long silvered air core light guide. An optic fibre inserted into the opposite end of the light guide transmits the light signal from the scintillator to a Hamamatsu photo-multiplier tube (PMT) located outside the treatment bunker [75]. The FOD clearly satisfies the small field detector criteria set out by Laud *et al* [71], who emphasize high spatial resolution and water equivalence as desirable attributes and therefore can be used for experimental determination of diode detector small field replacement correction factors.

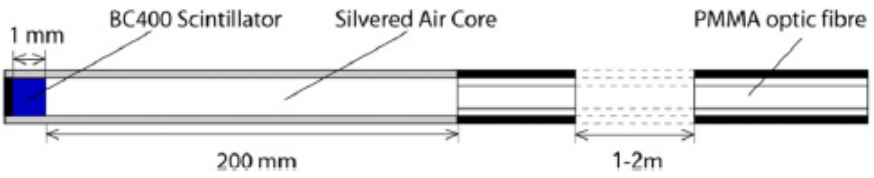

Figure 5.1 A diagram of the air core plastic scintillator detector [74].

The set of diode detectors used in this study were both shielded and unshielded, with the T60016 being shielded and the stereotactic field diode (SFD) and T60017 being unshielded. These diodes were selected as they each have a similar active area quoted by the manufacturers at ≤ 1.0 mm^2. In general, shielded diodes make use of high density materials placed

around the silicon chip which help eliminate the disproportionate number of low-energy scattered photons responsible for diode detector over-response in large fields [48]. In unshielded diodes the shielding material is replaced with a polymer plastic [80] and therefore eliminates the excessive electron scatter from the shield into the active volume.

5.2.3 Experimental procedures

5.2.3.1 Relative output measurement and uncertainty analysis

Detector specific output ratios are defined, as they have been throughout this work, as the ratio of detector (*det*) readings (*M*) taken between the clinical field size of interest (f_{clin}) and the machine-specific reference field (f_{msr}) such that,

$$OR_{det}^{f_{clin}} = \frac{M_{Q_{clin}}^{f_{clin}}}{M_{Q_{msr}}^{f_{msr}}} . \qquad (5.1)$$

$OR_{det}^{f_{clin}}$ measurements were performed at a nominal 6 MV beam energy on two beam matched Elekta Synergy medical linear accelerators (linac) - one fitted with the new Agility 160-leaf MLC and the other an 80-leaf MLCi2. Field sizes were set using the combined MLC and diaphragm for nominal square field sizes of side 3.0, 1.0, 0.9, 0.8, 0.7, 0.6 and 0.5 cm. In all cases $OR_{det}^{f_{clin}}$ was calculated using the square field size of side 3.0 cm as the

machine-specific reference field. For the Agility MLC, two additional leaf pairs on either side of the field aperture were kept in the open, field defining, position. All other out-of-field leaves were kept retracted at a distance of 20 mm from the Y2-Y1 axis. This results in an out-of-field leaf separation of 40 mm but is not an issue because the leaf separation is underneath the thick part of the sculpted diaphragms. For the MLCi2, one additional leaf pair on either side of the field aperture was kept in the open, field defining, position. All other out-of-field leaves were kept in the fully closed position at a distance of 2.5 mm from the Y2-Y1 axis. Collimating each field in this manner ensured that the field size along the axis orthogonal to the leaf travel was defined by the diaphragms alone.

Measurements were made at a depth of 10.0 cm with the long axis of the diode detectors placed parallel to the beam axis such that the active volume was positioned at isocenter. The FOD was placed perpendicular to the beam axis with the active volume located at isocenter. The well documented Cherenkov signal [69,70,74,75] was background subtracted by making a second set of measurements with only the optic fibre connected to the PMT. Positional fine tuning was performed in all cases to ensure the active volume of each detector was positioned at the radiation isocenter and not just centred on the light field. This positional fine tuning was validated by ensuring the instantaneous detector signal off axis was less than that at the radiation isocenter. Following this method ensured the detector positional uncertainty was limited only by the accuracy of the MP3 water tank system quoted by the manufacturer at ± 0.1 mm.

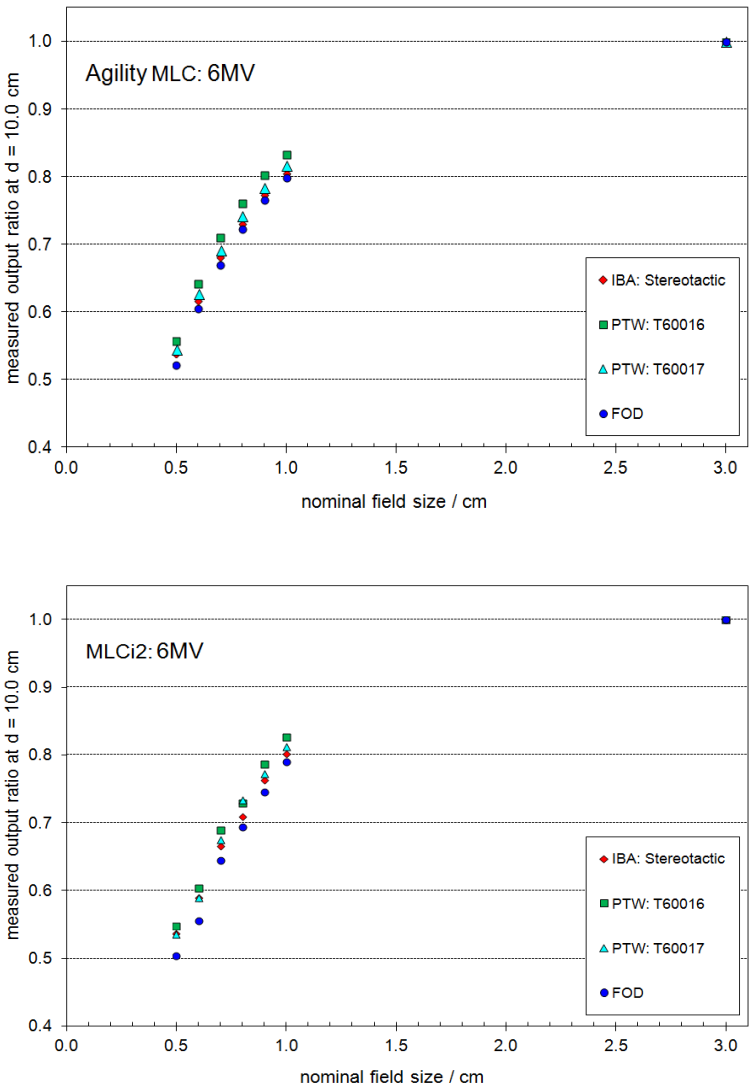

Figure 5.2 $OR_{det}^{f_{clin}}$ measured at a nominal 6 MV beam energy on two beam matched linacs, one with the 160-leaf Agility MLC (top) and the other the 80-leaf MLCi2 (bottom). A square field of side 3.0 cm was used as the machine-specific reference field. Naturally the measured $OR_{det}^{f_{clin}}$ varied as a function of both detector and MLC design.

The $OR_{det}^{f_{clin}}$ measurements were repeated three times. The water phantom, detector position and collimation were reset between each experimental session and five output readings taken at each field size. Diaphragm and

MLC repositioning between experimental sessions followed an iteration of retracting the collimators out to the reference field size and then back into the next field size. This was repeated until the field size reported by the control system was the same as the field size of interest. A mean output ratio was calculated across the three experimental sessions for each detector. The Type-A uncertainty associated with experimental set-up was characterized by calculating the standard percent error on $OR_{det}^{f_{clin}}$ across the three experimental sessions, which, given the sample size, provides a confidence interval of 90% for a coverage factor k = 2.0.

A mean coefficient of variation (CV) was calculated across the three independent experimental sessions using the session specific CV values calculated across the five independent readings. Calculating the mean CV in just such a manner characterizes the measurement precision associated with the performance of the detector-linac system alone. As noted in Chapter 2, following this methodology identifies two distinct Type-A uncertainty contributions: one due to detector and beam fluctuations (constant set-up) and another due to re-establishing the entire set-up.

5.2.3.2 Profile measurements and field size analysis

Profile measurements were taken for nominal square field sizes of 1.0, 0.9, 0.8, 0.7, 0.6 and 0.5 cm. Measurements were made at a depth of 10.0 cm with the long axis of the SFD detector placed parallel to the beam axis. Positional fine tuning was performed to ensure the active volume was

located at the radiation isocenter and not just positioned at the light field center. Following this method ensured the uncertainty in detector position associated with the profile and output ratio measurements was minimized and limited only by the water tank positional accuracy of ± 0.1 mm.

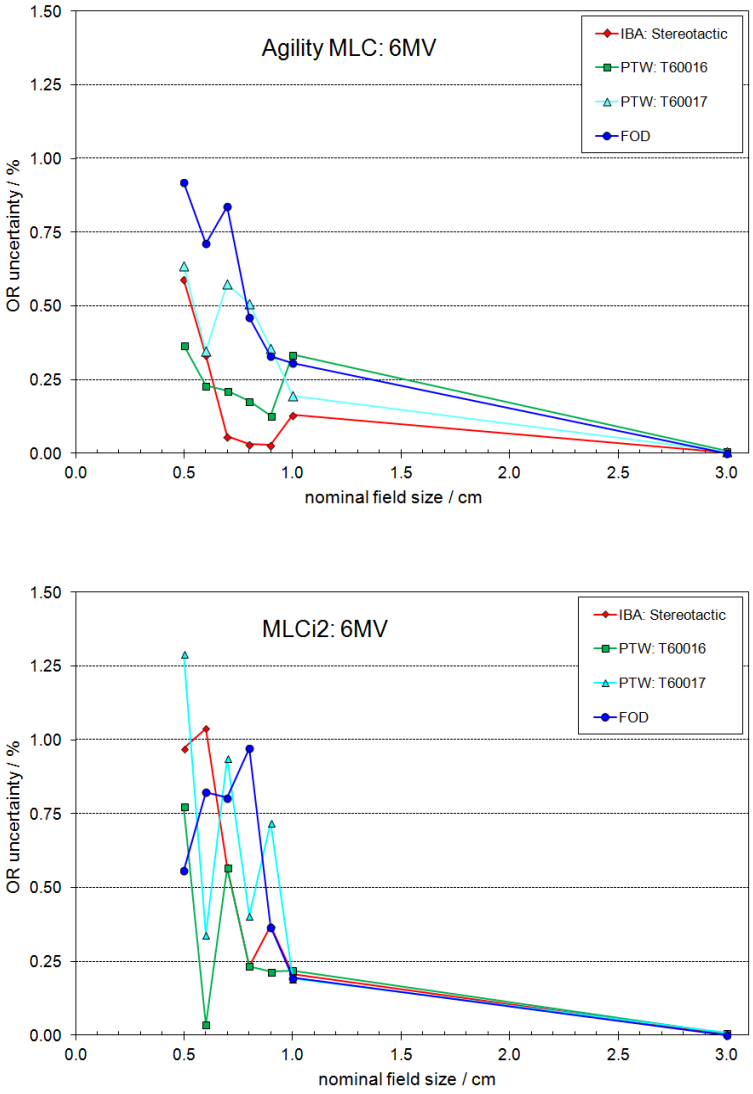

Figure 5.3 The standard percent error on the mean $OR_{det}^{f_{clin}}$ calculated across the three experimental sessions for the Agility (top) and MLCi2 (bottom).

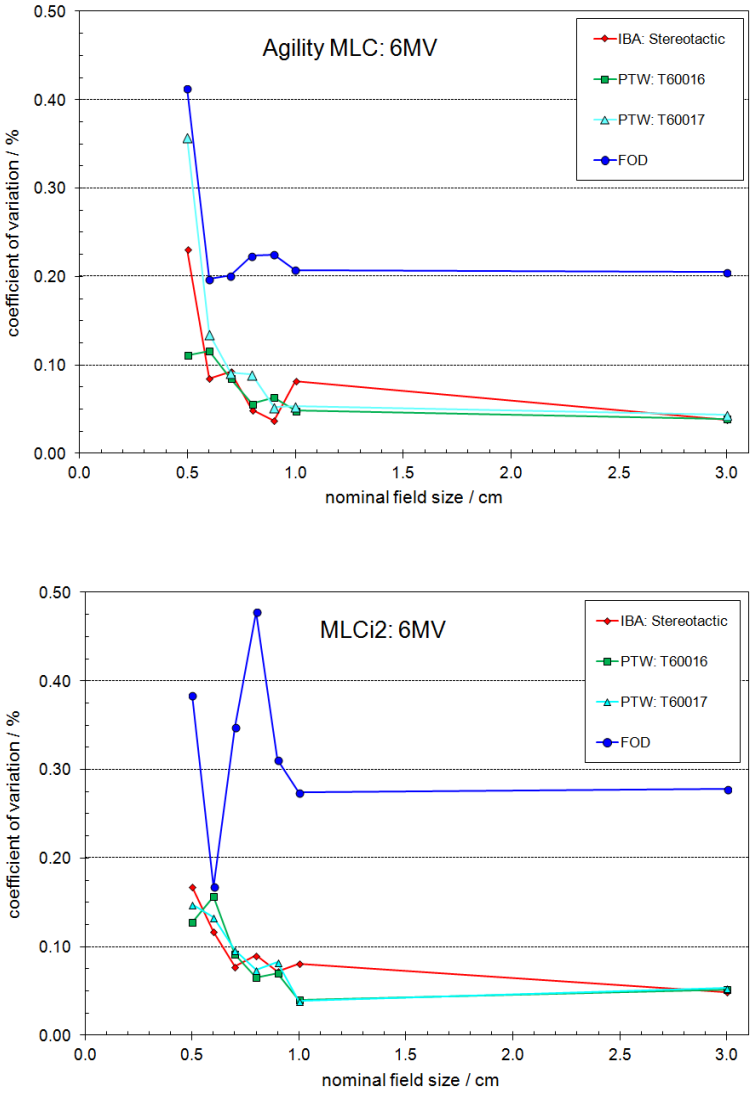

Figure 5.4 The mean coefficient of variation (CV) calculated for each detector calculated across the three independent experimental session for the Agility (top) and MLCi2 (bottom).

Profile measurements were repeated three times. The diaphragm and MLC positions were reset between each experimental session as detailed above. The water phantom position was left unchanged but the detector initial position fined tuned at the radiation isocenter as detailed above. Five profile measurements were taken for each field size along each axis (in-plane and

x-plane) during each experimental session. A mean field size, reported at the 50% isodose level, was calculated across the three experimental sessions. The Type-A uncertainty on field size was analyzed by calculating the standard error on the mean field size across the three experimental sessions - which again provides a confidence interval of 90% for a coverage factor k = 2.0. Measuring profiles in just such a manner characterizes the field size uncertainty associated with re-collimation only and nearly eliminates experimental set-up as a source of error.

5.2.4 Diode detector replacement correction factors

As outlined in Chapter 1, Alfonso *et al* [1] have proposed a small field dosimetry formalism that makes use of a field factor ($\Omega_{Q_{clin},Q_{msr}}^{f_{clin},f_{msr}}$) which converts absorbed dose to water for the machine-specific reference field to that of the clinical field size of interest such that,

$$D_{w,Q_{clin}}^{f_{clin}} = D_{w,Q_{msr}}^{f_{msr}} \cdot \Omega_{Q_{clin},Q_{msr}}^{f_{clin},f_{msr}} \qquad (5.2)$$

where,

$$\Omega_{Q_{clin},Q_{msr}}^{f_{clin},f_{msr}} = \frac{M_{Q_{clin}}^{f_{clin}}}{M_{Q_{msr}}^{f_{msr}}} \cdot k_{Q_{clin},Q_{msr}}^{f_{clin},f_{msr}} . \qquad (5.3)$$

$M_{Q_{clin}}^{f_{clin}}$ and $M_{Q_{msr}}^{f_{clin}}$ are detector readings taken at f_{clin} and f_{msr} respectively and $k_{Q_{clin},Q_{msr}}^{f_{clin},f_{msr}}$ the detector-specific correction factor which converts dose to the active volume of the detector to a point dose in water for the same f_{clin}. If, as Pantelis *et al* [88,89] note, $k_{Q_{clin},Q_{msr}}^{f_{clin},f_{msr}}$ equals unity for a given detector then the measured $OR_{det}^{f_{clin}}$ can be considered equivalent to $\Omega_{Q_{clin},Q_{msr}}^{f_{clin},f_{msr}}$ and used to determine $k_{Q_{clin},Q_{msr}}^{f_{clin},f_{msr}}$ for other detectors experimentally. $k_{Q_{clin},Q_{msr}}^{f_{clin},f_{msr}}$ values were calculated for each diode detector using the mean experimental output ratio ($OR_{det}^{f_{clin}}$) and the mean experimental FOD output ratio ($OR_{FOD}^{f_{clin}}$) such that,

$$k_{Q_{clin},Q_{msr}}^{f_{clin},f_{msr}} = \frac{OR_{FOD}^{f_{clin}}}{OR_{det}^{f_{clin}}}. \qquad (5.4)$$

The uncertainty on $k_{Q_{clin},Q_{msr}}^{f_{clin},f_{msr}}$ can simply be calculated as the sum of the squares of the uncertainties on $OR_{FOD}^{f_{clin}}$ and $OR_{det}^{f_{clin}}$ respectively.

5.3 Results

Plotted in Figure 5.2 are the output ratios normalized with respect to a square, machine-specific reference field, of side 3.0 cm. Although the data was acquired on beam matched linacs the output ratios do differ as a function of both detector type and MLC design. In all cases the diode

detectors over-respond with respect to the FOD - which was expected and consistent with similar work reported here and in the literature.

Table 5.1 The mean central axis positions (CAX) and field sizes (FS) with the associated standard experimental uncertainty reported at a 90% confidence interval for the Agility MLC.

Nominal FS (Agility)	CAX (mm)	Average FS (cm)	± FS at 2σ (cm)
1.0 cm	0.00	1.088	0.004
0.9 cm	0.03	0.991	0.002
0.8 cm	0.01	0.899	0.005
0.7 cm	0.02	0.816	0.003
0.6 cm	0.02	0.733	0.001
0.5 cm	0.05	0.654	0.003

Nominal FS (Diaphragm)	CAX (mm)	Average FS (cm)	± FS at 2σ (cm)
1.0 cm	0.01	0.987	0.011
0.9 cm	-0.02	0.903	0.009
0.8 cm	0.02	0.789	0.001
0.7 cm	-0.01	0.691	0.004
0.6 cm	0.03	0.590	0.004
0.5 cm	-0.05	0.494	0.007

Table 5.2 The mean central axis positions (CAX) and field sizes (FS) with the associated standard experimental uncertainty reported at a 90% confidence interval for the MLCi2.

Nominal FS (MLCi2)	CAX (mm)	Average FS (cm)	± FS at 2σ (cm)
1.0 cm	0.03	1.054	0.005
0.9 cm	0.04	0.955	0.018
0.8 cm	-0.07	0.847	0.002
0.7 cm	-0.03	0.774	0.004
0.6 cm	0.04	0.692	0.018
0.5 cm	0.03	0.620	0.028

Nominal FS (Diaphragm)	CAX (mm)	Average FS (cm)	± FS at 2σ (cm)
1.0 cm	0.01	0.987	0.005
0.9 cm	0.03	0.892	0.012
0.8 cm	-0.01	0.784	0.001
0.7 cm	0.02	0.685	0.000
0.6 cm	0.04	0.588	0.002
0.5 cm	0.00	0.509	0.005

Shown in Figure 5.3 is the standard percent error on $OR_{det}^{f_{clin}}$ calculated across the three experimental sessions for the Agility and MLCi2. The $OR_{det}^{f_{clin}}$ uncertainty data is clearly different for each MLC, but not so across the various detectors. The FOD and SFD uncertainty data associated with the Agility MLC data might suggest there are differences between the two

detectors but this is more likely due to experimental chance. This assumption can be rationalized by analyzing the MLCi2 uncertainty data for the same two detectors, which shows no statistical difference.

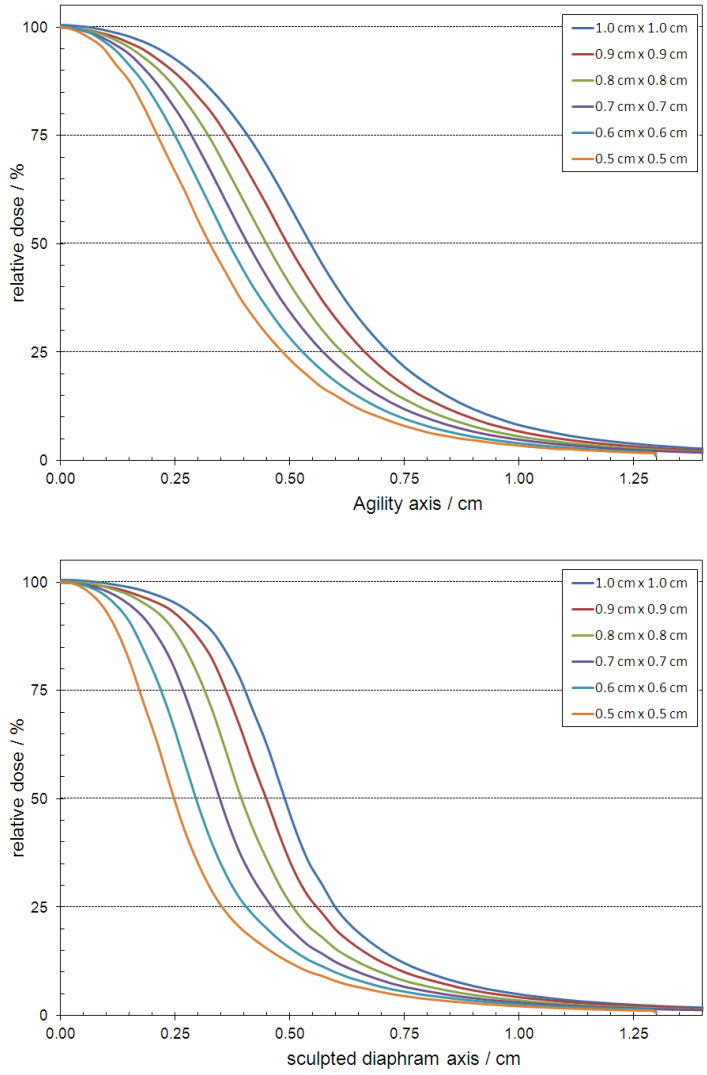

Figure 5.5 Average profile data for the Agility accelerator head measured in water along the leaf-axis (top) and diaphragm axis (bottom).

Figure 5.4 presents the mean CV values for each detector calculated using the CV for each of the three independent experimental sessions. Clearly the CV associated with the FOD measurements is greater than that for the

diodes. This is thought to originate from either the double measurement required for the Cherenkov subtraction process or the signal-to-noise of the Cherenkov radiation itself. Regardless of the source, the difference in measurement precision between the FOD and diode detectors does not translate into a difference in measurement uncertainty, which is dominated by variations in set-up and reproducibility in collimation.

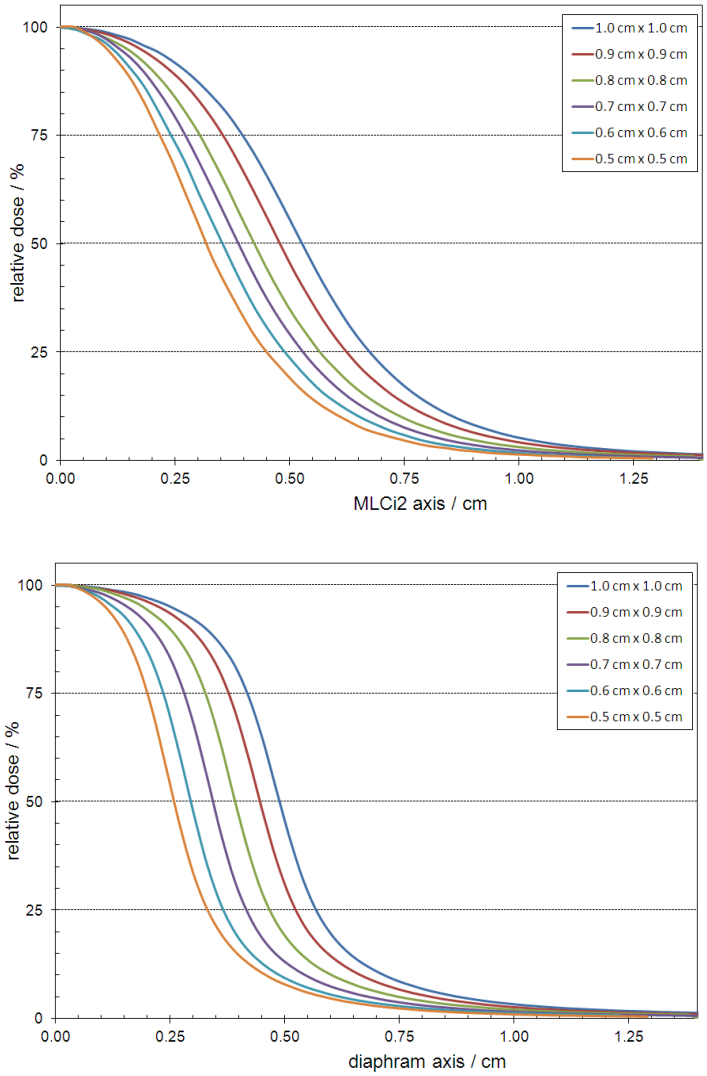

Figure 5.6 Average profile data for the MLCi2 accelerator head measured in water along the leaf-axis (top) and diaphragm axis (bottom).

Reported in Table 5.1 are the mean central axis positions (CAX), mean field sizes (FS) and associated standard experimental uncertainty in field size for the Agility head design. The assumption that the quoted uncertainty is due to collimation and not detector position is substantiated by the very small variability in the CAX. The same data acquired using the MLCi2 is shown in Table 5.2. Clearly the Type-A uncertainty in field size in greater for the MLCi2 than the Agility, with the most notable difference correlating to the smallest field size. Interestingly the uncertainty in field width, as defined by diaphragms, is very nearly constant for both head designs. This may indicate that although the diaphragms themselves have been redesigned the control system has most likely stayed the same. The mean profiles and 80% - 20% penumbral widths for the Agility and MLCi2 are shown in Figures 5.5 and 5.6 and Table 5.3 respectively. Each reveal a striking difference in the penumbral gradient along the MLC and diaphragm axis.

The experimentally determined $k_{Q_{clin},Q_{msr}}^{f_{clin},f_{msr}}$ correction factors calculated according to Equation (5.4) are shown in Table 5.4. The Francescon *et al* [45] PTW T60017 $k_{Q_{clin},Q_{msr}}^{f_{clin},f_{msr}}$ values, derived through Monte Carlo simulation, are also shown in parentheses and agree with our experimental value to within 1.0%. By validating $k_{Q_{clin},Q_{msr}}^{f_{clin},f_{msr}}$ for at least one of the diode detectors studied lends further credence to the experimental procedure of using the FOD first employed by Ralston *et al* [92].

Table 5.3 Penumbral widths calculated using the average profile data shown in Figure 5.5.

Nominal Field Size	80% - 20% Penumbral Width			
	Agility (cm)	Sculpted Diaphragm (cm)	MLCi2 (cm)	Diaphragm (cm)
1.0 cm	0.397	0.262	0.356	0.200
0.9 cm	0.386	0.258	0.345	0.195
0.8 cm	0.376	0.255	0.336	0.188
0.7 cm	0.368	0.253	0.326	0.180
0.6 cm	0.357	0.251	0.315	0.174
0.5 cm	0.346	0.249	0.298	0.172

5.4 Discussion

For the same nominal field size the output ratios measured for the Agility collimator head were greater than that measured for the MLCi2 equipped linac. This result can be attributed to the systematically larger field sizes and penumbral widths measured for the Agility. The dissimilarity in diode detector correction factor could also be attributed to the difference in field size collimated by the two MLC systems, yet the average difference in both field size and penumbral width along the MLC axis was small at 0.04 cm and

therefore would not account for the 2% difference in diode detector correction factors.

Table 5.4 $k_{Q_{clin},Q_{msr}}^{f_{clin},f_{msr}}$ correction factors for each diode using the FOD as the baseline reading.

Nominal Field Size	T60017		SFD		T60016	
	Agility	MLCi2	Agility	MLCi2	Agility	MLCi2
3.0 cm	1.000	1.000	1.000	1.000	1.000	1.000
1.0 cm	0.979	0.973 (0.980)	0.991	0.986	0.958	0.957
0.9 cm	0.978	0.966	0.992	0.978	0.955	0.948
0.8 cm	0.975	0.949	0.988	0.979	0.949	0.950
0.7 cm	0.970	0.955	0.983	0.968	0.943	0.936
0.6 cm	0.967	0.942	0.981	0.941	0.942	0.919
0.5 cm	0.958	0.941 (0.951)	0.968	0.938	0.936	0.920

$k_{Q_{clin},Q_{msr}}^{f_{clin},f_{msr}}$ for each diode detector was less than unity for all field sizes, which results from the well documented over-response of diodes in these types of small field applications. Interestingly, the correction required at the smallest field sizes are approximately 2% greater for MLCi2 compared to that

required for the Agility. The dissimilarity may result from differences in leaf tip transmission or inter-leaf leakage but this could not be substantiated through measurement alone. The MLCi2 system uses flat sided leaves, back-up diaphragms and tilted leaf banks. In contrast, the Agility MLC leaves have in-built defocusing from the source and incorporates essentially no tongue-and-groove. The defocused MLC design provides a very low 0.5% transmission (Cosgrove *et al* [26]) and therefore does not require a back-up diaphragm. This design difference may well result in enough of a spectral change that the correction factors required for the MLCi2 are greater than that required for the Agility. However, this assumption should be substantiated through a detailed Monte Carlo investigation.

Common to both the Agility and MLCi2 is the difference in penumbral gradient along the MLC and diaphragm axes. This difference is a result of the diaphragms being a greater distance away from the Bremsstrahlung target (and closer to the isocenter) than that of the MLC banks. This head geometry results in a sharper penumbra along the axis collimated by the diaphragms. In addition, the midline along the MLC axis projects between the two most centrally located leaf-pairs and therefore contributes to the penumbral broadening. One may well be justified in choosing to measure an additional subset of profile data with a half-leaf positional off-set away from the central axis. Cadman *et al* [16] used profile data measured in just such a manner to obtain a leaf tip characterization used in the commissioning of a treatment planning system.

The increased penumbral width between the Agility and MLCi2 is interesting and thought to be a combined effect that results from the change in leaf geometry, central axis inter-leaf leakage as well as a difference in source width between the two linacs. The leaf height on the MLCi2 and Agility are 82 and 90 mm respectively. Each MLC design will therefore have a different tongue-and-groove type interface and tip radius. It would appear that optimizing the Agility leaf geometry, to maintain an acceptably consistent penumbra across the extended over-travel of 15 cm, results in a slightly wider penumbra for small fields collimated along the beam central axis. The Agility MLC and sculpted diaphragm system was found to provide collimation reproducibility to within ± 0.1 mm as evidenced by the standard deviation in field size reported at a 90% confidence interval (Table 5.1). As such, a clinician may be reassured to use the system in place of stereotactic cones.

It is assumed that using just such an approach would require the steepest dose gradients between an abutting target and critical structure(s). From the data presented in Figure 5.5 and Table 5.3 this would require a collimator rotation. On Elekta linacs the electron source incident on the Bremsstrahlung target is generally accepted as being elliptical (Francescon *et al* [45]) and therefore assuming constant penumbral gradients, as a function of collimator angle, may well be short sighted. To investigate this further a set of small field profile measurements were made at collimator angles of 0, 30, 45, 60 and 90º for nominal square field sizes of 1.0, 0.9, 0.8, 0.7, 0.6 and 0.5 cm. The data was acquired in a similar manner to that reported above yet this time the field size was fixed and the collimator rotated without changing the

field size. At each collimator angle 5 profile measurements were taken along the MLC and diaphragm axis, an average profile was generated and resulting field size calculated at the 50% level.

A small change in field size was measureable as a function of collimator rotation, with the change at each collimator angle nearly constant for all field sizes (see Figure 5.7). At a collimator setting of 0º the diaphragm and MLC are in-plane and x-plane respectively, as the collimator is rotated from 0º to 90º the field sizes in the MLC axis decreased and increased along the diaphragm axis by approximately 0.5 mm. This would indicate the source width is wider x-plane than in-plane and is consistent with the source parameterization of Francescon *et al* [45] at $FWHM_x$ = 2.0 mm and $FWHM_y$ = 0.9 mm. Although the field size is not constant as a function of collimator angle the clinical use of the system for stereotactic applications would not generally be compromised. Subsequent work may be required to investigate if the field size dependence on collimator angle should be included in SRS treatment planning and how to incorporate this data into the commissioning of a treatment planning system. Data such as this clearly shows that robust experimental characterization of a collimation system for use in SRS applications should not solely focus on reporting conformity index type metrics derived from treatment planning studies. In fact, dosimetric characterization should be considered as a measurement based activity which reports experimental values to within an associated uncertainty.

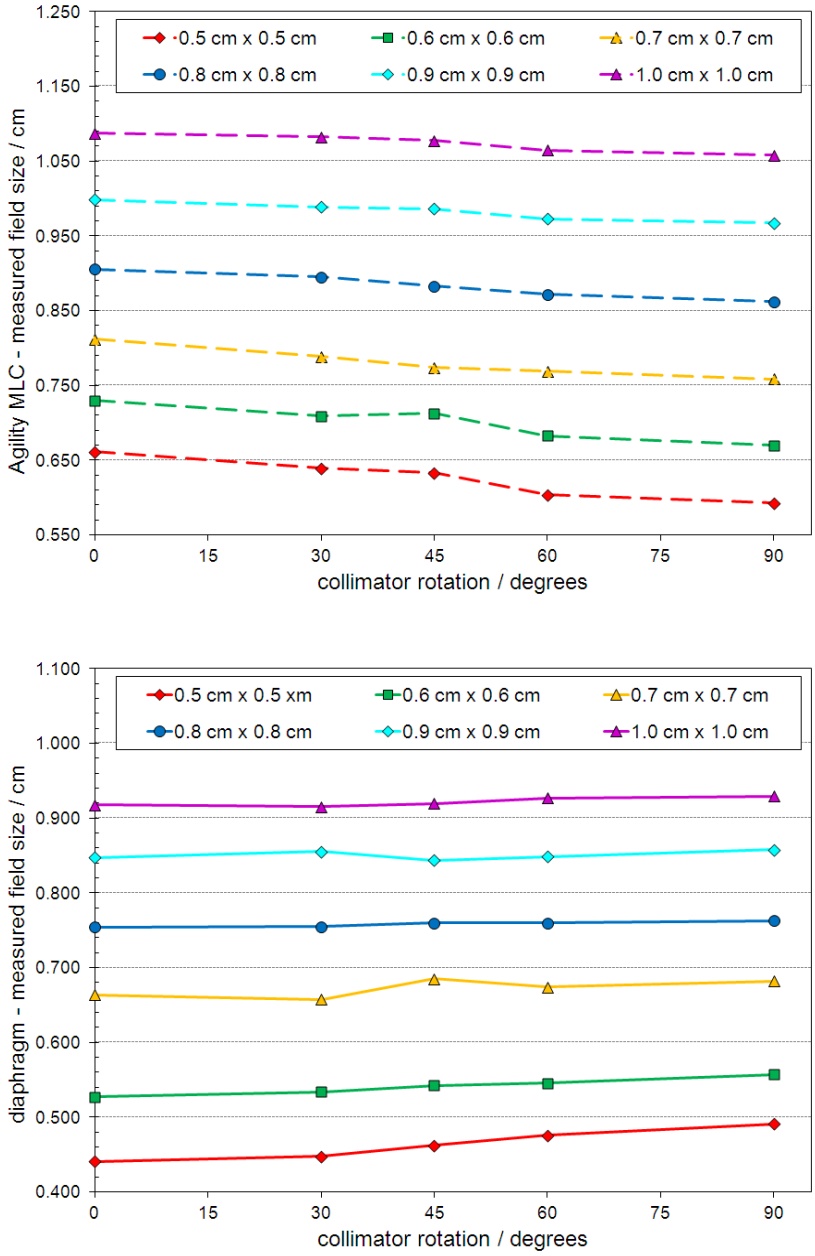

Figure 5.7 Shown above are the measured field sizes along the MLC axis (top) and diaphragm axis (bottom) as a function of collimator rotation.

Pantelis *et al* [88,89] have presented a unique experimental procedure for deriving $k_{Q_{clin},Q_{msr}}^{f_{clin},f_{msr}}$ correction factors for various diode detectors. The method uses an error weighted average of Alanine pellet, thermoluminescent dosimeter (TLD), Gafchromic EBT film and normoxic gel relative output

measurements to derive a water equivalent output factor that can then be used to correct for the well known diode over-response in small fields. Given the recent work of Scott *et al* [100] one may be hesitant to include TLD (ρ = 2.64 g·cm^{-3}) data in just such a methodology. In fact, Scott *et al* clearly shows that dosimeters for use in small fields should be water density equivalent and therefore the scintillator (ρ = 1.032 g·cm^{-3}) based measurements presented here could be considered a slightly more robust methodology. It could also be argued that using a well developed scintillator based dosimeter for small field relative dosimetry is desirable due solely to the simplicity of implementation.

5.5 Conclusion

The relative output, profile widths and associated uncertainties were all found to differ between the two MLC systems investigated, as were the field size specific diode detector replacement correction factors. The data also showed that the Agility 160-leaf MLC performs to a tighter positional tolerance than the MLCi2.

Chapter 6
A methodological approach to reporting corrected small field relative outputs

6.1 Introduction

The International Electrotechnical Commission (IEC) recommends using the distance intercepted by a given isodose curve (50% level) on a plane perpendicular to the beam axis, at a stated fixed distance from the source (isocenter), to define the dosimetric field size [56]. Often in clinical practice the definition of field size is more loosely taken to mean the light field projection at a fixed distance from the source. In the somewhat dated ICRU Report 24 [55] the light field projection is defined as the geometric field size. For field sizes large enough to ensure no source occlusion and charged particle equilibrium (CPE) the geometric field size may provide an accurate representation of the dosimetric field size, at least to within a given clinical tolerance. However, Das *et al* [33] have reported that for field sizes that do not satisfy the CPE or occlusion criteria the dosimetric field size will be greater than the geometric field size and therefore the traditional close agreement between field size definitions breaks down.

Experimental small field dosimetry can be challenging due to the lack of lateral charged particle equilibrium, spectral changes as a function of field size, detector choice and subsequent perturbations of the charged particle

fluence [7,17,24,33]. Alfonso *et al* [1] have presented a well thought out dosimetry formalism for reporting corrected relative output factors for small and non-standard fields. Although the formalism establishes a framework for correcting small field relative output measurements it could be argued that the reporting, and application, of $k_{Q_{clin},Q_{msr}}^{f_{clin},f_{msr}}$ as a function of field size is still somewhat ambiguous.

Commercial diode detectors have been shown to be a reasonably good choice for small field dosimetry applications, yet care must be taken when selecting between shielded (photon) and unshielded (electron and stereotactic) diodes. In general, the correction factors required for shielded diodes are approximately twice that required for the unshielded diodes for the same irradiation conditions. An experimental procedure for deriving $k_{Q_{clin},Q_{msr}}^{f_{clin},f_{msr}}$ for various diode detectors has been presented by Pantelis *et al* [88,89]. The method makes use of an error weighted average of Alanine pellet, thermoluminescent dosimeter (TLD), Gafchromic EBT film and normoxic gel measured relative outputs to derive a water equivalent output factor. The experimental output factor can then be used to correct for the well documented diode over-response in small fields. Ralston *et al* [92] used an air-core fibre optic scintillation dosimeter (FOD) for small field relative output dosimetry and showed the FOD can be used to experimentally determine $k_{Q_{clin},Q_{msr}}^{f_{clin},f_{msr}}$ for other detector types. The results presented in Chapter 5 show that a FOD can be used experimentally determine $k_{Q_{clin},Q_{msr}}^{f_{clin},f_{msr}}$ for a set of diodes and further characterization of small fields collimated with

a new 160-leaf MLC was conducted. The recommendation would be that output ratios and field sizes be measured concurrently as well as the standard experimental uncertainty be quoted when reporting experimental results.

Monte Carlo simulation has proven to be a powerful tool in overcoming the challenges inherent to small field dosimetry. Scott *et al* [100] has shown that the ratio of dose-to-water to dose-to-detector-in-water varies significantly as a function of field size. For small field sizes this ratio correlates with the mass density of the detector material relative to that of water. The authors also show that all water dose profiles are very similar to profiles simulated with a small isolated silicon volume in water (also see Francescon *et al* [45]).

Regardless of the dosimeter studied, the relative output and corresponding correction factors appear to have been presented as a function of the nominal field size and not the dosimetric field size. The viability of applying small field, central axis, relative output correction factors to clinically measured data requires standardization in measurement. In addition to experimental standardization, a field size metric which can be used to appropriately correlate relative output to the measured dosimetric field size is essential. The suitability of applying published $k_{Q_{clin},Q_{msr}}^{f_{clin},f_{msr}}$ correction factors across a population of linacs is also not apparent from the literature nor is it clear how the corrections should be applied to clinical data reported as a function of the measured dosimetric field size. This becomes problematic at

both the clinical level and in the development of a small field dosimetry CoP. As such, each aspect will be addressed in the work that follows.

6.2 Methods

6.2.1 Effective field size for use in small field dosimetry

For small fields collimated with jaws and/or MLCs there can be a difference between the geometric field size and nominal field size as set on the linac console. The difference can be due to collimator calibration and the positional accuracy of the collimation system itself. Add to this the inherent complication of the dosimetric field size being greater than the geometric field size and the requirements for a systematic framework for reporting and interpreting small field dosimetric values becomes clear. As such, a small field metric which can be used to represent the dosimetric field size would be of value. A number of approaches to this are possible but given the magnitude of the dimensional and scatter component changes which need to be taken into account an effective small field size is suggested as follows,

$$FS_{eff} = \sqrt{A \cdot B}\,, \tag{6.1}$$

where A and B correspond to the in-plane and x-plane dosimetric field

widths defined as the FWHM at the 50% isodose level. Moreover, one can define an equivalent field area such that,

$$FA_{equ} = A \cdot B. \tag{6.2}$$

Defining FS_{eff} and FA_{equ} provides a simple yet robust methodological framework for comparing small field dosimetric quantities across a population of linacs with different collimation systems (jaws, MLCs and cones, where the FA_{equ} of the latter can be represented by the actual measured field area and the FS_{eff} as the square root of this). We first explore the use of FS_{eff} for small, nominally square, fields and leave the viability of using FA_{equ} for comparison between cone, jaw and MLC collimated small fields for future work.

6.2.2 Experimental measurements

Small field 6 MV relative output measurements were made using two different PTW T60017 unshielded diodes on five Varian iX linacs located at three different institutions (See Table 6.1 for details). Detector specific output ratios ($OR_{det}^{f_{clin}}$) were calculated with respect to a square, jaw collimated, field size of side 3.0 cm for nominal square, jaw collimated, field sizes of side 1.0, 0.9, 0.8, 0.7, 0.6 and 0.5 cm. Measurements were made at a depth of 5.0 cm with the long axis of the diode detector placed parallel to the beam axis such

that the active volume was positioned at isocenter. Positional fine tuning was performed to ensure the active volume of the detector was located at the radiation isocenter and not just centred on the light field. Following this method ensured the detector positional uncertainty was limited only by accuracy of the water tank system quoted by the manufacturer at ± 0.1 mm.

Table 6.1 Linear accelerator and detector details.

Label	Institution	Varian iX	PTW T60017 Electron Diode
SCC-0	Saskatoon Cancer Centre	S/N 2311	S/N 000345
SCC-1		S/N 5141	
SCC-2		S/N 1085	
QUT-1	Premion, Wesley Centre	S/N 3561	S/N 000627
QUT-2	Premion, Chermside Centre	S/N 3850	

The measurements were repeated three times with the water phantom, detector position and collimation reset between each experimental session. During each experimental session five central axis output readings and five in-plane and x-plane profile measurements were made at each field size. The mean output ratio and field widths were calculated across the three experimental sessions as were the standard experimental errors for each.

FS_{eff} was calculated using the dosimetric field widths along each axis and $OR_{det}^{f_{clin}}$ values reported as a function of both the nominal and effective field sizes.

6.2.3 Monte Carlo simulations

A previously published BEAMnrc model of a 6 MV Varian iX linear accelerator head was used throughout this study [6]. The baseline electron source parameterization was a 6.2 MeV mono-energetic Gaussian with a circularly symmetric FWHM = 0.110 cm [28,29]. Simulated machine output per monitor unit was modelled using the method of Popescu *et al* [91] and azimuthal particle redistribution used to reduce latent phase space uncertainty [14].

DOSRZnrc simulations were run with the previously benchmarked T60017 diode detector model [28,29] such that the statistical dose uncertainty scored to the active volume was approximately ± 0.5%. The EGSnrc transport parameters ECUT, PCUT and ESTEP were set to 0.521 MeV, 0.01 MeV and 0.25 respectively. The EXACT boundary crossing algorithm was used in combination with the PRESTA-II condensed history electron step algorithm (ESAVEIN = 2.0 MeV) and the photon cross-section enhancement variance reduction technique. Phase space data for jaw collimated geometric field sizes of side 0.40, 0.45, 0.50, 0.55, 0.60, 0.65, 0.70, 0.75, 0.80, 0.85, 0.90, 0.95, 1.0 and 3.0 were used as DOSRZnrc input. Simulated output ratios were calculated for each field size as follows,

$$OR_{det_{MC}}^{f_{clin}} = \left(\frac{D_{det_{MC}}^{f_{clin}}}{D_{det_{MC}}^{f_{msr}}} \right) \cdot \left(\frac{D_{monitor_{MC}}^{f_{msr}}}{D_{monitor_{MC}}^{f_{clin}}} \right), \qquad (6.3)$$

where $D_{det_{MC}}^{f_{clin}}$, $D_{det_{MC}}^{f_{msr}}$, $D_{monitor_{MC}}^{f_{clin}}$ and $D_{monitor_{MC}}^{f_{msr}}$ represent the dose per incident particle scored to the active volume of the detector model and linac monitor unit chamber for the f_{clin} and f_{msr} simulations respectively.

DOSXYZnrc simulations were run using the same phase space data used in the DOSRZnrc simulations. The history number was set to give a statistical uncertainty less than ± 0.5% within a voxel dimension of 0.05 cm x 0.05 cm x 0.25 cm. The in-plane and x-plane FWHMs at the 50% level were extracted from the data and the resultant dosimetric field widths plotted as a function of the geometric field widths. The sensitivity of FS_{eff} to variations in electron energy and FWHM were investigated using two data sets. The first set of data was calculated for an electron energy fixed at 6.2 MeV with the Gaussian spatial distribution varied as follows: FWHM = 0.100, 0.110, and 0.120 cm. The second set of data was for electron energies at 5.8, 6.0 and 6.2 MeV with the spatial distribution fixed at a FWHM = 0.110 cm. Once again the dosimetric field widths were extracted from the data and plotted as a function of geometric field widths. For each source parameter combination $OR_{det_{MC}}^{f_{clin}}$ was plotted as a function of both the nominal and effective field size and the results compared to the experimental data.

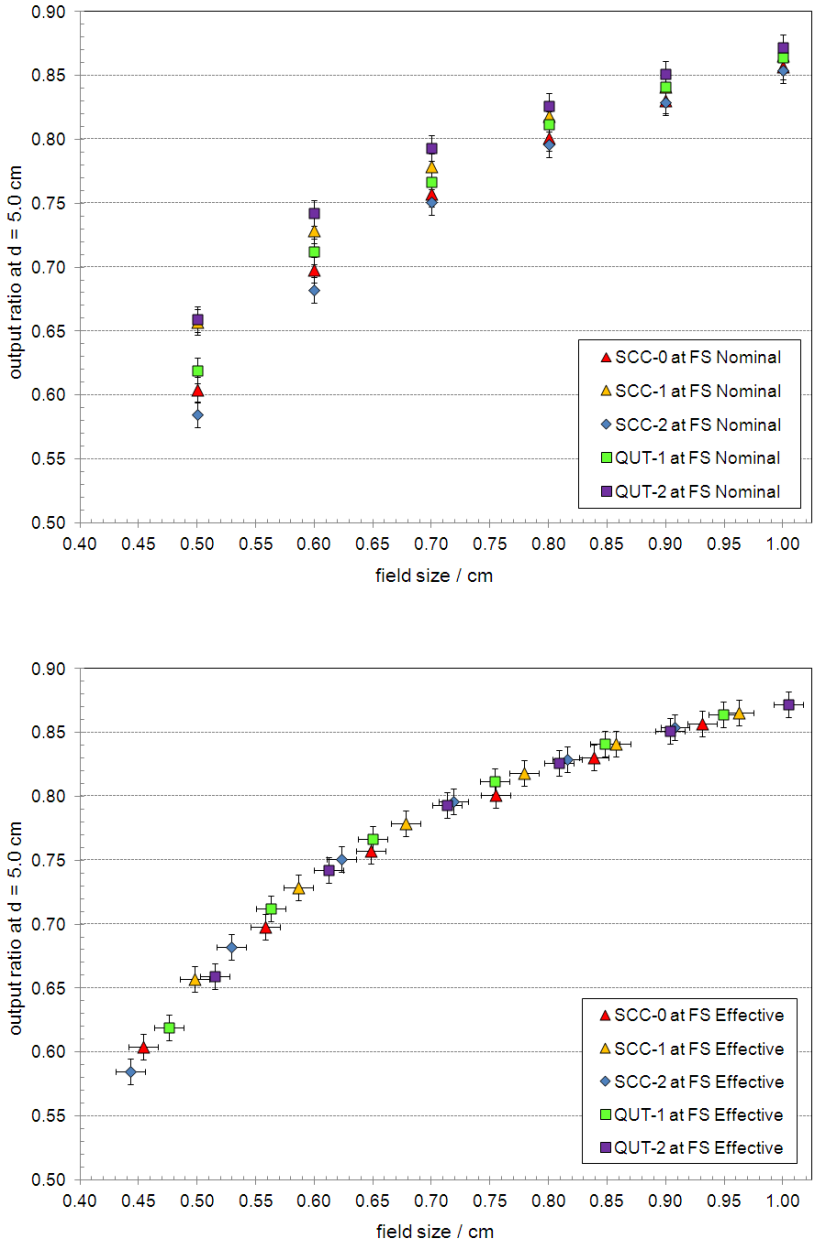

Figure 6.1 Measured $OR_{det}^{f_{clin}}$ data plotted as a function of the nominal (top) and effective (bottom) field sizes.

6.2.4 Interpreting and applying $k_{Q_{clin},Q_{msr}}^{f_{clin},f_{msr}}$

The PTW T60017 diode $k_{Q_{clin},Q_{msr}}^{f_{clin},f_{msr}}$ factors presented in Chapter 3 were used to correct the experimental $OR_{det}^{f_{clin}}$ data in a manner consistent with the Alfonso

et al formalism. The $k_{Q_{clin},Q_{msr}}^{f_{clin},f_{msr}}$ data was presented at the geometric field sizes and therefore some question still remained as to the appropriateness of applying the corrections (or similar corrections) to $OR_{det}^{f_{clin}}$ data reported at FS_{eff}. The experimental $OR_{det}^{f_{clin}}$ data was corrected using the $k_{Q_{clin},Q_{msr}}^{f_{clin},f_{msr}}$ as presented at the geometric field sizes and with $k_{Q_{clin},Q_{msr}}^{f_{clin},f_{msr}}$ reassigned to the effective field sizes calculated from the DOSXYZnrc simulations. In all cases, linear interpolation was used to assign $k_{Q_{clin},Q_{msr}}^{f_{clin},f_{msr}}$ to the corresponding experimental FS_{eff}. It should be noted that an additional correction factor was calculated for the square field of side 0.40 cm and the entire $k_{Q_{clin},Q_{msr}}^{f_{clin},f_{msr}}$ data set renormalized to a reference field size of side 3.0 cm.

6.3 Results

Figure 6.1 shows the measured $OR_{det}^{f_{clin}}$ data plotted as a function of the nominal field size (as set on the linac console) and the effective field size calculated using the measured in-plane and x-plane dosimetric field widths. When the $OR_{det}^{f_{clin}}$ data is plotted as a function of the nominal field size there appears to be a significant difference in the relative output across the linac population, which could be incorrectly interpreted as being a real difference in the electron source width incident on the Bremsstrahlung target. However, when the same $OR_{det}^{f_{clin}}$ data is plotted as a function of FS_{eff} there is no discernible difference in relative output across the population of linacs. The

inference being that the linear accelerators included in this study have electron source distributions that are very nearly indistinguishable.

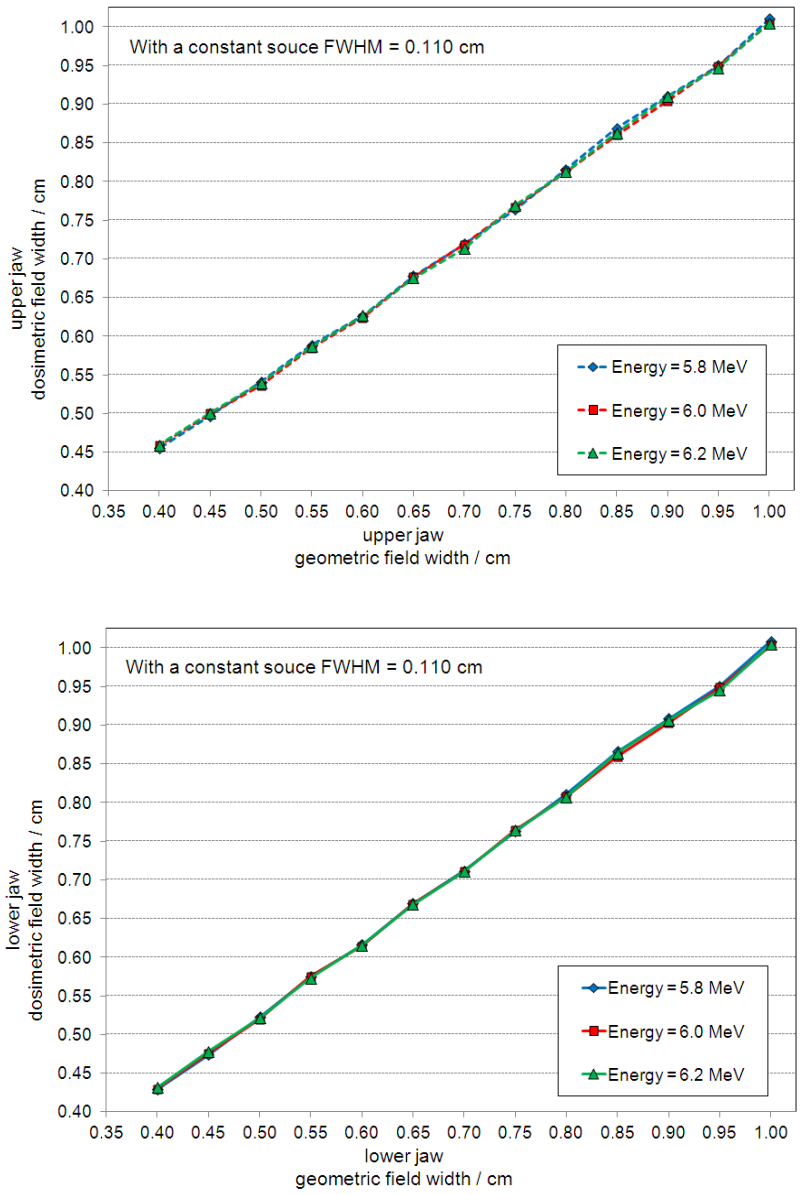

Figure 6.2 Geometric field widths plotted as a function of the dosimetric field width for the upper (top) and lower (bottom) jaws for a constant source FWHM.

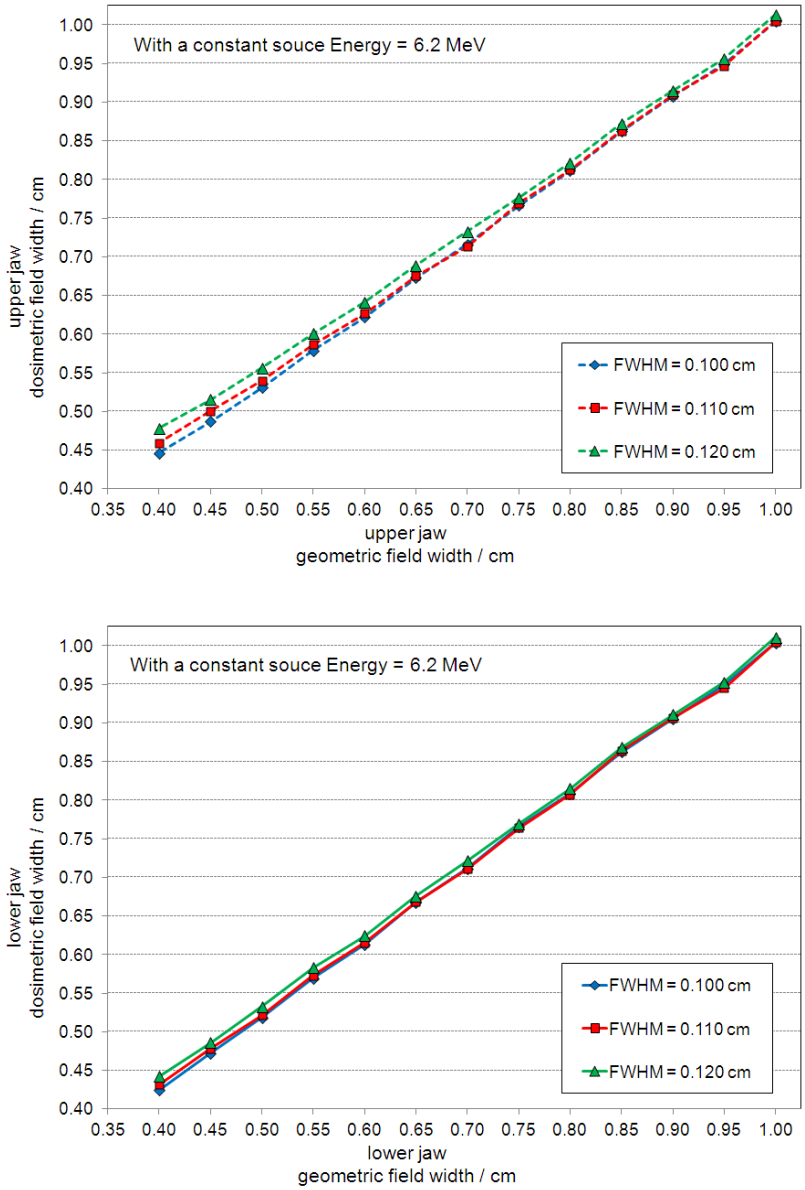

Figure 6.3 Geometric field widths plotted as a function of the dosimetric field width for the upper (top) and lower (bottom) jaws for a constant source energy.

Figures 6.2 and 6.3 show the DOSXYZnrc simulation data that relates the dosimetric field width to the corresponding geometric field width for the upper and lower jaws. These data reveal a number of interesting

characteristics: (1) dosimetric field widths are greater than the geometric field widths for field sizes less than approximately 0.8 cm x 0.8 cm, (2) the effect is greater along the axis collimated by the upper jaw than that collimated by the lower jaw and (3) the effect is independent of source energy but increases as a function of increased source width. The dosimetric field width data can be thought of as measured data from a perfect collimator jaw suffering from no positional error or uncertainty and therefore can be used to elicit the difference between the geometric and dosimetric field widths for this particular accelerator head.

Shown in Figures 6.4 and 6.5 are the $OR_{det_{MC}}^{f_{clin}}$ data plotted as a function of the geometric and effective field sizes respectively. Each graph includes the experimental $OR_{det}^{f_{clin}}$ data plotted as a function of the measured effective field sizes (see Figure 6.1). The $OR_{det_{MC}}^{f_{clin}}$ data simulated using a source FWHM = 0.120 cm, and plotted as a function of the geometric field size, agrees best with the experimental data. However, $OR_{det_{MC}}^{f_{clin}}$ simulated using a source FWHM = 0.100 cm is clearly in better agreement if plotted as a function of the effective field size. In both instances the agreement between the experimental and simulated data is reasonable at a FWHM = 0.110 cm.

The data in Figure 6.6 shows the relative output plotted as a function of the measured effective field size corrected using $k_{Q_{clin},Q_{msr}}^{f_{clin},f_{msr}}$ values at the geometric field size and the same $k_{Q_{clin},Q_{msr}}^{f_{clin},f_{msr}}$ values reassigned to the

associated effective field size. Clearly using $k_{Q_{clin},Q_{msr}}^{f_{clin},f_{msr}}$ at the nominal and effective field sizes produce output factors that are not identical but differ by much less than the reported experimental and/or Monte Carlo statistical uncertainties. The more important criteria for using the proposed methodology is to characterize, correct and report relative output as a function of the effective field size and not the nominal.

6.4 Discussion

The measured small field relative output data reported as a function of the nominal field size are clearly different across the accelerator population (see Tables 6.2 and 6.3). However, using the effective field size for reporting showed that the actual output ratios were consistent across the accelerator population. This indicates that Varian iX accelerators are generally well matched and that any major discrepancies in the literature may be attributed to reporting relative output as a function of the nominal field size. Understanding the differences between the nominal, geometric and dosimetric field sizes is critical and the implications, as they relate to interpreting small field dosimetric data, should not be discounted. For specialized stereotactic collimators, such as cones or micro-MLCs, the difference between the dosimetric and geometric field widths will be less than that for upstream jaw collimators. This alone highlights the importance of establishing a mechanism which facilitates the presentation of relative output data as a function of the measured equivalent field area.

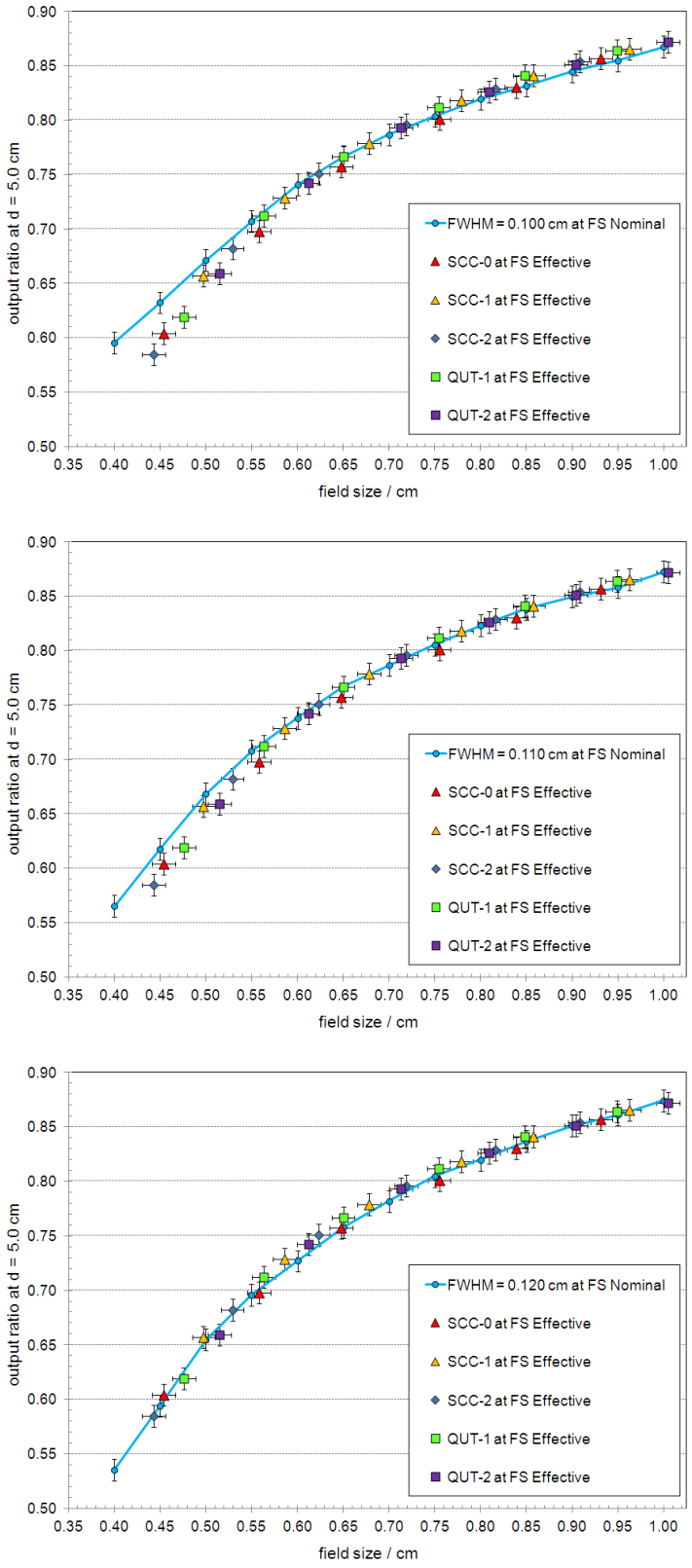

Figure 6.4 Simulated $OR_{det}^{f_{clin}}$ data (solid line) plotted as a function of the nominal field size.

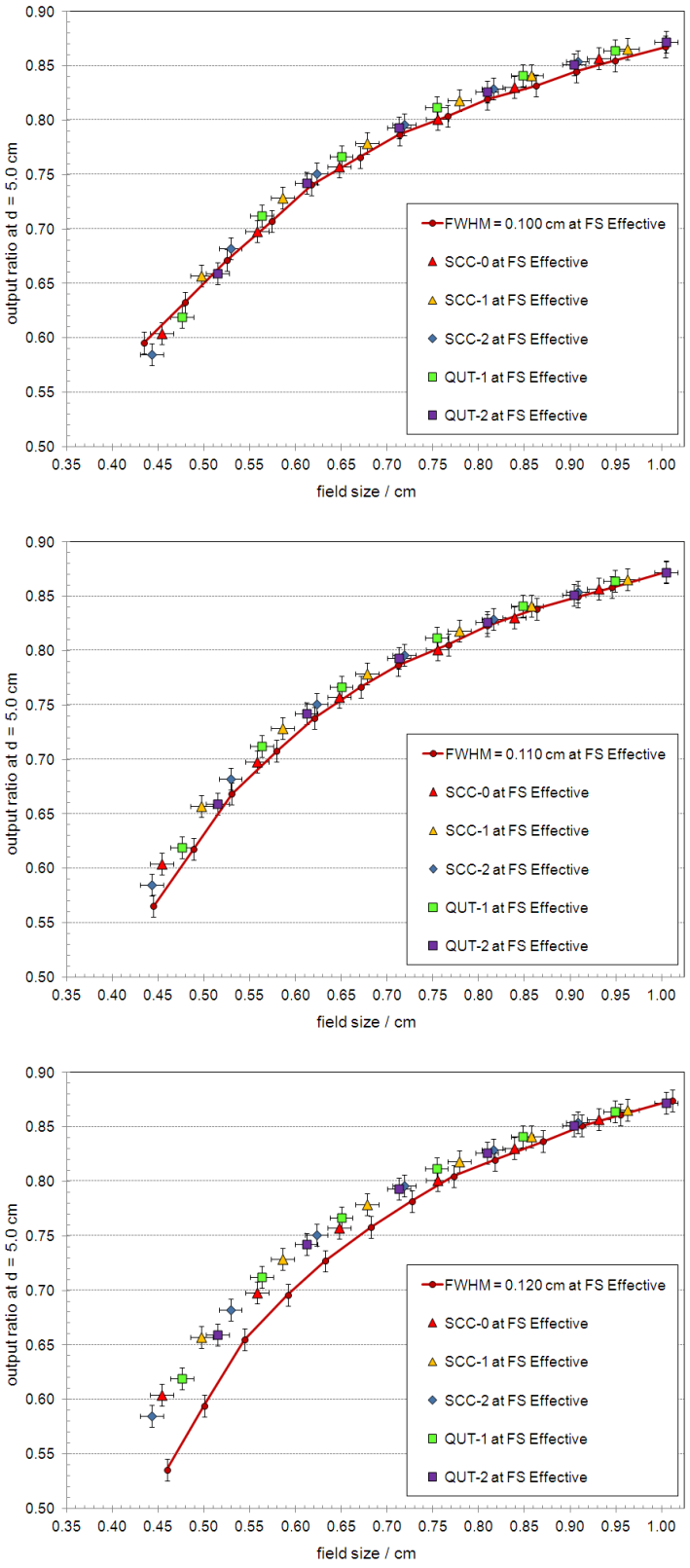

Figure 6.5 Simulated $OR_{det}^{f_{clin}}$ data (solid line) plotted as a function of the effective field size.

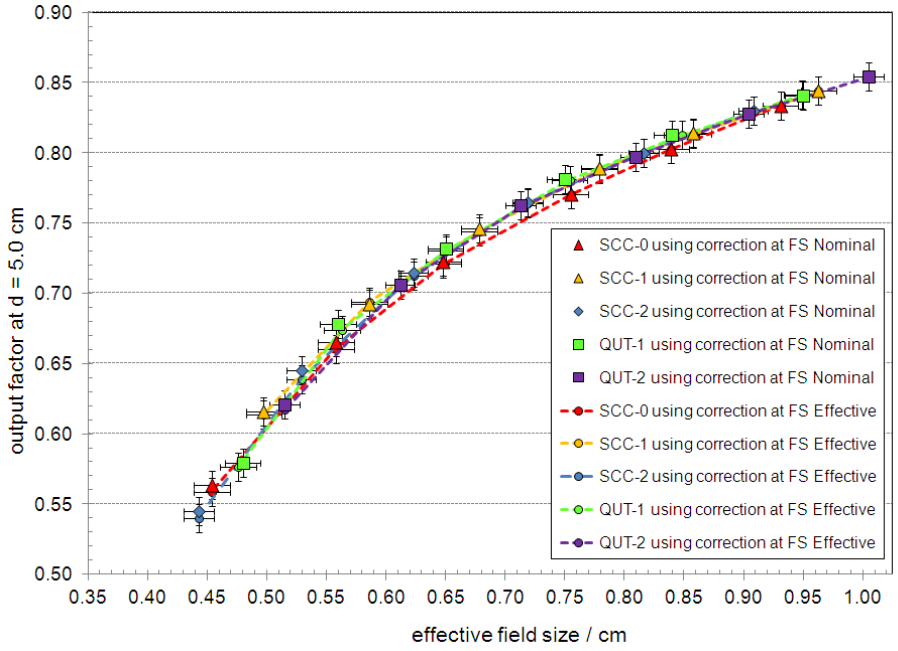

Figure 6.6 Corrected relative output data plotted as a function of the measured effective field size.

Reporting measured relative output and dosimetric field widths concurrently is comprehensive but somewhat cumbersome. What has been shown here is that using FS_{eff} as a small field metric relieves much of the ambiguity in reporting and simplifies the measured dosimetric field widths into one representative value. In addition, adopting a standard experimental methodology that includes reporting uncertainties in both the effective field size and measured output ratios is vital and consistent with the importance given to the expression of uncertainties documented in the IAEA dosimetry code of practice [54].

Table 6.2 Listed here are the nominal, measured and effective field sizes for linacs SCC-1 and -2.

SCC-1	Dosimetric Field Widths (cm)		Effective Field Size (cm)	Output Ratio
Nominal Field Size (cm)	In-plane	X-plane		
1.0	0.951 ± 0.001	0.975 ± 0.006	0.963 ± 0.007	0.866 ± 0.11%
0.9	0.857 ± 0.007	0.858 ± 0.059	0.858 ± 0.059	0.841 ± 0.92%
0.8	0.766 ± 0.013	0.792 ± 0.013	0.779 ± 0.019	0.818 ± 0.02%
0.7	0.659 ± 0.007	0.698 ± 0.005	0.678 ± 0.009	0.779 ± 0.54%
0.6	0.570 ± 0.008	0.603 ± 0.003	0.586 ± 0.008	0.729 ± 0.36%
0.5	0.494 ± 0.007	0.502 ± 0.008	0.498 ± 0.010	0.657 ± 0.18%

SCC-2	Dosimetric Field Widths (cm)		Effective Field Size (cm)	Output Ratio
Nominal Field Size (cm)	In-plane	X-plane		
1.0	0.882 ± 0.001	0.935 ± 0.013	0.908 ± 0.013	0.854 ± 0.13%
0.9	0.793 ± 0.007	0.840 ± 0.008	0.816 ± 0.011	0.829 ± 0.31%
0.8	0.700 ± 0.003	0.737 ± 0.001	0.719 ± 0.003	0.796 ± 0.14%
0.7	0.609 ± 0.005	0.638 ± 0.015	0.623 ± 0.016	0.751 ± 0.61%
0.6	0.511 ± 0.005	0.547 ± 0.012	0.529 ± 0.013	0.682 ± 1.22%
0.5	0.443 ± 0.006	0.452 ± 0.027	0.443 ± 0.028	0.585 ± 1.46%

The Monte Carlo simulations clearly show that the dosimetric field size is larger than the geometric field size for small fields (as previously reported by Das *et al* [33] and Aspradakis *et al* [5]). In all cases the dosimetric field width defined by the upper jaws was larger than that defined by the lower jaws.

Table 6.3 Listed here are the nominal, measured and effective field sizes for linacs QUT-1 and -2.

QUT-1	Dosimetric Field Widths (cm)		Effective Field Size (cm)	Output Ratio
Nominal Field Size (cm)	In-plane	X-plane		
1.0	0.933 ± 0.002	0.963 ± 0.003	0.948 ± 0.004	0.864 ± 0.20%
0.9	0.833 ± 0.002	0.868 ± 0.010	0.850 ± 0.010	0.841 ± 0.38%
0.8	0.745 ± 0.002	0.766 ± 0.015	0.755 ± 0.015	0.812 ± 0.29%
0.7	0.644 ± 0.000	0.649 ± 0.003	0.651 ± 0.003	0.767 ± 0.26%
0.6	0.559 ± 0.007	0.571 ± 0.010	0.565 ± 0.013	0.713 ± 0.42%
0.5	0.471 ± 0.013	0.482 ± 0.012	0.477 ± 0.018	0.619 ± 0.95%

QUT-2	Dosimetric Field Widths (cm)		Effective Field Size (cm)	Output Ratio
Nominal Field Size (cm)	In-plane	X-plane		
1.0	0.963 ± 0.016	1.050 ± 0.012	1.005 ± 0.020	0.872 ± 0.05%
0.9	0.870 ± 0.002	0.940 ± 0.001	0.904 ± 0.002	0.851 ± 0.23%
0.8	0.768 ± 0.027	0.854 ± 0.004	0.810 ± 0.027	0.826 ± 0.49%
0.7	0.683 ± 0.002	0.744 ± 0.016	0.713 ± 0.016	0.793 ± 0.21%
0.6	0.583 ± 0.000	0.643 ± 0.006	0.612 ± 0.006	0.743 ± 0.23%
0.5	0.488 ± 0.012	0.544 ± 0.007	0.515 ± 0.014	0.659 ± 0.36%

The upper jaws are closer to the source when compared to the lower jaws and therefore require a smaller physical separation to collimate the same geometric field width. The result is greater source occlusion across the upper jaw and therefore an increased effective field size. In short, dosimetric field widths increase as a function of increased source occlusion. For the

same reason the dosimetric field widths increase as a function of electron spot size increase. The effective field size should therefore be used when tuning the focal spot size of a linear accelerator Monte Carlo model. As evidenced in Figures 6.3 and 6.4, using the geometric field size may result in an incorrect spot size being determined.

There was a negligible difference in the output factors when $k_{Q_{clin},Q_{msr}}^{f_{clin},f_{msr}}$ was applied using the geometric field size or the effective field size. This is consistent with the work of Scott *et al* [100] which showed that a 1.0 mm field size difference results in a 1.0% difference in $k_{Q_{clin},Q_{msr}}^{f_{clin},f_{msr}}$. However, it is recommended that the effective field size be used when assigning $k_{Q_{clin},Q_{msr}}^{f_{clin},f_{msr}}$, as it provides consistency within the proposed methodology and standardizes the application across a population of linacs.

Presenting small field relative output data as a function of the effective field size, as defined is this work, can be well justified when one considers the phantom and head scatter factor characteristics of small fields. McKerracher and Thwaites [83] show that for square field sizes of side less than 4.0 cm measured phantom scatter factors are independent of collimation and linac design and dependent only on measurement depth and the beam area irradiated. It is therefore quite reasonable to argue for the use of FA_{equ} in comparing small field dosimetric quantities across multiple linacs or different collimation systems (jaws, MLCs and cones).

Head scatter factors for rectangular field sizes have been shown to be dependent on the collimator exchange effect [105]. However, as Zhu *et al* [114] note, this effect is negligible at field sizes of side less than 2.0 cm, where source occlusion becomes the dominant effect. Reporting relative output as a function of the FS_{eff}, which one will recall is calculated from the measured dosimetric field widths, clearly takes into account differences in source occlusion for millimetre scale changes in field size. Naturally there may be limitations in further application of the concepts presented here and in no way should one apply FA_{equ} or FS_{eff} without rigorous experimental validation.

6.5 Conclusion

For field sizes larger than approximately 1.0 cm the dosimetric and effective field sizes are equal and can generally be taken to be the same as the geometric field sizes. Therefore using an effective field size for small field dosimetry is consistent with current practice and can easily be accepted as a working definition for small field sizes. It has been shown that adopting this field size metric and the measurement methodology outlined in this portion of the study can provide consistency for small field dosimetry across a population of linear accelerators. However, there could be differences between accelerator designs with greater source occlusion due to a larger focal spot size, a collimation system closer to the source, or simply a smaller field size.

Chapter 7
Conclusion

7.1 General conclusions, impact and novel contributions

General conclusions will be summarized in the context of the principle research question, *"What are the requirements for accurate small field relative dosimetry?"*. The impact and novel contributions of the work will also be addressed.

Chapters 2 through 6 were each published as standalone papers [27,28,29,30,31] and therefore the impact and novel contributions of each Chapter will be assessed within the context of the peer-reviewed literature at the time of publication. The current "state-of-affairs" will also be provided through an assessment of the most recent publications related to the work presented here and potential directions for future work explored.

7.1.1 Chapter 2 - Small field output ratio analysis

The work in Chapter 2 clearly shows there are differences in the experimental small field relative output measured using shielded and unshielded diodes. Unlike other studies that present relative output data measured using various detector types on a single treatment machine, the

relative output data presented here was measured on two different linear accelerator head designs using only diode detectors. Not only were relative output data presented but a full experimental uncertainty analysis was performed. Measuring and reporting relative output might not be considered overly novel but the subtlety of reporting relative output ratios as opposed to relative output factors marks a clear change in practice.

Output factors are by definition the field size specific relative output ratios in water [90]. Output factors can be considered equivalent [50] to the ratio of ionization chamber readings measured under Bragg-Gray conditions, which implies the following would be required: (1) the field size must be large enough to ensure lateral charged particle equilibrium across the entire chamber, (2) that the ionization in the cavity can be directly related to the absorbed dose in the chamber wall and (3) the wall thickness must have a dimension great enough to ensure that all electrons that cross the cavity arise from within the wall and not the medium [58]. This is clearly not the case for small field relative output measurements and therefore investigators reporting measured small field output factors are in error (see [36] as an example). Only once a measured output ratio has been corrected using $k_{Q_{clin},Q_{msr}}^{f_{clin},f_{msr}}$ can the data be referred to as an output factor – which is $\Omega_{Q_{clin},Q_{msr}}^{f_{clin},f_{msr}}$ in the Alfonso *et al* formalism.

Understanding the difference between measured small field output ratios and the associated small field output factors has become clear for many of

the active researchers in the area of small field dosimetry. However, the subtleties are not well understood by the community as a whole, and yet are required for the accurate reporting of relative output in small field applications such as SRS and/or SBRT. As the community evaluates the clinical implementation of the proposed small field dosimetry formalism the impact of publishing experimental small field relative output ratios as opposed to relative output factors will become even more clear. With the recent reported errors made in small field dosimetry the clinical importance given to just such a detail may become ever more important.

The differences in the associated delivery precision as a function of linac head design, collimation and control system were also assessed in the work presented in Chapter 2. Arguing that these types of measurements are a requirement for the accurate implementation of the proposed small field dosimetry formalism could be debated. However, an in-depth dosimetric characterization that includes quantifying the variability in small field relative output as a function of collimator positional reproducibility, or the influence of leaf offset adjustment away from the commissioning baseline only adds to the understanding of the delivery system and therefore should be included as part of the experimental work performed prior to small field delivery applications such as SRS and/or SBRT.

The work presented in Chapter 2 demonstrates that the interpretation of experimental small field data can be ambiguous unless there is a clear understanding regarding measurement technique, data interpretation,

experimental uncertainty characterization and the delivery system limits. Therefore each aspect of the experimental process can be thought of as "*a requirement for accurate small field relative dosimetry*."

7.1.2 Chapter 3 - Implementing a Monte Carlo based small field dosimetry formalism

There were a number of general conclusions that came out of working through the proposed small field dosimetry formalism using Monte Carlo simulation methods: (1) Monte Carlo calculated small field detector-specific output ratios and in-water output factors are very sensitive to the simulated source parameterization, (2) for a Varian iX accelerator head the backscattered dose to the monitor chamber should be included in simulated output ratio calculations (a conclusion that is likely to apply also to other linac designs and which should always be considered), (3) at the smallest field sizes (down to 0.5 cm field side) the corrections required for shielded diode detector designs are nearly twice that required for unshielded diode designs and (4) the reported detector-specific correction factors should be applied to experimental small field $OR_{det}^{f_{clin}}$ data that are consistent with those of the associated simulation data.

At the time of publication there were still significant questions and debate regarding the methodology required to implement the proposed small field dosimetry formalism. The early work of Francescon *et al* [44], Scott *el at* [98,99] and Eklund and Ahnesjö [40,41,42] had clearly set the stage for the

use of Monte Carlo simulation in small field dosimetry, yet there was no consensus within the community regarding which of the previously published results were correct. Francescon *et al* had only investigated the three smallest circular collimators available with the Cyberknife radiosurgery system at a nominal 6 MV beam energy. Scott *et al* had made unsubstantiated simplifications in diode detector modelling and used a nominal 15 MV beam energy throughout their work. Add to this the results of Eklund and Ahnesjö [42], that were inconsistent with the other work, and indeed there were still significant questions regarding the use of Monte Carlo simulation in small field dosimetry.

The work in Chapter 3 was published at the same time the work of Francescon *et al* [45] appeared in the literature. Both papers outlined very similar benchmarking processes for use in small field applications. The estimated experimental uncertainty quoted by Francescon *et al* was ±0.75% (1σ) and is consistent with our general experimental uncertainty findings of approximately ±1.25% (2σ). However, the uncertainties on the correction factors quoted by Francescon *et al* at less than ±0.7% do appear to have been calculated wrongly and should have been reported for the diode detectors as being less than ±1.0%. The authors are also incorrect in their ubiquitous use of the term output factor to describe the ratio of detector readings.

In all cases the $k_{Q_{clin},Q_{msr}}^{f_{clin},f_{msr}}$ for diode detectors was shown to be less than unity for small fields. This result implies that at the smallest of field sizes the

relative output measured with any of the diodes investigated will be greater than the actual dose ratio in water.

The importance of the data presented here, with regards to clarifying the apparent ambiguity in diode detector response in small fields, should not be dismissed - as even the IPEM Report Number 103 [5] states that for diode detectors the high atomic number of silicon leads to a higher response to low energy photons compared to water and that an under-response for narrow fields is due to the reduced low energy photon contribution to the small field dose. This is clearly not the case given the results presented in Chapter 3.

The combined benchmarking of the linac model in combination with a comprehensive set of simulated diode detectors, as presented in Chapter 3, had not yet been reported on in the literature. Part of the motivation for investigating and presenting such a comprehensive set of data was that very little work had been done which guided the clinical user in diode detector selection based on Monte Carlo derived small field $k_{Q_{clin},Q_{msr}}^{f_{clin},f_{msr}}$ correction factors. Not only were multiple detectors modelled but the combined linac-detector models were commissioned against isocentric experimental readings taken at depths of 1.5, 5.0 and 10.0 cm. Using multiple depths was novel and maximized the chance of an optimized incident electron energy being selected and complemented the preferred large field commissioning techniques [22]. We conclude a protocol-like approach to Monte Carlo small field beam commissioning and detector modelling may be beneficial to the community.

The work presented in Chapter 3 demonstrates that Monte Carlo simulation data can be used to determine $k_{Q_{clin},Q_{msr}}^{f_{clin},f_{msr}}$ correction factors, which when applied to measured relative output ratios is "*a requirement for accurate small field relative dosimetry*".

7.1.3 Chapter 4 - Diode detector model simplification and electron source parameterization

The general conclusions of the work presented in Chapter 4 were as follows: (1) detector models can be simplified to produce $OR_{det_{MC}}^{f_{clin}}$ to within ±1.0% of those calculated using the complete design geometry, (2) diode detector correction factors are a function of chip radius (and depend on the amount of shielding material present) and (3) $k_{Q_{clin},Q_{msr}}^{f_{clin},f_{msr}}$ are insensitive to the electron energy and spot size variations investigated. The overarching conclusions being that simplified detector models may be used within the proposed small field dosimetry formalism and correction factors calculated for a generic Varian iX model may be sufficient for general clinical implementation of published correction factors.

Validating that simplified detector models can be used for calculating small field $OR_{det_{MC}}^{f_{clin}}$ was novel and clearly required - given that other investigators had already used unsubstantiated detector model simplifications to report small field dosimetric results [42,98,99]. Validating the use of simplified detector models clearly established that the Monte Carlo simulation results

of Scott *et al* [98,99] could be interpreted as being accurate and that no systematic error in linac modelling had been unintentionally concealed by their approach to detector model simplification. This was an important detail to have clarified as the results of Scott *et al* [98] contradicted that of Eklund and Ahnesjö [42] - both authors using simplified detector models.

The simulation data for a fixed field size of side 0.5 cm showing the response factor plotted as a function of active volume radius perpendicular to the beam axis is of great importance and at the time of publication had not yet been reported on in the literature. The data clearly revealed that response factors for radii ≥ 0.625 mm, calculated using equivalent silicon and water volumes, are clearly incorrect with respect to the accurate implementation of the proposed small field dosimetry formalism. In fact, at a chip radius of 1.00 mm the silicon over-response is off-set by the volume effect and results in no correction - which is what Ralston *et al* [92] found experimentally. The data also showed that silicon diode detectors, with an active volume radius greater than 1.00 mm, will result in a measured output ratio that is less than the relative absorbed dose to a point like volume of water. These results are significant as they show the relationship between silicon chip dimension and relative response to a point like volume of water. At the time of publication this was not well understood by the community and helped clarify the discussion around the application of the Alfonso formalism.

The work in Chapter 4 was published in parallel to that of Francescon *et al* [45] - which showed an insensitivity of $k_{Q_{clin},Q_{msr}}^{f_{clin},f_{msr}}$ to source parameterization for a Siemens Primus™ and Elekta Synergy®. The implication of $k_{Q_{clin},Q_{msr}}^{f_{clin},f_{msr}}$ being invariant to electron source energy and spatial FWHM is that the clinical implementation of the proposed dosimetry formalism may not require experimental validation of either parameter prior to using published Monte Carlo derived correction factors. The impact is significant but would only hold for treatment machines of the same make, model, collimation and nominal accelerating potential.

The work presented in Chapter 4 demonstrates that Monte Carlo derived $k_{Q_{clin},Q_{msr}}^{f_{clin},f_{msr}}$ correction factors can be applied to treatment machines of the same make, model, collimation and nominal accelerating potential. Each aspect of the modelling process is clearly "*a requirement for accurate small field relative dosimetry*".

7.1.4 Chapter 5 - Small field dosimetric characterization of a new 160-leaf MLC

The Chapter 5 conclusions were as follows: (1) the Agility MLC and MLCi2 relative output, profile widths and associated uncertainties were all found to differ, (2) the Agility MLC performs to a tighter positional tolerance than does the MLCi2 and (3) the air-core fiber optic scintillation dosimeter can be used to experimentally derive the field size specific diode detector replacement

correction factors to within ±1.0% of the Monte Carlo calculated values reported by Francescon *et al* [45] for the MLCi2.

Although some of the data analysis performed in Chapter 5 was the same as that presented in Chapter 2 the novel contributions of the work are evident in the comprehensive characterization of small field dose profiles and penumbral widths for two MLC systems. Measuring the very small change in field size as a function of collimator rotation was also novel and had not previously been reported on in the literature. The data again demonstrates the importance of experimental methods in the accurate and precise characterization of collimation systems for use in SRS and/or SBRT applications.

The ambiguity in reporting measured small field output ratios with respect to the nominal field size was becoming clear for many of the active researchers in the area of small field dosimetry. At the time of publication no other work had appeared in the literature that presented such a thorough experimental implementation of the proposed formalism. The impact of reporting relative output data alongside the measured field widths is subtle but just as important as understanding the distinction between measured relative output ratios and the associated relative output factors in water.

Wang *et al* [111] had explored using Monte Carlo simulation to investigate a similar BC400 scintillator air-core dosimeter for use in small field

applications. At field sizes smaller than 0.5 cm the authors report that when compared to water the scintillator detector over-responded by 2.0% when used in a parallel orientation and under-responded by 1.5% when used in a perpendicular orientation. The 1.5% under-response was attributed to volume averaging over the 4.0 mm length of BC400. The impact of validating scintillator derived $k_{Q_{clin},Q_{msr}}^{f_{clin},f_{msr}}$ correction factors were consistent with the Monte Carlo derived correction factors of Francescon *et al*. [45] was significant as it removed most of the ambiguity regarding the Wang *et al* [111] paper and corroborates the previous experimental results of Ralston *et al.* [92] - which relied on EBT2 film data which had an inherent Type A uncertainty quoted at ±2.5%.

The work presented in Chapter 5 demonstrates that given the appropriate choice of detector one can consider the small field dosimetric characterization of a delivery system, and the derivation of $k_{Q_{clin},Q_{msr}}^{f_{clin},f_{msr}}$ correction factors, as a measurement based activity. This negates the requirement for detailed Monte Carlo simulations, but does not remove the uncertainty on $k_{Q_{clin},Q_{msr}}^{f_{clin},f_{msr}}$ - as experimental data always has an associated measurement uncertainty.

Each aspect of the experimental process is, as suggested earlier, "*a requirement for accurate small field relative dosimetry*". However, the more correct statement is that each aspect of the experimental process and the

proper reporting of measured data are both “a r*equirement for accurate small field relative dosimetry*”.

7.1.5 Chapter 6 - Reporting corrected small field relative outputs

There were a number of important conclusions drawn from the work presented in Chapter 6: (1) dosimetric field widths increase with respect to the geometric field width as a function of increased source occlusion, (2) discrepancies between different published small field relative output data may be attributed to reporting output as a function of the nominal field size and (3) using FS_{eff} as a small field metric relieves much of the ambiguity in reporting and simplifies the measured dosimetric field widths into one representative value.

At the time the work of Chapter 6 was conceived most, if not all, of the small field studies had presented dosimetric data measured on a single linac, focused on the relative response of various detector types and appeared to have been presented as a function of the nominal field size. The impact of defining a field size metric for use in small field dosimetry was clearly demonstrated by applying the methodology to a population of linacs of the same head design and nominal accelerating potential. The concept of an effective field size was novel and removed much of the field size ambiguity associated with reporting small field relative output data [31].

Each linear accelerator head design will have different source occlusion characteristics and therefore the relationship between the geometric and dosimetric field widths will be different to those presented in the work of Chapter 6. However, the anticipated difference in relative output between various accelerator head designs and collimation systems will be small if the relative output data is correctly presented as a function of the effective field size (FS_{eff}). Naturally this only holds for the same beam energy and would require standardization in experimental set-up.

If a standard measurement depth and source-to-detector distance were to be invoked then the equivalent field area (FA_{equ}) could be used to facilitate the comparison of small field dosimetric data regardless of collimation type. The impact of this is significant as both the IAEA and the AAPM are making a clear move towards a CoP like approach to small field dosimetry. A small field metric that can be used to represent the dosimetric field size is clearly "*a requirement for accurate small field relative dosimetry*".

7.2 A current "state-of-affairs" in small field dosimetry

Research and community interest in small field dosimetry has been remarkable since the publication of the Alfonso *et al* [1] paper. The well thought-out but simple formalism marks the start of a new era in small field dosimetry and the work presented here will have a significant place within the lineage of papers published within this time period.

A number of very good papers have recently been published that follow on from the work presented in Chapters 2, 3, 4 and 5. As such, this review can be thought of as a current “state-of-affairs” in small field dosimetry at the time of writing. The following describes the dependence of dosimeter response on active volume density and reviews a small field cavity theory that accounts for the density dependence. Advancements in detector design, investigated through the use of Monte Carlo simulation, will also be explored and the first flattening filter free (FFF) small field dosimetry results to appear in the literature will be reviewed.

7.2.1 Active volume density and diode detector over-response

Deriving $k_{Q_{clin},Q_{msr}}^{f_{clin},f_{msr}}$ correction factors using Monte Carlo simulation or experimental methods is important and does provide for accurate small field dosimetry. However, when the conventional thinking was that diode detectors should present an under-response in small fields, due to the reduced low energy photon contributions in small field geometries, the obvious question was why is it that the relative small field response of diode detectors was, in fact, greater than that of water.

As the field size decreases, the number of low energy photons in the beam decreases, which results in a decrease in the mass energy coefficient relative to larger field sizes. Aspradakis *et al.* [5] proposes that this alone should result in an diode detector under-response - given that the ratio of

mass energy absorption coefficients of silicon-to-water exhibits a near eight fold increase at low photon energies [97]. However, Scott *et al.* [98] clearly showed that the silicon-to-water stopping power ratio and mass energy absorption coefficients change very little at small field sizes. The authors inferred that diode detector over-response is not due to differences in atomic composition between water and silicon and suggested the over-response was due to the higher physical density of silicon.

The hypothesis that diode detector over-response is a density effect was tested by Scott *et al.* [100] using Monte Carlo simulations of artificial “water” substances having densities of silicon, diamond and air having the atomic composition, mass stopping power and mass energy absorption coefficients of unit-density water. The simulation results clearly show that at the smallest field sizes detector response correlates with the mass density of the active volume - with the artificial silicon and diamond density detectors having an over-response relative to unit-density water, and the artificial air density detector having an under-response relative to an equivalent volume of unit-density water. The results do demonstrate that the variation in detector response at small field sizes is due to active volume mass density rather than differences in atomic composition. However, demonstrating the effect through simulation does not provide a root cause explanation regarding the density dependence.

7.2.2 Cavity theory and the dependence on active volume density

Fenwick *et al* [43] continue the work and incorporate the density effect into a cavity theory explanation. The cavity theory is developed by splitting the absorbed dose to the sensitive volume into two components - that which is imparted by electrons liberated by photon interactions that occur inside and outside the detector active volume. The splitting of absorbed dose into an 'internal' and 'external' component was rationalized by making two assumptions: (1) the primary fluence of a wide, high energy, photon field is uniform throughout the water phantom and (2) electrons liberated within the cavity mostly escape from within it.

The authors note that if some, but not all, of the internally liberated electrons escape from the cavity then the ratio of dose-to-water to dose-to-detector-in-water can be shown to vary as a function of cavity density. The breakthrough comes when the authors link detector response and density to the level of central axis lateral electronic disequilibrium. Of course this occurs for field sizes that do not satisfy the electronic equilibrium condition inferred by the first assumption but this is taken into account by splitting the absorbed dose into 'internal' and 'external' components. When normalized to a square field of side 10.0 cm the relative variation in lateral electronic equilibrium (or lack thereof) was shown to be very nearly equivalent to the conventional phantom scatter factors for square fields of side down to 0.25 cm.

Although not explicitly stated by the authors one can infer that when compared to water the diode detector over-response is the result of an increased number of internally generated electrons that do not escape from the active volume. When normalized back to a field size that provides charged particle equilibrium the increase in electron number in small field geometries compensates for some of the inherent lateral charged particle disequilibrium. The density increase is essentially providing a mechanism for lateral build-up within the detector active volume - which manifests itself as an over-response in small field geometries relative to a field size that provides charged particle equilibrium.

7.2.3 Compensating for detector response in small fields

Charles *et al* [18] used Monte Carlo simulation at a nominal 6 MV to investigate optically stimulated luminescent dosimeters (OSLDs) as a viable small field dosimeter. The authors clearly demonstrate that modelling the OSLD and the surrounding air gap created by the detector case is necessary in benchmarking the simulation data back to experiment. The authors then explore the influence of varied air gap geometries on small field OSLD small field response.

An interesting linear relationship is revealed between the upstream air gap thickness and the percent dose reduction for square field sizes of side 9.8 cm down to 0.6 cm. For the smallest field size a 0.5 mm, an air gap immediately upstream of the active detector volume results in a 5%

reduction in the detector response relative to the no air gap simulation data. For field sizes of side greater than 3.0 cm an upstream air gap of up to 2.0 mm was shown not to alter the OSLD detector relative response. The implications of the work are twofold: (1) when performing small field measurements care must be taken to ensure there are no unintentional air gaps surrounding the detector and (2) creating an intentional air gap upstream of the active volume of diode detectors may be used to offset the well documented detector over-response.

In a subsequent work Charles *et al* [19] do just this and exploit the air gap to detector response relationship and quantify the volume of upstream air gap required to negate the over-response of both photon and electron diodes. For each detector investigated the authors plot the ratio of dose-to-water to dose-to-detector as a function of upstream air gap and show that an optimal air gap can be identified when this ratio is the same for all field sizes. Following just such an approach results in a “correction-less” diode detector with a $k_{Q_{clin},Q_{msr}}^{f_{clin},f_{msr}}$ value of unity (to within ± 0.5%). Underwood *et al.* [106,107] explore a similar approach to modifying detector response in small field geometries and demonstrate that appropriately placed compensatory materials can be used to construct a “water equivalent” PTW 60003 diamond detector and PTW 31006 PinPoint chamber.

7.2.4 Small field dosimetry and flattening filter free beams

High energy photon treatment beams in a flattening filter free mode have recently become commercially available and their use is gaining favour in some external beam radiotherapy applications. With the flattening filter removed from the beam path the maximum deliverable dose rate can be increased. For example, the maximum deliverable FFF dose rate available on the Varian TrueBeam linear accelerator is 2400 $MU \cdot min^{-1}$, which is far greater than a traditional external beam dose rate of 400 to 600 $MU \cdot min^{-1}$. This option has generally been commissioned and implemented clinically as part of stereotactic radiosurgery (SRS), stereotactic body radiotherapy (SBRT) and/or stereotactic ablative radiotherapy (SABR) programs, where patient position during treatment is critical and therefore a reduction in beam-on time is advantageous.

Only recently has the FFF mode become available on traditional gantry mounted linear accelerator based systems. At the time of writing only the work of Lechner *et al.* [72] has appeared in the literature comparing small field relative output for a gantry mounted linear accelerator based system in flattened and unflattened modes. The authors use well thought out experimental procedures to compare the measured relative output for nominal 6 and 10 MV flattened and unflattened photon beams. The general conclusions being that apart from the shielded diodes irradiated at 10 MV the dose response ratios of all other detectors showed only small differences between filtered and unfiltered modes. The underlying message being that

one may be well justified in using the same $k_{Q_{clin},Q_{msr}}^{f_{clin},f_{msr}}$ across both filtering modes at the same accelerating potential.

7.3 Future work

The recent developments in small field dosimetry are undeniable and many of the questions posed in the past decade by the likes of McKerracher and Thwaites [79,81,82,83] Sauer and Wilbert [97], Li *et al* [73] and Verhaegen *et al* [108] have now been addressed. However, research will continue and the following topics could potentially be directions for future work.

7.3.1 Experimental validation of a correction-less diode

Constructing a “correction-less” diode detector by introducing an intentional air gap upstream of the active volume is an attractive option for overcoming the well established over-response in small field relative dosimetry. Charles *et al* [19] have shown that an optimal air gap can be identified when the ratio of dose-to-water to dose-to-detector is the same for all field sizes. The obvious next step would be to experimentally validate this approach of identifying an optimal air gap and then confirm the modified diode is indeed “correction-less”. Upstream air gaps of varying thicknesses can easily be created using a set of solid water caps fabricated to fit over the top of the detector. Another method would be to fabricate one cap that could be

adjusted to create various air gap thicknesses. In both cases the cap would need to be water tight and the gap resolved to within ± 0.1 mm.

Fabricating a set of caps would provide for experimental validation in a beam of known quality but could not be used for the experimental determination of an optimal air gap in a beam of unknown quality. The inherent dilemma in using experimental methods alone is that one must already have the dose-to-water as a function of field size. Having dose-to-water as a function of field size implies that $k_{Q_{clin},Q_{msr}}^{f_{clin},f_{msr}}$ could also be calculated for the diode detector and therefore the cap(s) would not be required. In fact, if one already has dose-to-water as a function of field size then no measurements would be required at all.

Monte Carlo simulation could be used to investigate over what range of beam qualities a “correction-less” diode of fixed air gap thickness would still perform as “correction-less”. This would be useful future work as it could potentially demonstrate transferability of one “correction-less” diode across various treatment platforms.

7.3.2 Towards a small field dosimetry code of practice

The Alfonso *et al* [1] formalism is simple and yet there is little direction given in the paper regarding clinical implementation. This is not necessarily a surprise as the intent of the paper was to outline a new dosimetry framework

which extended the recommendations given in conventional CoPs for clinical reference dosimetry and to encourage research in the topic.

The proposed formalism does move towards traceability but an unambiguous small field CoP would require specific procedures regarding: detector selection, experimental requirements, set-up conditions and measurement methods and the application of detector specific $k_{Q_{clin},Q_{msr}}^{f_{clin},f_{msr}}$, as well as consistent reporting. Many of the details regarding detector selection and experimental set-up have been addressed in the literature and the results could therefore be distilled into procedural recommendations and/or requirements. What has not appeared in the literature is any clear recommendation regarding how beam quality should be reported when presenting small field dosimetric quantities, nor has there been any work which has shown a functional relationship between $k_{Q_{clin},Q_{msr}}^{f_{clin},f_{msr}}$ and beam quality.

Correlating changes in $k_{Q_{clin},Q_{msr}}^{f_{clin},f_{msr}}$ as a function of beam quality in the conventional CoP reference field beam may be a sufficient indicator for the transferability of $k_{Q_{clin},Q_{msr}}^{f_{clin},f_{msr}}$ between clinical beams and could then be used in a look-up table type approach to setting $k_{Q_{clin},Q_{msr}}^{f_{clin},f_{msr}}$ for a given clinical beam. Although the beam quality of the machine-specific reference field might well be used to define the small field CoP beam quality index it could be argued that using the conventional reference dosimetry beam quality index

throughout alleviates any ambiguity. Either way these issues will require investigation and give guidance as to potential future work. The increasing availability of FFF beams and their use in small field situations such as SBRT gives a further spur for research-based recommendations on these issues.

Guidelines regarding an uncertainty budget assessment will also need to be established. The standard approach for expressing measurement uncertainties in reference dosimetry is to follow the Comité International des Poids et Mesures [54] classification scheme of Type A and Type B uncertainties. Evaluating Type B standard uncertainties is based on methods other than statistical analysis of a series of observations. Type B uncertainties include unknown but suspected influences on measurement and, as noted in the IAEA Technical Report Series No. 398, the application of correction factors or physical data taken from the literature. The report states that there are no rigid rules for estimating Type B standard uncertainties and that the experimenter should use his or her best knowledge and experience and provide Type B uncertainty estimates as the equivalent of standard deviation. However, within a small field dosimetry CoP there would need to be rigid rules regarding estimates of the associated Type B uncertainties related to the application of $k_{Q_{clin},Q_{msr}}^{f_{clin},f_{msr}}$. This will need to be resolved.

7.4 Concluding remarks

The radiation oncology community will continue to strive towards increased radiotherapy efficacy through refinements in current treatment techniques and/or the potential development of new techniques altogether. It is plausible that in many cases future radiosurgery will become the frontline treatment modality of choice with traditional surgery being reserved as an adjuvant therapy. As such, the traceability, accuracy and consistency of radiation measurements will become even more essential. The work presented in this thesis adds to the required body of knowledge regarding small field dosimetry and should prove very useful for the radiation oncology community.

List of References

[1] Alfonso R *et al.* 2008 A new formalism for reference dosimetry of small and nonstandard fields, *Med. Phys.* **35**, 5179-86

[2] Almond P R, Biggs P J, Coursey B M, *et al.* 1999 Report of AAPM Therapy Physics Committee Task Group 51: Protocol for clinical reference dosimetry of high-energy photon and electron beams *Med. Phys.* **26**, 1847-70

[3] Andreo P 1991 Monte Carlo techniques in medical radiation physics *Phys. Med. Biol.* **36**, 861-920

[4] Araki F 2006 Monte Carlo study of a Cyberknife stereotactic radiosurgery system *Med. Phys.* **33,** 2855-63

[5] Aspradakis M M, Byrne J P, Palmans H, *et al*. 2010 IPEM Report Number 103: Small Field MV Photon Dosimetry. Published by the Institute of Physics and Engineering in Medicine.

[6] Babcock K, Cranmer-Sargison G and Sidhu N P 2008 Increasing the speed of DOSXYZnrc Monte Carlo simulations through the introduction of non-voxelated geometries *Med. Phys.* **35**, 633-44

[7] Bouchard H, Seuntjens J, Carrier J F and Kawrakow I 2009 Ionization chamber gradient effects in nonstandard beam configurations *Med. Phys.* **36**, 4654-63

[8] Beddar A S, Mackie T R and Attix F H 1992 Water-equivalent plastic scintillation detectors for high-energy beam dosimetry: Physical

characteristics and theoretical considerations *Phys. Med. Biol.* **37**, 1883-1900

[9] Berger M J 1963 Monte Carlo calculation of the penetration and diffusion of fast charged particles *Meth. Comput. Phys.* **1**, 135–215

[10] Bergstrand E S, Shortt K R, Ross C H and Hole E O 2003 An investigation of the photon energy dependence of the EPR alanine dosimetry system *Phys. Med. Biol.* **48**, 1753-71

[11] Beyzadeoglu M, Ozyigit G and Ebruli C 2010 Basic Radiation Oncology, Springer Publishing

[12] Bielajew A F and Rogers D W O 1987 PRESTA: The parameter reduced electron-step transport algorithm for electron Monte Carlo transport *Nucl. Instrum. Methods. Phys. Res.* B. **18**, 165–181.

[13] Bielajew A F, Rogers D W O, and Nahum A E 1985 Monte Carlo simulation of ion chamber response to $_{60}$CO - resolution of anomalies associated with interfaces *Phys. Med. Biol.* **30**, 419-428.

[14] Bush K, Zavgorodni S F and Beckham W A 2007 Azimuthal particle redistribution for the reduction of latent phase-space variance in Monte Carlo simulations *Phys. Med. Biol.* **52**, 4345-60

[15] Boyer A L, Ochran T G, Nyerick C E and Waldron T J 1992 Clinical dosimetry for implementation of a multileaf collimator *Phys. Med. Biol.* **19**, 1255-61

[16] Cadman P, McNutt T and Bzdusek K 2005 Validation of physics improvements for IMRT with a commercial treatment-planning system. *J. Appl. Clin. Med. Phys.* **6** 74-86

[17] Capote R, Sanchez-Doblado F, Leal A, Lagares J I and Arrans R 2004 An EGSnrc Monte Carlo study of the microionization chamber for

reference dosimetry of narrow irregular IMRT beamlets *Med. Phys.* **31**, 2416-22

[18] Charles P H, Crowe S B, Kairn T *et al.* 2012 The effect of very small air gaps on small field dosimetry *Phys. Med. Biol.* **57,** 6947-6960.

[19] Charles P H, Crowe S B, Kairn T *et al.* 2013 Monte Carlo-based diode design for correction-less small field dosimetry *Phys. Med. Biol.* **58**, 4501-12

[20] Chen F, Graeff C F and Baffa O 2005 K-band EPR dosimetry: small-field beam profile determination with miniature alanine dosimeter *Appl. Rad. Iso.* **62**, 267-71

[21] Chern S, Leavitt D D, Jensen R L and Shrieve D C 2006 Is smaller better? Comparison of 3-mm and 5-mm leaf size for stereotactic radiosurgery: A dosimetric study *Int. J. Radiation Oncol. Biol. Phys.* **66,** S76-S81

[22] Chetty I J, Curran B, Cygler J E *et al.* 2007 Report of the AAPM Task Group No. 105: Issues associated with clinical implementation of Monte Carlo-based photon and electron external beam treatment planning *Med. Phys.* **34**, 4818-53

[23] Chibani O, Moftah B and Ma C M C 2011 On Monte Carlo modeling of megavoltage photon beams: A revisited study on the sensitivity of beam parameters *Med. Phys.* **38**, 188-201

[24] Chung E, Bouchard H, Seuntjens J 2010 Investigation of three radiation detectors for accurate measurement of absorbed dose in nonstandard fields *Med. Phys.* **37**, 2404-13

[25] Cosgrove V P, Jahn U, Pfaender M, Bauer S, Budach V and Eurm R E 1999 Commissioning of a micro multi-leaf collimator and planning system for stereotactic radiosurgery *Radiother. Oncol.* **50**, 325-36

[26] Cosgrove V P, Thomas M D, Weston S J, *et al.* 2009 Physical characterization of a new concept design of an Elekta radiation head with integrated 160-leaf multi-leaf collimator *Int. J. Radiat. Oncol. Biol. Phys*. **75**, S722–S723.

[27] Cranmer-Sargison G, Weston S, Sidhu N P and Thwaites D I 2011a Experimental small field 6 MV output ratio analysis for various diode detector and accelerator combinations *Radiother. Oncol.* **100**, 429-35

[28] Cranmer-Sargison G, Weston S, Evans J A, Sidhu N P and Thwaites D I 2011b Implementing a newly proposed Monte Carlo based small field dosimetry formalism for a comprehensive set of diode detectors *Med. Phys*. **38**, 6592-602

[29] Cranmer-Sargison G, Weston S, Evans J A, Sidhu N P and Thwaites D I 2012 Monte Carlo modelling of diode detectors for small field MV photon dosimetry: detector model simplification and the sensitivity of correction factors to source parameterization *Phys. Med. Biol.* **57**, 5141-53

[30] Cranmer-Sargison G, Liu P Z Y, Weston S, Suchowerska N and Thwaites D I 2013 Small field dosimetric characterization of a new 160-leaf MLC *Phys. Med. Biol.* **57**, 7343-54

[31] Cranmer-Sargison G, Charles P H, Trapp J V and Thwaites D I 2013 A methodological approach to reporting corrected small field relative outputs *Radiother. Oncol.* **109**, 350-355

[32] Curran B H, Balter J M and Chetty I J 2006 Monograph No. 32, Integrating New Technologies into the Clinic: Monte Carlo and Image-Guided Radiation Therapy, Medical Physics Publishing

[33] Das I J, Ding G X and Ahnesjö A 2008 Small fields: Nonequilibrium radiation dosimetry *Med. Phys.* **35**, 206-15

[34] Daşu A, Lofroth P O and Wickman G 1998 Liquid ionization chamber measurements of dose distributions in small 6 MV photon beams *Phys. Med. Biol.* **43**, 21-36

[35] Dhabaan A *et al.* 2010 Dosimetric performance of the new high-definition multileaf collimator for intracranial stereotactic radiosurgery *J. Appl. Clin. Med. Phys.* **11**, 197-211

[36] Dieterich S and Sherouse G W 2011 Experimental comparison of seven commercial dosimetry diodes for measurement of stereotactic radiosurgery cone factors *Med. Phys.* **38**, 4166-73

[37] Ding G X 2003 Using Monte Carlo simulations to commission photon beam output factors - a feasibility study *Phys. Med. Biol.* **48**, 3865-74

[38] Ding G X, Duggan D M, Coffey C W 2006 Commissioning stereotactic radiosurgery beams using both experimental and theoretical methods *Phys. Med. Biol.* **51**, 2549-66

[39] Ding G X, Duggan D M, Coffey C W 2009 A theoretical approach for non-equilibrium radiation dosimetry *Phys. Med. Biol.* **53**, 3493-9.

[40] Eklund K and Ahnesjö A 2009 Modeling silicon diode energy response factors for use in therapeutic photon beams *Phys. Med. Biol.* **54**, 6135-50

[41] Eklund K and Ahnesjö A 2010a Spectral perturbations from silicon diode detector encapsulation and shielding in photon fields *Med. Phys.* **37**, 6055-60

[42] Eklund K and Ahnesjö A 2010b Modeling silicon diode dose response factors for small photon fields *Phys. Med. Biol.* **55**, 7411-23

[43] Fenwich J D, Kumar S, Scott A and Nahum A E 2013 Using cavity theory to describe the dependence on detector density of dosimeter response in non-equilibrium small fields *Med. Biol.* **58**, 2901-23

[44] Francescon P, Cora S and Cavedon C 2008 Total scatter factors of small beams: A multidetector and Monte Carlo study *Med. Phys.* **35**, 504-13

[45] Francescon P, Cora S and Satariano N 2011 Calculation of $k_{Q_{clin},Q_{msr}}^{f_{clin},f_{msr}}$ for several small detectors and for two linear accelerators using Monte Carlo simulations *Med. Phys.* **38**, 6513-27

[46] Goudsmit S A and J L Saunderson 1940a Multiple scattering of electrons *Phys. Rev.* **57**, 24-29.

[47] Goudsmit S A and J L Saunderson 1940b Multiple scattering of electrons II *Phys. Rev.* **58**, 36-42.

[48] Griessbach I, Lapp M, Gademann G and Harder D 2005 Dosimetric characteristics of a new unshielded silicon diode and its application in clinical photon and electron beams *Med. Phys.* **32**, 3750-4

[49] Hartmann B, Martisiková M and Jäkel O 2010 Homogeneity of Gafchromic EBT2 film *Med. Phys.* **37**, 1753-6

[50] Haryanto F, Fippel M, Laud W, Dohm O and Nüsslin F 2002 Investigation of photon beam output factors for conformal radiation

therapy - Monte Carlo simulations and measurements *Phys. Med. Biol.* **47**, N133-43

[51] Hazard L J *et al* 2009 Conformity of LINAC-based stereotactic radiosurgery using dynamic conformal arcs and micro-multileaf collimator *Int. J. Radiat. Oncol. Biol. Phys.* **73**, 562-70

[52] Heydarian M, Hoban P W and Beddoe A H 1996 A comparison of dosimetry techniques in stereotactic radiosurgery *Phys. Med. Biol.* **41**, 93-110

[53] Higgins P D, Sibata C H, Siskind L, Sohn J W 1995 Deconvolution of detector size effect for small field measurement *Med. Phys.* **22**, 1663-6

[54] IAEA 2000 Technical Reports Series No. 398: Absorbed Dose Determination in External Beam Radiotherapy, International Atomic Energy Agency, Vienna.

[55] ICRU 1976 Determination of absorbed dose in a patient irradiated by beams of x or gamma rays in radiotherapy procedures. Report No. 24, U.S. National Bureau of Standards

[56] IEC 2007 60976 Medical electrical equipment - Medical electron accelerators - Functional performance characteristics, Edition 2.0

[57] Jenkins T, Nelson W, Rindi A, Nahum A E and Rogers D W O 1989 *Monte Carlo Transport of Electrons and Photons,* New York: Plenum Press, 115-137

[58] Johns H E and Cunningham J R 1983 The physics of radiology. Edition 4.0, Charles C Thomas Publishing

[59] Kahn F M 2003 The physics of radiation therapy, Edition 3.0, Lippincott Williams & Wilkins

[60] Karzmarh C J, Nunan C S and Tanabe E 1992 Medical Linear Accelerators, McGraw-Hill Companies Health Professions Division

[61] Kawrakow I 1996 Electron transport: longitudinal and lateral correlation algorithm *Nucl. Instrum. Methods. Phys. Res. B.* **114**, 307-326.

[62] Kawrakow I 2000 Accurate condensed history Monte Carlo simulation of electron transport, part I: EGSnrc, the new EGS4 version *Med. Phys.* **27**, 485-498

[63] Kawrakow I and A F Bielajew 1998a On the condensed history technique for electron transport *Nucl. Instrum. Methods. Phys. Res. B.* **142**, 253-280

[64] Kawrakow I, and A F Bielajew 1998b On the representation of electron multiple elastic scattering distributions for Monte Carlo calculations *Nucl. Instrum. Methods. Phys. Res. B.* **134**, 325-336

[65] Kawrakow I and Fippel M 2000 Investigation of variance reduction techniques for Monte Carlo photon dose calculation using XVMC *Phys. Med. Biol.* **45**, 2163-83

[66] Kawrakow I, Rogers D W O and Walters B R B 2004 Large efficiency improvements in BEAMnrc using directional Bremsstrahlung splitting *Med. Phys.* **31**, 2883-98

[67] Kawrakow I and Rogers D W O 2006 The EGSnrc Code System: Monte Carlo Simulation of Electron and Photon Transport, National Research Council of Canada, Ottawa PIRS-701

[68] Klein D M, Tailor R C, Archambault L, *et al.* 2010 Measuring output factors of small fields formed by collimator jaws and multileaf collimator using plastic scintillation detectors *Med. Phys.* **37**, 5541-9

[69] Lambert J, Yin Y, McKenzie D R, *et al.* 2008 Cerenkov-free scintillation dosimetry in external beam radiotherapy with an air core light guide *Phys. Med. Biol.* **53**, 3071-80

[70] Lambert J, Yin Y, McKenzie D R, Law S, Ralston A and Suchowerska N 2010 A prototype scintillation dosimeter customised for small and dynamic megavoltage radiation fields *Phys. Med. Biol.* **55**, 1115-26

[71] Laud W U and Wong T 2003 The volume effect of detectors in the dosimetry of small fields used in IMRT *Med. Phys.* **30**, 341-7

[72] Lechner W, Palmans H, Sölkner L, Grochowska P, Georg D 2013 Detector comparison for small field output factor measurements in flattening filter free photon beams *Radiother. Oncol.* **109**, 356-360

[73] Li S, Rashid A, He S and Djajaputra D 2004 A new approach in dose measurement and error analysis for narrow photon beams (beamlets) shaped by different multileaf collimators using a small detector *Med. Phys.* **31**, 2020-32

[74] Liu P Z Y, Suchowerska N, Lambert J, Abolfathi P and McKenzie D R 2011 Plastic scintillation dosimetry: comparison of three solutions for the Cerenkov challenge *Phys. Med. Biol.* **56**, 5805-21

[75] Liu P Z Y, Suchowerska N, Abolfathi P and McKenzie D R 2012 Real-time scintillation array dosimetry for radiotherapy: The advantages of Photomultiplier detectors *Med. Phys.* **39** 1688-96

[76] Ma C M and Rogers D W O 2006 BEAMDP as a General-Purpose Utility, National Research Council of Canada, Ottawa PIRS-509e(rev A)

[77] British Measurement and Testing Association 2003 Measurement Good Practice Guide No. 36: Estimating Uncertainties in Testing

[78] United Kingdom Accreditation Service (UKAS) 2007 M3003 Edition 2: The Expression of Uncertainty and Confidence in Measurement

[79] McKerracher C and Thwaites D I 1999 Assessment of new small-field detectors against standard-field detectors for practical stereotactic beam data acquisition *Phys. Med. Biol.* **44**, 2143-60

[80] McKerracher C and Thwaites D I 2006 Notes on the construction of solid-state detectors *Radiother. Oncol.* **79**, 348-51

[81] McKerracher C and Thwaites D I 2007a Head scatter factors for small MV photon fields. Part I: a comparison of phantom types and methodologies *Radiother. Oncol.* **85**, 277-85

[82] McKerracher C and Thwaites D I 2007b Head scatter factors for small MV photon fields. Part II: the effects of source size and detector *Radiother. Oncol.* **85**, 286-91

[83] McKerracher C and Thwaites D I 2008 Phantom scatter factors for small MV photon fields *Radiother. Oncol.* **86**, 472-75

[84] Monk J E, Perks J R, Doughty D and Plowman P N 2003 Comparison of a Micro-multileaf collimator with a 5-mm-leaf-width collimator for intracranial stereotactic radiotherapy *Int. J. Radiation Oncology Biol. Phys.* **57**, 1443-49

[85] Mould R F 1998 Introductory Medical Statistic, 3rd Edition. Medical Science Series, Institute of Physics Publishing.

[86] Nelson W R, Hirayama H, and Rogers D W O 1985 The EGS4 Code System, Report SLAC-265, Stanford Linear Accelerator Center

[87] Palmans H 2012 Determination of the beam quality index of high-energy photon beams under nonstandard reference conditions *Med. Phys.* **39**, 5513-19

[88] Pantelis *et al.* 2012 On the output factor measurements of the CyberKnife iris collimator small fields: Experimental determination of the $k_{Q_{clin},Q_{msr}}^{f_{clin},f_{msr}}$ correction factors for microchamber and diode detectors *Med. Phys.* **39**, 4875-85

[89] Pantelis *et al* 2011 On the implementation of a recently proposed dosimetric formalism to a robotic radiosurgery system *Med. Phys.* **37**, 2369-79

[90] Podgorsak E B 2005 Radiation Oncology Physics: A handbook for teachers and students. International Atomic Energy Agency, Vienna

[91] Popescu I A, Shaw C P, Zavgorodni S F, Beckham W A 2005 Absolute dose calculations for Monte Carlo simulations of radiotherapy beams *Phys. Med. Biol.* **50**, 3375-92

[92] Ralston A, Liu P, Warrener K, McKenzie D and Suchowerska N 2012 Small field correction factors derived using an air core fibre optic Scintillation dosimeter and EBT2 film *Phys. Med. Biol.* **57**, 2587-2602

[93] Rogers D W O *et al.* 1995 BEAM: A Monte Carlo code to simulate radiotherapy treatment units *Med. Phys.* **22**, 503-24

[94] Rogers D W O, Walters B R B and Kawrakow I 2005 BEAMnrc Users Manual, National Research Council of Canada, Ottawa PIRS-509(A)revK

[95] Rogers D W O, Kawrakow I, Seuntjens J P, Walters B R B and Mainegra-Hing E 2005 NRC User Codes for EGSnrc, National Research Council of Canada, Ottawa PIRS-702revB

[96] Sahoo N, Kazi A M and Hoffman M 2008 Semi-empirical procedures for correcting detector size effects on clinical MV beam profiles *Med. Phys.* **35**, 5124-33

[97] Sauer O A and Wilbert J 2007 Measurement of output factors for small photon fields *Med. Phys.* **34**, 1983-88

[98] Scott A, Nahum A E and Fenwich J D 2008 Using a Monte Carlo model to predict dosimetric properties of small radiotherapy photon fields *Med. Phys.* **35**, 4671-84

[99] Scott A, Nahum A E and Fenwich J D 2009 Monte Carlo modeling of small photon fields: Quantifying the impact of focal spot size on source occlusion and output factors, and exploring miniphantom design for small-field measurements *Med. Phys.* **36**, 3132-44

[100] Scott A, Kumar S, Nahum A E and Fenwich J D 2012 Characterizing the influence of detector density on dosimeter response in non-equilibrium small photon fields *Med. Biol.* **57** 4461-76

[101] Sham E, Seuntjens J, Devic S and Podgorsak E B 2008 Influence of focal spot on characteristics of very small diameter radiosurgical beams *Med. Phys.* **35**, 3317-30

[102] Sheikh-Bagheri D and Rogers D W O 2002 Monte Carlo calculation of nine megavoltage photon beam spectra using the BEAM code *Med. Phys.* **29**, 391-402

[103] Sonke J J, Brand B and van Herk M 2003 Focal spot motion of linear accelerators and its effect on portal image analysis *Med. Phys.* **30**, 1067-75

[104]Sutherland J G H and Rogers D W O 2010 Monte Carlo calculated absorbed-dose energy dependence of EBT and EBT2 film *Med. Phys.* **37**, 1110-6

[105]Tatcher M and Bjärngard B E 1993 Head-scatter factors in rectangular photon fields *Med. Phys.* **20** 205-6

[106]Underwood T S A, Winter H C, Hill M A and Fenwick J D 2013 Detector density and small field dosimetry: integral versus point dose measurement schemes *Med. Phys.* **40** 082102

[107]Underwood T S A, Winter H C, Hill M A and Fenwick J D 2013 Mass-density compensation can improve the performance of a range of different detectors under non-equilibrium conditions *Phys. Med. Biol.* **58**, 8295-8310

[108]Verhaegen F, Das I J and Palmans H 1998 Monte Carlo dosimetry study of a 6 MV stereotactic radiosurgery unit *Phys. Med. Biol.* **43**, 2755-68

[109]Walters B R B, Kawrakow I and Rogers D W O 2006 DOSXYZnrc Users Manual, National Research Council of Canada, Ottawa PIRS-794revB

[110]Walters B R B, Kawrakow I and Rogers D W O 2002 History by History statistical estimators in the BEAM code system *Med. Phys.* **29**, 2745-52

[111]Wang L L W and Beddar S 2011 Study of the response of plastic scintillation detectors in small-field 6 MV photon beams by Monte Carlo simulations *Med. Phys.* **38**, 1596-9

[112]Wu A, Zwicker R D, Kalend A M and Zheng Z 1993 Comments on dose measurements for a narrow beam in radiosurgery *Med. Phys.* **30**, 777-79

[113]Wulff J, Zink K and Kawrakow I 2008 Efficiency improvements for ion chamber calculations in high energy photon beams *Med. Phys.* **35**, 1328-36

[114]Zhu T C, Ahnesjö A, Lam K L, *et al.* 2009 Report of AAPM Therapy Physics Committee Task Group 74: In-air output ratio, S_c, for megavoltage photon beams *Med. Phys.* **36**, 5261-91

Appendix A

A.1 BEAMnrc input file: VARIAN_6MV_PHSP_A

```
VARIAN_6MV_PHSP_A
#!GUI1.0
AIR700ICRU
0, 0, 0, 0, 0, 3, 0,  IWATCH ETC.
25000000, 33, 75, 99, 29, 1000, 0, 0,  NCASE ETC.
50.0, 100.0, 100, ,  SELECTIVE BREM OPTIONS
-1, 19, -0.11, 0, 0, 0, 0.0, 0.0, 0.0, 0.0,  IQIN, ISOURCE + OPTIONS
0, MONOENERGETIC
6.2
0, 0, 0.7, 0.01, 0, -2, 2.0,  0 , ECUT,PCUT,IREJCT,ESAVE
0, 0, 0, 0, 0,  PHOTON FORCING
1, 6,  SCORING INPUT
0,1
0,  DOSE COMPONENTS
-0.0889, Z TO FRONT FACE
********** start of CM SLABS with identifier target  **********
10.0, RMAX
Target
2, NSLABS
-0.0889, ZMIN
0.0889, 0.7, 0.01, 0, 1, -1
W700ICRU
0.1575, 0.7, 0.01, 0, 2, -1
CU700ICRU
********** start of CM CONS3R with identifier pri_col  **********
10.0, RMAX
pri_coll
0.1575, ZMIN
7.3725, ZTHICK
4, NUM_NODE
0.1575, 2.5,
1.54, 2.5,
1.54, 0.613,
7.53, 2.09,
0.7, 0.01, 0, 3, -1,
VACUUM
0.7, 0.01, 0, 4, -1,
WLIGHT
********** start of CM SLABS with identifier be_win  **********
10.0, RMAX
AIR GAP
2, NSLABS
7.53, ZMIN
0.94, 0.7, 0.01, 0, 5, 0
VACUUM
0.0254, 0.7, 0.01, 0, 6, 0
BE700ICRU
********** start of CM FLATFILT with identifier fla_filt
**********
10.0, RMAX
FLATFILT
```

```
10.485, ZMIN
19, NUMBER OF LAYERS
1, 0.028, # CONES, ZTHICK OF LAYER 1
0.0,
0.064,
1, 0.028, # CONES, ZTHICK OF LAYER 2
0.064,
0.127,
1, 0.038, # CONES, ZTHICK OF LAYER 3
0.127,
0.191,
1, 0.041, # CONES, ZTHICK OF LAYER 4
0.191,
0.254,
1, 0.074, # CONES, ZTHICK OF LAYER 5
0.254,
0.381,
1, 0.1535, # CONES, ZTHICK OF LAYER 6
0.381,
0.508,
1, 0.1235, # CONES, ZTHICK OF LAYER 7
0.508,
0.635,
1, 0.1235, # CONES, ZTHICK OF LAYER 8
0.635,
0.762,
1, 0.1235, # CONES, ZTHICK OF LAYER 9
0.762,
0.889,
1, 0.1135, # CONES, ZTHICK OF LAYER 10
0.889,
1.016,
1, 0.2235, # CONES, ZTHICK OF LAYER 11
1.016,
1.27,
1, 0.2035, # CONES, ZTHICK OF LAYER 12
1.27,
1.524,
1, 0.2035, # CONES, ZTHICK OF LAYER 13
1.524,
1.778,
1, 0.1835, # CONES, ZTHICK OF LAYER 14
1.778,
2.032,
1, 0.1735, # CONES, ZTHICK OF LAYER 15
2.032,
2.286,
1, 0.142, # CONES, ZTHICK OF LAYER 16
2.286,
2.54,
1, 0.13, # CONES, ZTHICK OF LAYER 17
2.54,
2.794,
3, 0.097, # CONES, ZTHICK OF LAYER 18
2.794, 3.366, 3.81,
3.061, 3.302, 3.81,
1, 0.165, # CONES, ZTHICK OF LAYER 19
3.81,
3.81,
0.7, 0.01, 0, 7,
CU700ICRU
0.7, 0.01, 0, 8,
```

```
AIR700ICRU
0.7, 0.01, 0, 7,
CU700ICRU
0.7, 0.01, 0, 8,
AIR700ICRU
0.7, 0.01, 0, 7,
CU700ICRU
0.7, 0.01, 0, 8,
AIR700ICRU
0.7, 0.01, 0, 7,
CU700ICRU
0.7, 0.01, 0, 8,
AIR700ICRU
0.7, 0.01, 0, 7,
CU700ICRU
0.7, 0.01, 0, 8,
AIR700ICRU
0.7, 0.01, 0, 7,
CU700ICRU
0.7, 0.01, 0, 8,
AIR700ICRU
0.7, 0.01, 0, 7,
CU700ICRU
0.7, 0.01, 0, 8,
AIR700ICRU
0.7, 0.01, 0, 7,
CU700ICRU
0.7, 0.01, 0, 8,
AIR700ICRU
0.7, 0.01, 0, 7,
CU700ICRU
0.7, 0.01, 0, 8,
AIR700ICRU
0.7, 0.01, 0, 7,
CU700ICRU
0.7, 0.01, 0, 8,
AIR700ICRU
0.7, 0.01, 0, 7,
CU700ICRU
0.7, 0.01, 0, 8,
AIR700ICRU
0.7, 0.01, 0, 7,
CU700ICRU
0.7, 0.01, 0, 8,
AIR700ICRU
0.7, 0.01, 0, 7,
CU700ICRU
0.7, 0.01, 0, 8,
AIR700ICRU
0.7, 0.01, 0, 7,
CU700ICRU
0.7, 0.01, 0, 8,
AIR700ICRU
0.7, 0.01, 0, 7,
CU700ICRU
0.7, 0.01, 0, 8,
AIR700ICRU
0.7, 0.01, 0, 7,
CU700ICRU
0.7, 0.01, 0, 8,
AIR700ICRU
0.7, 0.01, 0, 7,
```

```
CU700ICRU
0.7, 0.01, 0, 8,
AIR700ICRU
0.7, 0.01, 0, 7,
CU700ICRU
0.7, 0.01, 0, 7,
AIR700ICRU
0.7, 0.01, 0, 7,
CU700ICRU
0, 0, 0, 8,
AIR700ICRU
0.7, 0.01, 0, 7,
CU700ICRU
0.7, 0.01, 0, 8,
AIR700ICRU
********** start of CM CHAMBER with identifier chamber  **********
15.0, RMAX
Ion Chamber
14.2, ZMIN
0, 15, 0, N_TOP, N_CHM, N_BOT
4.7625, 4.7752, 4.95, RADII FOR CENTRAL PART
0.629, 0, ZTHICK, FLAG FOR LAYER 1 IN CENTRAL PART
0.7, 0.01, 0, 0,
AIR700ICRU
0.0127, 0, ZTHICK, FLAG FOR LAYER 2 IN CENTRAL PART
0.7, 0.01, 0, 0,
KAPTON700ICRU
0.229, 0, ZTHICK, FLAG FOR LAYER 3 IN CENTRAL PART
0.7, 0.01, 1, 0,
AIR700ICRU
0.0051, 0, ZTHICK, FLAG FOR LAYER 4 IN CENTRAL PART
0.7, 0.01, 0, 0,
KAPTON700ICRU
0.234, 0, ZTHICK, FLAG FOR LAYER 5 IN CENTRAL PART
0.7, 0.01, 1, 0,
AIR700ICRU
0.0051, 0, ZTHICK, FLAG FOR LAYER 6 IN CENTRAL PART
0, 0, 0, 0,
KAPTON700ICRU
0.229, 0, ZTHICK, FLAG FOR LAYER 7 IN CENTRAL PART
0.7, 0.01, 1, 0,
AIR700ICRU
0.0127, 0, ZTHICK, FLAG FOR LAYER 8 IN CENTRAL PART
0.7, 0.01, 0, 0,
KAPTON700ICRU
0.229, 0, ZTHICK, FLAG FOR LAYER 9 IN CENTRAL PART
0.7, 0.01, 1, 0,
AIR700ICRU
0.0051, 0, ZTHICK, FLAG FOR LAYER 10 IN CENTRAL PART
0.7, 0.01, 0, 0,
KAPTON700ICRU
0.234, 0, ZTHICK, FLAG FOR LAYER 11 IN CENTRAL PART
0.7, 0.01, 1, 0,
AIR700ICRU
0.0051, 0, ZTHICK, FLAG FOR LAYER 12 IN CENTRAL PART
0.7, 0.01, 0, 0,
KAPTON700ICRU
0.229, 0, ZTHICK, FLAG FOR LAYER 13 IN CENTRAL PART
0.7, 0.01, 1, 0,
AIR700ICRU
0.0127, 0, ZTHICK, FLAG FOR LAYER 14 IN CENTRAL PART
0.7, 0.01, 0, 0,
```

```
KAPTON700ICRU
0.628, 0, ZTHICK, FLAG FOR LAYER 15 IN CENTRAL PART
0.7, 0.01, 0, 0,
AIR700ICRU
0.7, 0.01, 0, 9,   chamber wall
AIR700ICRU
0.7, 0.01, 0, 10,   gap
AIR700ICRU
0.7, 0.01, 0, 11,   container
AIR700ICRU
0, MRNGE
********** start of CM MIRROR with identifier mirror  **********
15.0, RMAX
MIRROR
18.873, 9.125, ZMIN, ZTHICK
4.67, -6.645, XFMIN, XBMIN
1, # LAYERS
0.00508,  thickness of layer 1
0.7, 0.01, 0, 12,
MYLAR700ICRU
0.7, 0.01, 0, 13,
AIR700ICRU
0.7, 0.01, 0, 14,
AIR700ICRU
**********************end of all CMs*****************************
 ##########################
 :Start MC Transport Parameter:

 Global ECUT= 0.7
 Global PCUT= 0.01
 Global SMAX= 1e10
 ESTEPE= 0.25
 XIMAX= 0.5
 Boundary crossing algorithm= EXACT
 Skin depth for BCA= 0
 Electron-step algorithm= PRESTA-II
 Spin effects= On
 Brems angular sampling= Simple
 Brems cross sections= BH
 Bound Compton scattering= Off
 Pair angular sampling= Simple
 Photoelectron angular sampling= Off
 Rayleigh scattering= Off
 Atomic relaxations= On
 Electron impact ionization= Off

 :Stop MC Transport Parameter:
 ##########################
```

A.2 BEAMnrc input file: VARIAN_6MV_PHSP_B_1x1

```
VARIAN_6MV_PHSP_B_1x1
#!GUI1.0
AIR700ICRU
0, 0, 0, 0, 0, 3, 0,  IWATCH ETC.
35000000000, 44, 59, 99, 0, 0, 0, 0,  NCASE ETC.
9, 21, 3, 0, 0, 0, 0, 0, 0, 0,  IQIN, ISOURCE + OPTIONS
/home/mcuser/EGS_storage/GCS_6_2_011/varian6x_A_GCS_6_2_011.egsphsp1
0, 0, 0.7, 0.01, 0, -2, 2.0,  0 , ECUT,PCUT,IREJCT,ESAVE
0, 0, 0, 0, 0,  PHOTON FORCING
1, 5,  SCORING INPUT
0,1
0,  DOSE COMPONENTS
14.2, Z TO FRONT FACE
*********** start of CM CHAMBER with identifier ion_cham
***********
10.0, RMAX
Ion Chamber
14.2, ZMIN
0, 15, 0, N_TOP, N_CHM, N_BOT
4.7625, 4.7752, 4.95, RADII FOR CENTRAL PART
0.629, 0, ZTHICK, FLAG FOR LAYER 1 IN CENTRAL PART
0.7, 0.01, 1, 0,
AIR700ICRU
0.0127, 0, ZTHICK, FLAG FOR LAYER 2 IN CENTRAL PART
0.7, 0.01, 0, 0,
KAPTON700ICRU
0.229, 0, ZTHICK, FLAG FOR LAYER 3 IN CENTRAL PART
0.7, 0.01, 1, 0,
AIR700ICRU
0.0051, 0, ZTHICK, FLAG FOR LAYER 4 IN CENTRAL PART
0.7, 0.01, 0, 0,
KAPTON700ICRU
0.234, 0, ZTHICK, FLAG FOR LAYER 5 IN CENTRAL PART
0.7, 0.01, 1, 0,
AIR700ICRU
0.0051, 0, ZTHICK, FLAG FOR LAYER 6 IN CENTRAL PART
0, 0, 0, 0,
KAPTON700ICRU
0.229, 0, ZTHICK, FLAG FOR LAYER 7 IN CENTRAL PART
0.7, 0.01, 1, 0,
AIR700ICRU
0.0127, 0, ZTHICK, FLAG FOR LAYER 8 IN CENTRAL PART
0.7, 0.01, 0, 0,
KAPTON700ICRU
0.299, 0, ZTHICK, FLAG FOR LAYER 9 IN CENTRAL PART
0.7, 0.01, 1, 0,
AIR700ICRU
0.0051, 0, ZTHICK, FLAG FOR LAYER 10 IN CENTRAL PART
0.7, 0.01, 0, 0,
KAPTON700ICRU
0.233, 0, ZTHICK, FLAG FOR LAYER 11 IN CENTRAL PART
0.7, 0.01, 1, 0,
AIR700ICRU
0.0051, 0, ZTHICK, FLAG FOR LAYER 12 IN CENTRAL PART
0.7, 0.01, 0, 0,
KAPTON700ICRU
0.23, 0, ZTHICK, FLAG FOR LAYER 13 IN CENTRAL PART
0.7, 0.01, 1, 0,
AIR700ICRU
```

```
0.0127, 0, ZTHICK, FLAG FOR LAYER 14 IN CENTRAL PART
0.7, 0.01, 0, 0,
KAPTON700ICRU
0.628, 0, ZTHICK, FLAG FOR LAYER 15 IN CENTRAL PART
0.7, 0.01, 1, 0,
AIR700ICRU
0.7, 0.01, 0, 9,   chamber wall
AIR700ICRU
0.7, 0.01, 0, 10,   gap
AIR700ICRU
0.7, 0.01, 0, 11,   container
AIR700ICRU
0, MRNGE
*********** start of CM MIRROR with identifier mirror  ***********
15.0, RMAX
MIRROR
18.873, 9.107, ZMIN, ZTHICK
4.67, -6.645, XFMIN, XBMIN
1, # LAYERS
0.00508,  thickness of layer 1
0.7, 0.01, 0, 12,
MYLAR700ICRU
0.7, 0.01, 0, 13,
AIR700ICRU
0.7, 0.01, 0, 14,
AIR700ICRU
*********** start of CM SLABS with identifier slab2  ***********
30, RMAX
:Start MC Transport Parameter:
1, NSLABS
27.98, ZMIN
0.01, 0.7, 0.01, 0, 0, 0
AIR700ICRU
*********** start of CM MCTWIST with identifier mctwist  ***********
30, RMAX
:Start MC Transport Parameter:
1, NMCTWIST
27.99, ZMIN
0.01, 0.7, 0.01, 0, 0, 0
AIR700ICRU
*********** start of CM JAWS with identifier jaws  ***********
5, RMAX
jaws
2, # PAIRED BARS OR JAWS
Y
28.0, 35.8, 0.14000, 0.17900, -0.14000, -0.17900,
X
36.7, 44.5, 0.18350, 0.22250, -0.18350, -0.22250,
0.7, 0.01, 0, 0,
0.7, 0.01, 0, 0,
W700ICRU
0.7, 0.01, 0, 0,
W700ICRU
**********************end of all CMs*****************************
 ##########################
 :Start MC Transport Parameter:

 Global ECUT= 0.7
 Global PCUT= 0.01
 Global SMAX= 5
 ESTEPE= 0.25
 XIMAX= 0.5
```

```
 Boundary crossing algorithm= PRESTA-I
 Skin depth for BCA= 0
 Electron-step algorithm= PRESTA-II
 Spin effects= On
 Brems angular sampling= Simple
 Brems cross sections= BH
 Bound Compton scattering= Off
 Pair angular sampling= Simple
 Photoelectron angular sampling= Off
 Rayleigh scattering= Off
 Atomic relaxations= On
 Electron impact ionization= Off

 :Stop MC Transport Parameter:
##########################
```

A.3 DOSXYZnrc input file: Water Tank Phantom

```
Water Tank Phantom
#!GUI1.0
2
H2O521ICRU
AIR521ICRU
0.7, 0.01, 0, 0, 0
-3, -3, -1, 1
-15.25
10, 1
0.25, 42
10, 1
-15.25
10, 1
0.25, 42
10, 1
0
0.25, 120
0, 0, 0, 0, 0, 0, 0, 0
0, 0, 0, 0, 0, 0, 0, 0
0, 0, 0, 0, 0, 0, 0, 0
2, 2, 0, 0, 0, 180, 0, 55.5, 0, 0, 0, 0, 0, 0
2, 0, 2, 0, 1, 0, 0, 55.5
/home/mcuser/EGS_storage/1x1_MCT/1x1_MCT_6_2_011.egsphsp1
25000000000, 0, 99, 11, 78, 100.0, 0, 4, 0, 1, 2.0, 0, 0, 0, 1, 1
 ##########################
 :Start MC Transport Parameter:

 Global ECUT= 0.7
 Global PCUT= 0.01
 Global SMAX= 1e10
 ESTEPE= 0.25
 XIMAX= 0.5
 Boundary crossing algorithm= EXACT
 Skin depth for BCA= 0
 Electron-step algorithm= PRESTA-II
 Spin effects= On
 Brems angular sampling= Simple
 Brems cross sections= BH
 Bound Compton scattering= Off
 Pair angular sampling= Simple
 Photoelectron angular sampling= Off
 Rayleigh scattering= Off
 Atomic relaxations= Off
 Electron impact ionization= Off

 :Stop MC Transport Parameter:
 ##########################
```

A.4 DOSRZnrc input file: Stereotactic Field Diode

```
TITLE= SFD_1x1_d_5

##########################
:start I/O control:

IWATCH= off
STORE INITIAL RANDOM NUMBERS= no
IRESTART= first
STORE DATA ARRAYS= yes
OUTPUT OPTIONS= material summary
ELECTRON TRANSPORT= normal
DOSE ZBOUND MIN= 4
DOSE ZBOUND MAX= 5
DOSE RBOUND MIN= 0
DOSE RBOUND MAX= 1

:stop I/O control:
##########################

##########################
:start Monte Carlo inputs:

NUMBER OF HISTORIES= 24000000000
INITIAL RANDOM NO. SEEDS= 38, 81
MAX CPU HOURS ALLOWED= 999
IFULL= entrance regions
STATISTICAL ACCURACY SOUGHT= 0.0000
SCORE KERMA= no

:stop Monte Carlo inputs:
##########################

##########################
:start geometrical inputs:

METHOD OF INPUT= individual
Z OF FRONT FACE= 0.0
DEPTH BOUNDARIES= 50.5, 55.425, 55.475, 55.525, 55.6, 56.04, 56.46,
56.93, 58.89, 70
RADII= 0.05, 0.0833, 0.14, 0.2, 20
MEDIA= AIR521ICRU,
 H2O521ICRU,
 ABS521,
 STEEL521ICRU,
 epoxy521,
 COAX521,
 SI521ICRU;

DESCRIPTION BY= planes
MEDNUM= 1, 2, 3, 4, 5, 6, 7, 6, 3
START ZSLAB= 1, 2, 3, 8, 5, 7, 4, 8, 4
STOP ZSLAB= 2, 10, 9, 9, 7, 9, 4, 9, 5
START RING= 1, 1, 1, 4, 1, 1, 1, 2, 2
STOP RING= 5, 5, 4, 4, 2, 1, 1, 2, 2

:stop geometrical inputs:
##########################

##########################
```

```
:start source inputs:

INCIDENT PARTICLE= all
SOURCE NUMBER= 21
SOURCE OPTIONS= 0, 0, 0, 0
FILSPC=
/home/mcuser/egsnrc_mp/BEAM_varian6x_B_MCT/1x1_MCT_6_2_011.egsphsp1

:stop source inputs:
#########################

#########################
:start MC transport parameter:

Global ECUT= 0.521
Global PCUT= 0.001
Global SMAX= 1e10
ESTEPE= 0.25
XImax= 0.5
Skin depth for BCA= 3
Boundary crossing algorithm= EXACT
Electron-step algorithm= PRESTA-II
Spin effects= on
Brems angular sampling= KM
Brems cross sections= BH
Electron Impact Ionization= On
Bound Compton scattering= On
Pair angular sampling= Simple
Photoelectron angular sampling= On
Rayleigh scattering= Off
Atomic relaxations= On
Set PCUT= 0
Set PCUT start region= 1
Set PCUT stop region= 1
Set ECUT= 0
Set ECUT start region= 1
Set ECUT stop region= 1
Set SMAX= 0
Set SMAX start region= 1
Set SMAX stop region= 1

:stop MC transport parameter:
#########################

#########################
:start variance reduction:

BREM SPLITTING= off
NUMBER OF BREMS PER EVENT= 1
CHARGED PARTICLE RUSSIAN ROULETTE= off
ELECTRON RANGE REJECTION= on
ESAVEIN= 2.0
RUSSIAN ROULETTE DEPTH= 0.0000
RUSSIAN ROULETTE FRACTION= 0.0000
EXPONENTIAL TRANSFORM C= 0.0000
PHOTON FORCING= off
START FORCING= 1
STOP FORCING AFTER= 1
CS ENHANCEMENT FACTOR= 1
CS ENHANCEMENT START REGION= 1, 1
CS ENHANCEMENT STOP REGION= 1, 1
```

```
:stop variance reduction:
#########################

#########################
:start plot control:

PLOTTING= off

:stop plot control:
#########################
```